



UPPSALA
UNIVERSITET

*Digital Comprehensive Summaries of Uppsala Dissertations
from the Faculty of Science and Technology 1469*

Multifunctional Carbon Foams by Emulsion Templating

*Synthesis, Microstructure, and 3D Li-ion
Microbatteries*

HABTOM DESTA ASFAW



ACTA
UNIVERSITATIS
UPSALIENSIS
UPPSALA
2017

ISSN 1651-6214
ISBN 978-91-554-9799-6
urn:nbn:se:uu:diva-312897

Dissertation presented at Uppsala University to be publicly examined in Polhemsalen, Ångström Laboratory, Lägerhyddsvägen 1, Uppsala, Friday, 3 March 2017 at 09:15 for the degree of Doctor of Philosophy. The examination will be conducted in English. Faculty examiner: Professor John R. Owen (University of Southampton).

Abstract

Asfaw, H. D. 2017. Multifunctional Carbon Foams by Emulsion Templating. Synthesis, Microstructure, and 3D Li-ion Microbatteries. *Digital Comprehensive Summaries of Uppsala Dissertations from the Faculty of Science and Technology* 1469. 139 pp. Uppsala: Acta Universitatis Upsaliensis. ISBN 978-91-554-9799-6.

Carbon foams are among the existing electrode designs proposed for use in 3D Li-ion microbatteries. For such electrodes to find applications in practical microbatteries, however, their void sizes, specific surface areas and pore volumes need be optimized. This thesis concerns the synthesis of highly porous carbon foams and their multifunctional applications in 3D microbatteries. The carbon foams are derived from polymers that are obtained by polymerizing high internal phase water-in-oil emulsions (HIPEs).

In general, the carbonization of the sulfonated polymers yielded hierarchically porous structures with void sizes ranging from 2 to 35 μm and a BET specific surface area as high as 630 $\text{m}^2 \text{g}^{-1}$. Thermogravimetric and spectroscopic evidence indicated that the sulfonic acid groups, introduced during sulfonation, transformed above 250 $^{\circ}\text{C}$ to thioether (-C-S-) crosslinks which were responsible for the thermal stability and charring tendency of the polymer precursors. Depending on the preparation of the HIPEs, the specific surface areas and void-size distributions were observed to vary considerably. In addition, the pyrolysis temperature could also affect the microstructures, the degree of graphitization, and the surface chemistry of the carbon foams.

Various potential applications were explored for the bespoke carbon foams. First, their use as freestanding active materials in 3D microbatteries was studied. The carbon foams obtained at 700 to 1500 $^{\circ}\text{C}$ suffered from significant irreversible capacity loss during the initial discharge. In an effort to alleviate this drawback, the pyrolysis temperature was raised to 2200 $^{\circ}\text{C}$. The resulting carbon foams were observed to deliver high, stable areal capacities over several cycles. Secondly, the possibility of using these structures as 3D current collectors for various active materials was investigated in-depth. As a proof-of-concept demonstration, positive active materials like polyaniline and LiFePO_4 were deposited on the 3D architectures by means of electrodeposition and sol-gel approach, respectively. In both cases, the composite electrodes exhibited reasonably high cyclability and rate performance at different current densities. The syntheses of niobium and molybdenum oxides and their potential application as electrodes in microbatteries were also studied. In such applications, the carbon foams served dual purposes as 3D scaffolds and as reducing reactants in the carbothermal reduction process. Finally, a facile method of coating carbon substrates with oxide nanosheets was developed. The approach involved the exfoliation of crystalline VO_2 to prepare dispersions of hydrated V_2O_5 , which were subsequently cast onto CNT paper to form oxide films of different thicknesses.

Keywords: Battery, Carbon, Electrochemical, Electrodeposition, Emulsion, Energy, Exfoliation, Foam, Lithium, Microbattery, Multifunctional, Nanoparticles, Polyaniline, Polymer, Power, Sol-gel, Storage, Structured, Three-dimensional

Habtom Desta Asfaw, Department of Chemistry - Ångström, Structural Chemistry, Box 538, Uppsala University, SE-751 21 Uppsala, Sweden.

© Habtom Desta Asfaw 2017

ISSN 1651-6214

ISBN 978-91-554-9799-6

urn:nbn:se:uu:diva-312897 (<http://urn.kb.se/resolve?urn=urn:nbn:se:uu:diva-312897>)

To my family, especially my mom

List of papers

This thesis is based on the following papers, which are referred to in the text by their Roman numerals.

- I **Boosting the thermal stability of emulsion-templated polymers via sulfonation: an efficient synthetic route to hierarchically porous carbon foams**
H. D. Asfaw, R. Younesi, M. Valvo, J. Maibach, J. Ångström, C.-W. Tai, Z. Bacsik, M. Sahlberg, L. Nyholm, and K. Edström, ChemistrySelect, 1 (4), 784–792 (2016)
- II **Emulsion-templated bicontinuous carbon network electrodes for use in 3D microstructured batteries**
H. D. Asfaw, M. Roberts, R. Younesi, and K. Edström, J. Mater. Chem. A, 1 (44), 13750-13758 (2013)
- III **Emulsion-templated graphitic carbon foams with optimum porosity for 3D Li-ion microbatteries**
H. D. Asfaw, C.-W. Tai, L. Nyholm, and K. Edström, in manuscript
- IV **Nanosized LiFePO₄-decorated emulsion-templated carbon foam for 3D micro batteries: a study of structure and electrochemical performance**
H. D. Asfaw, M. Roberts, C.-W. Tai, R. Younesi, M. Valvo, L. Nyholm, and K. Edström, Nanoscale, 6(15) 8804-8813 (2014)
- V **Surface-oxidized NbO₂ nanoparticles for high performance lithium microbatteries**
H. D. Asfaw, C.-W. Tai, L. Nyholm, and K. Edström, in manuscript
- VI **A one-step water based strategy for synthesizing hydrated vanadium pentoxide nanosheets from VO₂ (B) as freestanding electrodes for lithium battery applications**
A. Etman, H. D. Asfaw, N. Yuan, J. Li, Z. Zhou, F. Peng, I. Persson, X. Zou, T. Gustafsson, K. Edström, J. Sun, J. Mater. Chem. A, 4(46), 17988-18001 (2016)

Reprints were made with permission from the publishers.

My contributions to the papers

- I. I planned the project, carried out the synthesis of the carbon foams, conducted part of the characterizations including SEM, surface area and porosity analysis, TGA and XRD. I also participated in the analyses of the samples using Raman, IR and RGA. I processed most of the data and wrote the manuscript as a main author with contributions from the co-authors.
- II. I participated in the planning of the experiments, the fabrication of the electrodes, and the writing of the manuscript.
- III. I did all the synthesis and characterization of the materials, except the TEM analysis. I wrote the manuscript as the main author with contributions from the co-authors.
- IV. I planned and carried out the experiments. I performed all the characterizations of the materials, with the exception of the TEM analysis. I wrote the manuscript as the main author with contributions from the co-authors.
- V. I planned and carried out the synthesis, and characterization of the materials, with the exception of the TEM analysis. I wrote the manuscript as the main author with contributions from the co-authors.
- VI. I took part in the planning of the project, the execution of the experiments, and discussion of the results. I carried out the electrochemical testing of the electrodes. I also wrote the electrochemical section of the manuscript. Contributed equally as a first author.

The author also contributed to the following papers that are not included in this thesis.

- **A Li-Ion Microbattery with 3D Electrodes of Different Geometries**
G. Oltean, H. D. Asfaw, L. Nyholm, and K. Edström, ECS Electrochemistry Letters, 3(6), A54-A57 (2014)
- **A General Method to Fabricate Free-Standing Electrodes: Sulfonate Directed Synthesis and their Li⁺ Storage Properties**
Y. Ma, H. D. Asfaw, and K. Edström, Chem. Mater., 27(11), 3957-3965 (2015)
- **Three-dimensional carbon foam supported tin oxide nanocrystallites with tunable size range: Sulfonate anchoring synthesis and high rate lithium storage properties**
Y. Ma, H. D. Asfaw, and K. Edström, J. Power Sources, 294, 208-215 (2015)
- **Encasing Si particles within a versatile TiO_{2-x}F_x layer as an extremely reversible anode for high energy-density lithium-ion battery**
Y. Ma, H. D. Asfaw, C. Liu, B. Wei, and K. Edström, Nano Energy, 30, 745-755 (2016)
- **Solid-State 3D-Microbatteries using Functionalized Polycarbonate-based Polymer Electrolytes**
B. Sun, H. D. Asfaw, D. Rehnlund, J. Mindemark, L. Nyholm, K. Edström and D. Brandell, in manuscript
- **The SEI layer on hard carbon anodes in sodium-ion batteries**
H. D. Asfaw, M. Valvo, K. Edström, and R. Younesi, in manuscript

Contents

My contributions to the papers	vii
Abbreviations	xii
Symbols	xiii
Preface	xv
1 Electrochemical Energy Storage	19
1.1 The development of lithium-ion batteries	19
1.2 Electrode processes	21
1.3 Porous electrodes	24
2 Three-dimensional (3D) Microbatteries	27
2.1 Electrode architectures and cell Design	27
2.1.1 Three-dimensional (3D) electrode architectures	27
2.1.2 High-aspect-ratio array electrodes	29
2.1.3 High-aspect ratio micro-channel electrodes	31
2.1.4 Foam electrodes	32
2.2 Materials selection and deposition	33
3 Synthesis of Carbon Foams from Emulsions	36
3.1 Overview of emulsion-templated carbon foams	36
3.1.1 Polymerization and pyrolysis of high internal phase emulsions	37
3.1.2 Carbon foams from water-in-oil polyHIPEs	37
3.1.3 Carbon foams from oil-in-water polyHIPEs	38
3.1.4 Carbon foams from Pickering polyHIPEs	39
3.2 Synthesis procedure	39
3.3 The microstructure of emulsion-templated polymer and carbon foams	41
3.4 Optimizing surface area and porosity	45
3.5 Chemical transformations during pyrolysis	48
3.6 Structural evolution during pyrolysis	55
3.7 The surface of carbon foams	58
4 Lithium-ion Storage in Emulsion-templated Carbon Foams	60
4.1 Lithium-ion storage and the structure of carbon materials	60
4.2 Emulsion-templated carbon foam anodes	61
4.2.1 The first discharge and pyrolysis temperature	61

4.2.2	Electrochemical performance	63
5	Emulsion-templated Carbon Foams as 3D Substrates	66
5.1	PANI-coated carbon foams for 3D lithium microbatteries	66
5.1.1	Electrodeposition of PANI	66
5.1.2	PANI in lithium batteries	68
5.1.3	Electrochemical study on PANI-coated carbon foams ..	69
5.2	LiFePO ₄ -coated carbon foam as a positive electrode	71
5.2.1	Sol-gel synthesis of LiFePO ₄	72
5.2.2	Characterization	72
5.2.3	Electrochemical investigation	74
6	Synthesis of Mixed-Valence Niobium and Molybdenum Oxides Through Carbothermal Reduction in Emulsion-templated Carbon Foams	78
6.1	Sol-gel synthesis of niobium and molybdenum oxides on carbon foams	78
6.2	Structural investigation: over-stoichiometric NbO ₂	79
6.3	Structural investigation: mixed oxides Mo ₃ Nb ₂ O ₁₁	81
6.4	Electrochemical behaviors and rate performance: NbO _{2+δ}	84
6.5	Lithiation-induced enhancement of charge transfer kinetics	86
6.6	Electrochemical behaviors and rate performance: Mo ₃ Nb ₂ O ₁₁ ..	87
7	Exfoliation-Deposition of Metal Oxides: A Facile Approach to Material Deposition on Carbon Substrates	90
7.1	Exfoliation of VO ₂ (B) in water	90
7.2	Hydrated V ₂ O _{5-δ} nanosheets from exfoliated VO ₂	90
7.3	Deposition of hydrated V ₂ O _{5-δ} nanosheets on carbon nanotube paper	91
7.4	V ₂ O ₅ -coated CNT paper as a freestanding cathode for lithium batteries	91
8	Conclusions and Outlook	96
9	Sammanfattning på Svenska	101
10	Appendix: Characterization techniques	105
10.1	Thermal analysis	105
10.2	Residual gas analysis: pyrolysis-mass spectrometry	106
10.3	Electron microscopy	106
10.3.1	Scanning Electron Microscopy (SEM)	106
10.3.2	Transmission Electron Microscopy (TEM)	108
10.4	Specific surface area and porosity analysis	108
10.5	X-ray diffraction	110
10.6	X-ray spectroscopy	110
10.6.1	X-ray photoelectron emission spectroscopy	110

10.6.2	X-ray absorption near edge structure spectroscopy	111
10.7	Vibrational spectroscopy	112
10.7.1	Fourier transform infrared spectroscopy	112
10.7.2	Raman spectroscopy	113
10.8	Electrochemical Methods	113
10.8.1	Cyclic voltammetry	113
10.8.2	Controlled-current methods	115
10.8.3	Electrochemical impedance spectroscopy	116
10.8.4	Electrode preparation and cell construction	117
	References	120

Abbreviations

2D	Two-Dimensional
3D	Three-Dimensional
3DOM	Three-Dimensional Ordered Macroporous
ATR	Attenuated Total Reflectance
BET	Brunauer-Emmett-Teller
BJH	Barrett-Joyner-Halenda
BSE	Back-Scattered Electrons
CV	Cyclic Voltammetry
DEC	Diethyl Carbonate
DVB	Divinylbenzene
EC	Ethylene Carbonate
FTIR	Fourier Transform Infrared
HIPE	High Internal Phase Emulsion
PANI	Polyaniline
polyHIPE	High Internal Phase Emulsion Polymer
PPI	Pores Per Inch
PSD	Pore Size Distribution
PTFE	Poly(tetrafluoroethylene)
Pyr-MS	Pyrolysis-Mass Spectrometry
RGA	Residual Gas Analysis
RVC	Reticulated Vitreous Carbon
SE	Secondary Electrons
SEM	Scanning Electron Microscopy
STEM	Scanning Transmission Electron Microscopy
TEM	Transmission Electron Microscopy
TGA	Thermogravimetric Analysis
VBC	4-Vinylbenzyl Chloride
XAFS	X-ray Absorption Fine Structure
XANES	X-ray Absorption Near-Edge Structure
XPS	X-ray Photoelectron Spectroscopy

Symbols

α	Charge transfer coefficient
α_c	Extent of conversion
A	Surface area
C	Concentration
C_a	Capillary number
C^b	Bulk concentration
C_{BET}	Multilayer adsorption constant
C_{eff}	Coulombic efficiency
d	Inter-planar distance
D	Diffusion coefficient
E_a	Activation energy
E	Energy density
E_b	Binding energy
E_k	Kinetic energy
ε	Porosity
F	Faraday constant
η	Overpotential
η_a	Activation overpotential
η_c	Concentration overpotential
η_{con}	Viscosity of the continuous phase
φ_a	Apparent pore volume
φ_p	Pore volume
γ	Shear rate
h	Planck constant
i	Current
i_c	Capacitive current
i_f	Faradaic current
i_o	Exchange current
i_p	Peak current
λ	Wavelength
κ	Ionic conductivity
κ_{eff}	Effective ionic conductivity
k_o	Intrinsic rate constant
L	Particle size
m	Mass of active material
m_s	Mass of adsorbent
ν	Scan rate or frequency

n	Number of moles of electrons
n_a	Amount of adsorbed gas
n_m	Monolayer adsorbate coverage
N_A	Avogadro constant
p	Pressure
p^o	Saturation pressure
P	Power
R	Gas constant
R_{el}	Electrolyte resistance
R_{crit}	Critical droplet size
ρ_b	Bulk density
ρ_p	Particle density
σ	Cross-sectional area
τ_D	Time constant for solid-state diffusion
τ	Tortuosity
T	Temperature
T_a	Temperature amplitude
T_m	Maximum temperature
t	Time
t_e	Electrode thickness
V	Voltage
Z	Pre-exponential factor
ω	Angular velocity or frequency

Preface

Energy storage is one among many concerns humanity has to continually deal with. To ensure sustainable provision of energy is of utmost importance as long as technological breakthroughs are concerned. Particularly, the era we live in is characterized by increased miniaturization of electronic devices, and their integration into every aspect of our lives. This has in turn necessitated the development of batteries with the desired form factors and efficiency. Assuredly, what makes a battery efficient is not only the active material used but also the choice of the electrode design and configuration. A notable example where optimum electrode design is indispensable is a microbattery. Advances in the design and application of miniature medical implants, distributed systems with interacting sensor nodes, actuators, tele-transmitters, receivers and other microsystems have led to increased demands for microbatteries. To meet the requirements for high energy and power densities imposed by such sophisticated electronic systems, a paradigm shift from planar to 3D electrode configurations is needed. Research in microbatteries, therefore, boils down to the fabrication of 3D electrodes, the synthesis of active materials, and the development of material deposition techniques suited for coating the bespoke 3D electrodes. As widely reported, various electrode designs have been proposed for use in 3D microbatteries. Different material deposition approaches have been explored. A variety of active materials have also been investigated. Despite all efforts and gains made so far, there remains much left to study in order to come up with ideal battery systems that are capable of replacing the current state-of-the-art microbatteries.

This thesis deals with the potential application of emulsion-templated carbon foams as anodes and 3D substrates in microbatteries. It is written based on a set of refereed papers published over the past four years. A detailed study on the synthesis of the carbon foams and their multifunctional use as active materials, and as 3D scaffolds is presented. To gain insight into the factors which can be manipulated in order to tailor the porosity, specific surface areas, and void-size distributions of the carbon foams, an in-depth investigation has been made into the various stages involved in the preparation, and the carbonization of high internal phase emulsion polymers (polyHIPEs). The benefits of using these carbon foams as alternatives to commercial carbon foams are also highlighted. Additionally, efforts have been made to identify active materials that are suitable for high power applications in microbatteries. In summary, the projects included in this thesis were intent on achieving the following objectives:

- to investigate emulsion-templated carbon foams as better alternatives to commercial carbon foams, which normally possess significantly lower specific surface areas and void sizes that are orders of magnitudes larger
- to identify synthesis strategies to further optimize the porosity and void dimensions of emulsion-templated carbon foams, which can be suitable for constructing microbatteries with high power and energy densities
- to unravel the chemical processes involved in the conversion of emulsion-templated polymers to carbon foams
- to optimize the performance of monolithic carbon foams as multifunctional electrodes in 3D microbatteries
- to improve the structure of carbon foam anodes by increasing the temperature of pyrolysis
- to identify and synthesize composite 3D electrodes based on emulsion-templated carbon foams coated in active materials, via electrodeposition and sol-gel processing
- to develop new methodologies for coating 3D electrodes based on carbon

Practically all of the research work reported in this thesis has been undertaken within the Ångström Advanced Battery Center (ÅBC) of Uppsala University under the supervision of Profs Kristina Edström and Leif Nyholm. During my time in this group I have received a lot of help and generosity from many people. First and foremost, I owe deep gratitude to Kristina, Matt Roberts, Tatti and Daniel for taking care of the administrative issues and accommodation when I came to Uppsala for my Master thesis project, and for making my stay as comfortable as it could be. On the research part, this thesis could have not been materialized in its current bound form had it not been for the continuous technical and academic support I got from within and outside the group. I would like to extend my thanks to my main supervisor Kristina Edström for her continual support and encouragement during the whole period of my PhD studies. Kristina, I appreciate the wonderful opportunity you have given me to do my PhD in your research group and your hard work to secure the funds that covered my salary, and... also allowed me to experiment as many crazy ideas as I could! Thanks a lot for being always positive towards my ideas. As much gratitude goes to my co-supervisor Leif Nyholm for the help with electrochemistry, the continuous encouragement and other valuable contributions. I should be grateful to your unfailingly fast feedbacks (some sent on weekends!) on my manuscripts and the great scientific discussions filled with a lot of passion. I have learnt a great deal along the way. Special thanks go to Matthew Roberts for introducing me to microbattery research, and for being a kind and patient supervisor during my master thesis work as well. Thanks a lot for your help with reading and correcting my manuscripts.

I would also like to acknowledge the following co-authors for the scientific and technical contributions they have provided: *Ahmed Etman, Daniel Brandell, Reza Younesi, Mario Valvo, Ma Yue, Gabriel Oltean, Julia Maibach, Bing Sun, David Rehnlund, Jonas Ångström, Jonas Mindemark, Junliang Sun*

(Stockholm U), Cheuk-Wai Tai (Stockholm U) and Zoltan Bacsik (Stockholm U). My acknowledgement wouldn't be complete if I forgot to recognize the technical assistance and advice I received from Henrik Eriksson, Jan Bohlin, Anders Lund, Pedro Berastegui, Adam Sobkowiak, Girma Hailu, Viktor Renman, Chenjuan Liu, Steven Renault, Ronnie Mogensen, Martin Sahlberg, Johan Cedervall, Mikael Ootsson, Håkan Rundlöf and Torbjörn Gustafsson. I appreciate my good Palermo/Norrlands/Bowling... friends for the great fun and games we have had over the years: Adam S., Bertrand P., Getachew K., Konstantinos D., Marco C., Mario V., Matt R., Matthew W., Reza Y., Ronnie M., and Stéven R. I am glad to mention Kersti for the nice Christmas dinner and pleasant discussion, Petter for the interesting/fun chit-chats in the lab and for being a nice companion when traveling to SU for the TEM course, and Dou for being such an amiable officemate. I owe a deep gratitude to a long list of current and former colleagues in ÅABC for the friendly working environment: Alina, Andoria, Andreas, Anti, Burak, Cesar, Chao, Charlotte, Christofer, Eric, Erik B., Fabian, Feres, Fernanda, Fredrik B., Fredrik L., Jeff, Jia, Jonas Hedman, Jonas H., Josh, Julia M., Karima, Kasia, Mahsa, Matt L., Mohammed, Nina, René, Rickard, Ruijun, Sara, Shruti, Siham, Solveig, Taha, Therese, Tim, Viktor N., Wei, Will, Yanyan, and Zhaohui. Last but not least, I would like to acknowledge the kind and friendly administrative assistance I have received from the current and former administrators at Chemistry-Ångström: Anna Cuturic, Diana Bernelind, Eva Larsson, Patrik Lindahl, Peter Lundström, Slavica Nuic, Susanne Söderberg, Terese Magnusson and others whom I might have forgotten.

Habtom Desta Asfaw

Uppsala, 2017

1. Electrochemical Energy Storage

Electrochemical reactions form the basis of energy storage in batteries, supercapacitors, fuel cells, and so on. Batteries, particularly, play a pivotal role in powering consumer electronics from laptops to micro-sized sensors. For instance, current advances in the design and application of miniature medical implants, sensor nodes, wireless telecommunications, and other microsystems have increased the demand for microscale batteries [1–4]. A clear demonstration of this can be seen in the report compiled by KnowMade[®] and published in 2016 [5]. The report analyzed the trend in IP patents filed or published over the last 50 years. Accordingly, a dramatic increase in innovations related to microbatteries has been witnessed as of the year 2000, and over 3000 patents were published up to 2016. The necessity for developing or improving electrode architectures and suitable materials for microbatteries cannot, therefore, be overemphasized. Alternative energy sources like temperature gradient, sunlight, vibration, and so on [6–8] are being studied as potential candidates for meeting the energy demands. However, these sources are intermittent and cannot supply the required amount of energy whenever needed. Thus, only microbatteries, particularly lithium-ion batteries, can enable the coming age of internet of things (IoT) and miniature electronics [9].

In general, batteries can be classified into two broad categories, namely non-rechargeable or primary and rechargeable or secondary [10]. Primary batteries entail reactions which consume stored chemicals to generate electricity, and are discarded when fully discharged. Principal examples are the Zn-MnO₂/carbon, alkaline Zn-MnO₂, Zn-Ag₂O, Zn-NiOOH, and so on [10]. A rechargeable battery, on the other hand, is based on chemical reactions which can be reversed after having been spent, simply by running current across the terminals of the battery. Various rechargeable battery chemistries have been developed so far including lead acid battery, nickel-cadmium (Ni-Cd), nickel metal hydride (Ni-MH), and most importantly lithium-ion batteries. Lithium-ion batteries can provide higher energy densities, and have become popular in consumer electronics, and large scale applications [11].

1.1 The development of lithium-ion batteries

The emergence of lithium-ion batteries may be associated with the seminal researches into lithium intercalation compounds conducted in the 1970s. Compounds prepared by chemical or electrochemical intercalation of lithium into

layered hosts such as graphite and transition metal dichalcogenides were investigated in relation to their thermodynamic behaviors, structures, superconducting properties, lithium ion conductivity and so on [12–14]. In 1976, Whittingham demonstrated that lithium ions could reversibly be intercalated into and removed from TiS_2 host structure, and thus proposed a novel mechanistic basis for a new generation of rechargeable batteries [15]. Basically, intercalation refers to the inclusion of small ions or molecules into hosts with layered framework structures. Typical examples of intercalation hosts include graphite, transition metal dichalcogenides such as TiS_2 , MoS_2 , NbS_2 , TiSe_2 , and transition metal oxides like MoO_3 , and V_2O_5 [14–17].

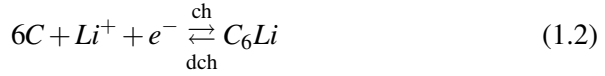
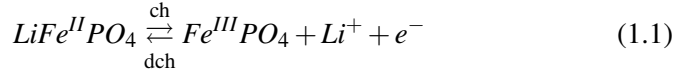
A remarkable innovation, which unarguably revolutionized the use of batteries in portable electronics, is credited to John Goodenough’s group at Oxford which reported in 1980 that LiCoO_2 can be effectively utilized as a cathode to fabricate a battery of higher working voltage, rate and energy density. [18] That discovery led to the widespread use of a 3.7 volt battery in portable electronics. Another group of cathode materials which are considered safe and viable contenders are lithium containing polyanionic compounds. [19] Unlike, layered chalcogenides, these compounds allow the movement of lithium ions via their channeled structures. Some examples are LiFePO_4 [20, 21], $\text{Li}_2\text{FeSiO}_4$ [22], and LiFeSO_4F [23, 24].

Early research on lithium batteries used lithium metal as an anode. Since lithium metal was highly reactive and its use in batteries posed significant safety risk, the need to replace it was imperative [25]. Lithiated graphite, which is an intercalation compound itself, was then proposed to replace pure metallic lithium. Though its electrochemical investigation can be traced back to earlier works by J.O. Besenhard on electrochemical reduction of graphite in organic solutions of lithium salts [26], the use of lithiated graphite as a reversible anode was introduced by R. Yazami in 1983 [27]. Since then, a large proportion of lithium-ion batteries in commercial use are based on LiCoO_2 cathode and graphite anode. The electrochemical intercalation of lithium ions into graphite occurs below 0.2 V versus lithium [28, 29]. However, most electrolytes commonly used in lithium-ion batteries are unstable at lower voltages (< 1 V vs. Li^+/Li) and decompose to produce a mixture of compounds that passivate the anode surface against further reaction. This inadvertently formed layer, namely the solid electrolyte interphase (SEI) [30, 31], is absent in another class of insertion-based anodes such as $\text{Li}_4\text{Ti}_5\text{O}_{12}$, TiO_2 , TiNb_2O_7 and Nb_2O_5 since they operate above 1.5 V versus lithium [32–36]. Apart from graphite, other allotropes of carbon such as disordered carbons, carbon nanotubes and graphene have been studied in a quest for anodes that can store more lithium ions (charge) beyond the theoretical limit of 372 mAh g^{-1} [37–39] for graphite. In this regard, porous disordered carbons have particularly aroused research interest since they provide high surface areas available for lithium ion storage. Inherent to these materials, unfortunately, is the huge irreversible charge consumed during the first discharge; only a fraction of the

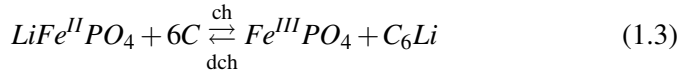
lithium ions is retrieved in the subsequent cycles of the battery. Another class of candidates for anode materials includes alloys and convertible oxides which operate by different mechanisms but are plagued by the same problem of irreversibility [40–43].

1.2 Electrode processes

A battery is built from a group of electrochemical cells which harness stored chemical energy to generate electricity. Every electrochemical cell consists essentially of an anode, a cathode and an electrolyte. The electrolyte allows ions to shuttle between the two electrodes in response to the electrical current flowing in the external circuit. To understand how an electrochemical cell works, it is crucial to look into the thermodynamics and kinetics of the reactions occurring at the electrodes [25, 44, 45]. By way of illustration, consider a full-cell electrochemical cell consisting of LiFePO_4 cathode and a graphite anode. *Figure 1.1* shows a generalized schematic of a lithium-ion battery. The following reactions take place at the respective electrodes.



And, the overall cell reaction can be put as



The thermodynamic output voltage of the cell, when no current is applied or drawn, may be represented as

$$V_{\text{OC}} = V_{\text{cell}} = V_{\text{C}} - V_{\text{A}} \quad (1.4)$$

where V_{OC} , V_{cell} , V_{C} , and V_{A} stand for the open circuit voltage, the cell voltage, cathode voltage, and anode voltage, respectively, associated with the electrochemical cell. During battery operation under the influence of applied current or voltage, the cell voltage departs from the equilibrium/thermodynamic value due to voltage drops related to ohmic drop (IR_{Ω}), activation (electron transfer) overpotential (η_{a}) and concentration overpotential (η_{c}) [25, 45].

$$V'_{\text{cell}} = V_{\text{OC}} \pm IR_{\Omega} \pm \eta_{\text{a}} \pm \eta_{\text{c}} \quad (1.5)$$

where - is for discharge and + is for charge. These parameters can pictorially be depicted in the form of a polarization curve as shown in *Figure 1.2*. The

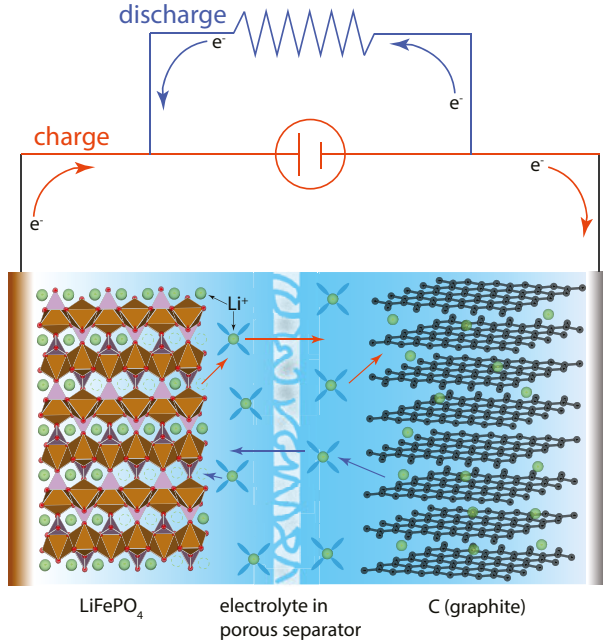


Figure 1.1. Schematic illustration of a full-cell Li-ion battery consisting of LiFePO₄ and graphite in liquid electrolyte

ohmic drop is caused by the resistance of the electrolyte to the flow of ions and the resistance to electronic current flow through the electrode assembly including the active materials and the current collectors.

The activation or surface overpotential can be thought of as the driving force needed to cause current to flow (or electrons to tunnel) across the electrode-active material interface. In essence, it is the difference between the equilibrium potential and the potential observed when the electrode is under applied current. A phenomenological relation, the *Butler-Volmer* equation, [46] defines the fundamental dependence of current on the important parameters related to the electrode system. Mathematically,

$$i = nFAk_o \left[C_R(0,t) \exp(1 - \alpha) \frac{F\eta}{RT} - C_O(0,t) \exp(-\alpha) \frac{F\eta}{RT} \right] \quad (1.6)$$

In the relation given above, i , n , F , A , k_o , α , η , $C_O(0, t)$, and $C_R(0, t)$ represent, respectively, the current response, the number of moles of electron involved in the electron transfer process, Faraday constant (96485.3329 C mol⁻¹ or 26.801 Ah mol⁻¹), the surface area of the electrode, the intrinsic heterogeneous rate

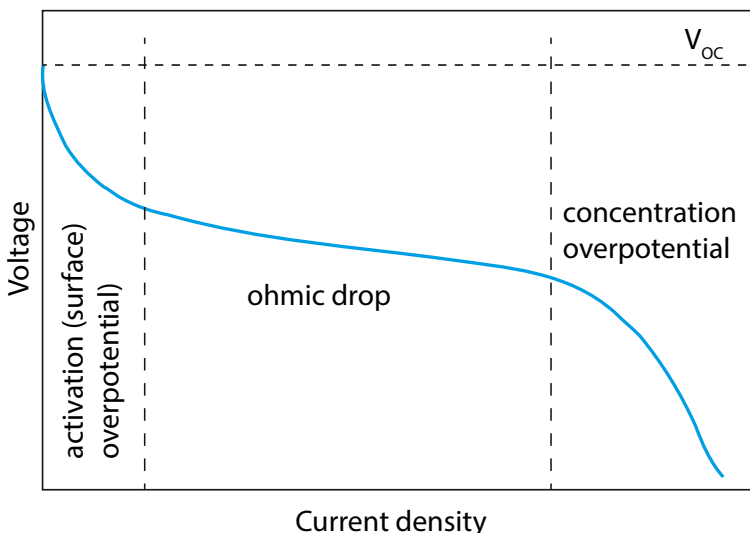


Figure 1.2. A typical polarization curve showing the origins of voltage drop in an electrochemical cell under operation

constant of the electrode reaction, the transfer coefficient of the electrode process, the interfacial activation overpotential, the surface concentration of the oxidized species, and the surface concentration of the reduced species. The concentration overpotential arises at relatively higher current densities when the transport of the lithium ions to or away from the electrodes is not sufficiently fast so as to sustain the electrode reaction. For instance, this occurs when the diffusion of the lithium ions in the solid active materials is too sluggish. Hence, a sharp decline or rise in the voltage is usually observed at the end of charge and discharge curves. Careful electrode and cell design is necessary to tackle voltage drops involved during cell operation. A good deal of efforts is focused on the optimization of electrode formulations towards improving the electrochemical performance of batteries. The following are some of the common strategies employed to achieve optimum cell operation:

- using nano-sized active materials
- using active materials with good ionic and electronic conductivities
- optimizing the proportion of binders, conductive additives, and active materials in the composite electrodes
- using electrically-conducting binders in the electrode formulation
- optimizing porosity or density of the composite electrodes

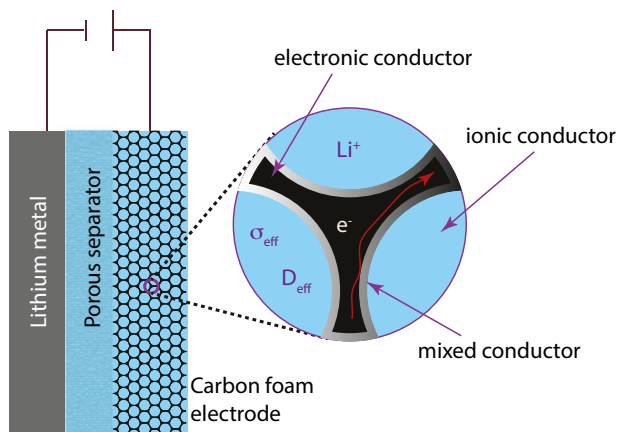


Figure 1.3. Schematic description of an electrochemical cell composed of a porous working electrode in which the electrolyte occupies the vacant voids. The symbols D_{eff} and κ_{eff} , denote, respectively, the effective diffusion coefficient and the effective ionic conductivity.

1.3 Porous electrodes

Most electrodes employed in lithium-ion batteries are heterogeneous materials composed of redox-active materials, carbon and polymeric binders fixed on metal current collectors. The effective electrical and ionic conductivities through the electrode structures rely on the formulation of the composite electrodes [44, 47]. Inclusion of critical amounts of porosity and conductive additives in the electrodes is essential to ensure proper utilization of the active materials over sustained cycling. In this regard, bicontinuous electrode structures are preferable for applications wherein both reasonably high power and high energy densities are required. Monolithic porous electrodes can be visualized as forming continua of electrolyte, active material and conductive matrix [48]. In such electrode designs, the ionic transport of the lithium ions, the kinetics of the electrochemical reactions, the interparticle electrical contact, and the electrical wiring of the active materials to current collector can be enhanced and thus high power density can be achieved. As noted in the previous section, the rate of such electrochemical processes is governed by the intrinsic rate constant, the interfacial surface area and the activation overpotential of the electrodes. Porous electrodes present plenty of room for reactants to stay in close proximity to the interfacial surface area. Large area-to-volume ratios can be achieved with a coating of active materials onto the surface of the porous electrodes (*Figure 1.3*). Thus, they offer a high interfacial surface area allowing for increased amount of reaction to take place within a small spatial volume [48]. Monolithic, porous carbon electrodes are attractive for applications in energy storage and conversion devices, electrosynthesis and

electroanalytical analysis. They are easy to handle and possess considerably higher electrical conductivities, in contrast to heterogeneous cast electrodes. There are some essential descriptors that are often invoked to characterize the performance of porous electrodes in electrochemical reactors. These include porosity, tortuosity, and percolation.

Porosity

Porosity can be thought of as the amount of vacant space contained in a solid material. It can be defined as the fraction of the apparent volume (V) of a solid substance that is taken up by voids (V_p), or occupied by a liquid or a gaseous phase. A measure of porosity can range from 0 to 1 or 100%. Mathematically, the value of porosity (ε) can be expressed as

$$\varepsilon = \frac{V_p}{V} \quad (1.7)$$

Alternatively, it can also be calculated in terms of the bulk (ρ_b) and particle (ρ_p) densities of the porous media.

$$\varepsilon = 1 - \frac{\rho_b}{\rho_p} \quad (1.8)$$

Geometric parameters like pore widths, shapes, and connectivity are important in describing the electrochemical performance of porous electrodes.

Tortuosity

Tortuosity is considered as a key parameter for describing the transport properties of electrolytes in porous electrodes. When used in electrochemical cells, the electrolyte fills the voids in the porous electrode. In bicontinuous carbon foams, the solid matrix and the pore electrolyte form infinitely interconnected structures. Since the electrolyte is confined in the pores of the electrode, its effective transport properties in terms of diffusion and transport number of the ions differ from the values it would have outside the pores, *i.e.*, in the bulk of the solution. Thus the value of porosity ought to be taken into account in the equations describing the transport of the ions in the pore electrolyte. In this case, the porosity is the volume of the electrolyte expressed as a fraction of the total or apparent volume of the electrode. The effective transport properties, [49] can be written as follows

$$D_{eff} = \frac{\varepsilon}{\tau} D_o \quad (1.9)$$

and

$$\kappa_{eff} = \frac{\varepsilon}{\tau} \kappa_o \quad (1.10)$$

Alternatively, making use of Bruggeman relation,

$$\frac{\varepsilon}{\tau} \approx \varepsilon^{1.5} \quad (1.11)$$

the equations shown above can be reformulated as

$$D_{eff} \approx \varepsilon^{1.5} D_o \quad (1.12)$$

and

$$\kappa_{eff} \approx \varepsilon^{1.5} \kappa_o \quad (1.13)$$

In these relations, the variable τ denotes tortuosity, whose value is always larger than 1. Tortuosity may, as such, be treated as a microstructural property of the electrode and is thus affected by the morphology and spatial orientations of the constituents of the solid matrix of the porous electrodes. It determines the efficacy of the porous pathways in allowing the electrolyte permeate the entirety of the electrode. These parameters are essential for all types of electrodes and inevitably affect the kinetics of reactions occurring at the electrodes. To be able to evaluate the optimal magnitudes of these parameters is indispensable if one is to fabricate electrodes that are suited for power applications in lithium-ion batteries or supercapacitors. Thus, design considerations of electrodes have received considerable attention. [50]. Since bicontinuous carbon foams possess low tortuosity, high porosity and excellent electrical conductivity, they can be used to fabricate thick electrodes which can deliver high energy density without considerably sacrificing the power density. Mathematically, for a porous electrode with a thickness t_e , the electrolyte resistance (R_{el}) [51] can be expressed as

$$R_{el} = \frac{\tau}{\varepsilon} \frac{t_e}{\kappa_o} = \frac{t_e}{\kappa_o \varepsilon^{1.5}} = \frac{t_e}{\kappa_{eff}} \quad (1.14)$$

Thus, 3D porous electrodes like carbon foams can be used in microbatteries wherein increased amount of active materials (a thick layer of active materials) is required. However, most carbon foams on the market are unsuitable as they possess large void dimensions ($> 100 \mu\text{m}$), and using them in micro-battery electrodes results in low energy densities. For such electrodes to find widespread use as 3D electrodes, their void sizes and pore volumes need be optimized.

2. Three-dimensional (3D) Microbatteries

Microbatteries are small-sized electrochemical devices specifically designed for use in autonomously-powered systems. Analogous to commercial lithium-ion batteries, microbatteries come in different sizes, configurations, nominal voltage and capacities. Included in this chapter are outlines of the most essential aspects of microbattery electrodes like electrode fabrication and material deposition. Short reviews of the various electrode architectures and material deposition approaches are presented.

2.1 Electrode architectures and cell Design

The trend in microelectronics is to fabricate self-sufficient devices in which a processor, communicators, sensors and power sources are integrated in a spatial volume of less than 10 mm^3 [1, 2, 52]. In such applications wherein space is at a premium, power devices that are sufficiently small, yet able to provide ample energy at desirable rates, should be utilized. Presently, either thin or thick film microbatteries are commonly used to power microscale devices. Thin-film (2D) microbatteries make use of only the in-plane surface and are suitable for applications which require high power at low capacity. They are composed of stacks of active materials, and an electrolyte deposited on a planar substrate, as shown in *Figure 2.1 a*) [53, 54]. Despite their high rate capability, thin film microbatteries suffer from limited energy density. Increasing the thickness of the layers of active materials leads to increased capacity but with a concomitant increase in ion-diffusion path length and ohmic drop, which result in a marked reduction in power density [1]. To achieve acceptable tradeoff between energy and power densities, careful design of electrode architectures and the development of suitable material are issues of paramount importance. Three-dimensional electrode architectures are being developed to achieve these goals. A schematic of a 3D Zn-air microbattery is given in *Figure 2.1 b*) as an example.

2.1.1 Three-dimensional (3D) electrode architectures

In contrast to thin or thick film microbatteries, 3D microbatteries are intended for use in applications which seek to utilize increased amounts of active materials at high rates. The use of 3D electrode designs compensates for low solid-state diffusion coefficients in active materials, and offers large surface area

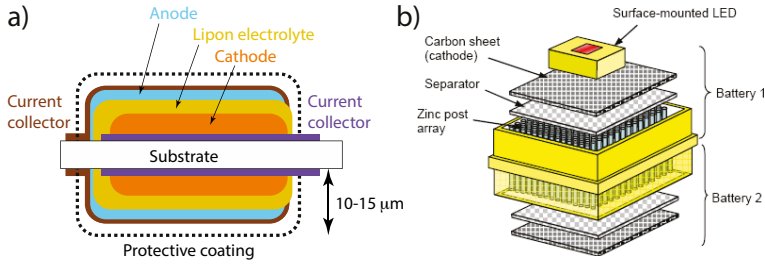


Figure 2.1. Schematic of a) the cross section of a thin film microbattery with both sides of the substrate coated in active materials and a solid electrolyte b) two Zn-air 3D microbatteries assembled in series and connected to an LED. The schematic in a) is redrawn based on the Ref [53] and the latter is reproduced from Ref [55] with permission from ©2007 IEEE

available for coating with sufficient amount of active materials. This strategy ensures a relatively larger areal capacity and sustainable power density. To date, a number of 3D geometries of current collectors have been explored as shown in *Figure 2.2* [1, 2, 52, 56–58]. The array of nanopillars is by far the most extensively studied electrode design and is fabricated by electrodeposition of metals through channeled membranes like anodized aluminium oxide (AAO), [56, 59, 60] or by carbonizing photoresists patterned by photolithography [61]. It has been claimed that this periodic electrode architecture suffers from non-uniform primary current distribution [62] which leads to local overcharge/discharge at high rates [2, 63]. Another similar configuration consists of concentric cylindrical current collectors coated conformally by one active material and an electrolyte layer with the remaining void filled by the second active material. Golodnitsky *et al.* developed microchannelled plates in which layers of current collectors, active materials and an electrolyte were deposited successively onto perforated substrates to form a mechanically robust 3D electrode configuration [58]. Highly porous electrodes based on aerogels, carbon foams and oxide nanotubes have also been developed for microbattery applications [1, 64–66]. These open structures are of beneficial use in that they offer large specific surface area, high porosity and buffering against volume changes occurring during cycling. Of particular interest are transition metal oxide aerogels endowed with adequate ionic and electrical conductivity. In a paper published in 2007, Long *et al.* described the fabrication of nanoscale battery composed of MnO_x ambipolar as a cathode, polymer electrolyte separator and RuO_2 nanoparticles as an anode [64, 67]. The success of this approach depends heavily upon the conductivity of the nanostructured aerogel framework, the ability to deposit a pinhole-free polymer electrolyte and the homogeneity of the back-filling component distributed at the exterior of the structure. Self-limiting electropolymerization [68], electroless deposition and

atomic layer deposition have been proposed as suitable techniques for these structures [64].

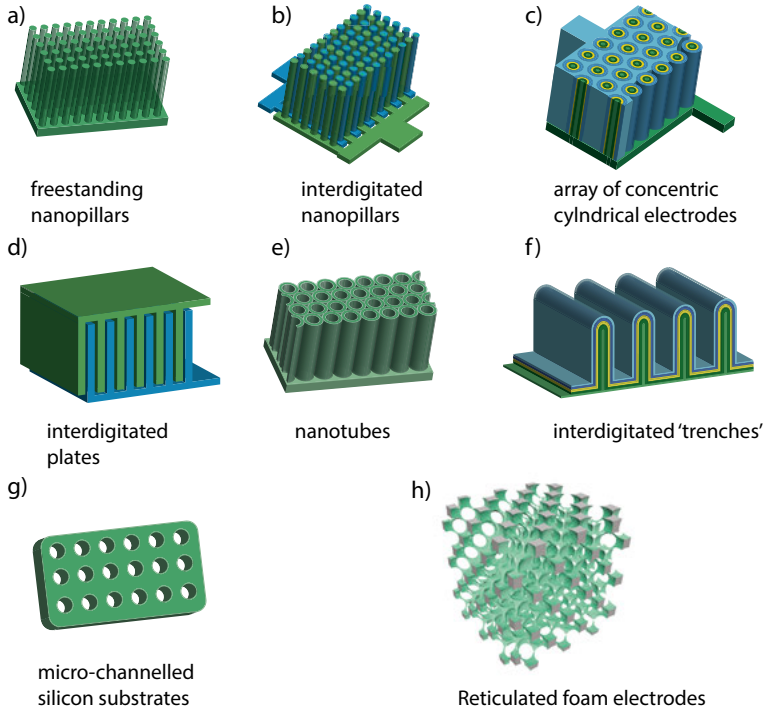


Figure 2.2. Schematic of the 3D electrode architectures proposed for use in microbatteries: a) high-aspect-ratio arrays electrode b) interdigitated arrangement of arrays for full-cell microbatteries c) concentric cylindrical array electrodes d) interdigitated planar electrodes for full-cell microbatteries e) vertically-aligned nanotubes f) interdigitated trench electrodes g) micro-channelled silicon substrates h) reticulated foam or aperiodic electrodes

2.1.2 High-aspect-ratio array electrodes

3D electrodes consisting of arrays of micro- and nano-pillars are the most widely studied architectures destined for use in microbatteries [52, 69–71]. Templates commonly utilized in the fabrication of self-supported metal and carbon posts are porous membranes such as AAO and perforated silicon wafers [71,72]. For instance, by electroplating through silicon molds, micro-machined by etching, high-aspect-ratio arrays of Zn pillars were prepared [70]. The schematic of the whole process is shown in *Figure 2.3*. In addition to micro-posts, periodically-organized trenches of metals were fabricated by electrodeposition through the appropriate silicon membranes [69]. Etching away the silicon template using XeF_2 gave rise to free-standing metal posts and trenches.

The high surface area available and the short ion diffusion pathlength in these electrode geometries can be exploited to design high performance microbatteries. For instance, Chamran *et al.* reported the use of 3D Zn micro-post electrodes in Zn-air microbattery [55]. A typical arrangement of the 3D electrodes in the cell is shown in Figure 2.1 b). The Zn anodes could be combined with $\text{Ni}(\text{OH})_2$ -coated micro-posts to form fully interdigitated a 3D microbattery [73]. In addition to metals, the fabrication of 3D carbon arrays were demonstrated using the same route [74]. A slurry of mesocarbon microbeads was infiltrated into the micro-channels of a silicon mold, which was subsequently removed by etching with XeF_2 . The free-standing carbon electrodes were suggested for 3D lithium-ion microbattery applications. Furthermore, the high-aspect-ratio Si microstructures could be utilized as substrates for other active materials or be used directly as 3D active materials in microbatteries [75, 76]. Nano-structured 3D array electrodes can be designed through

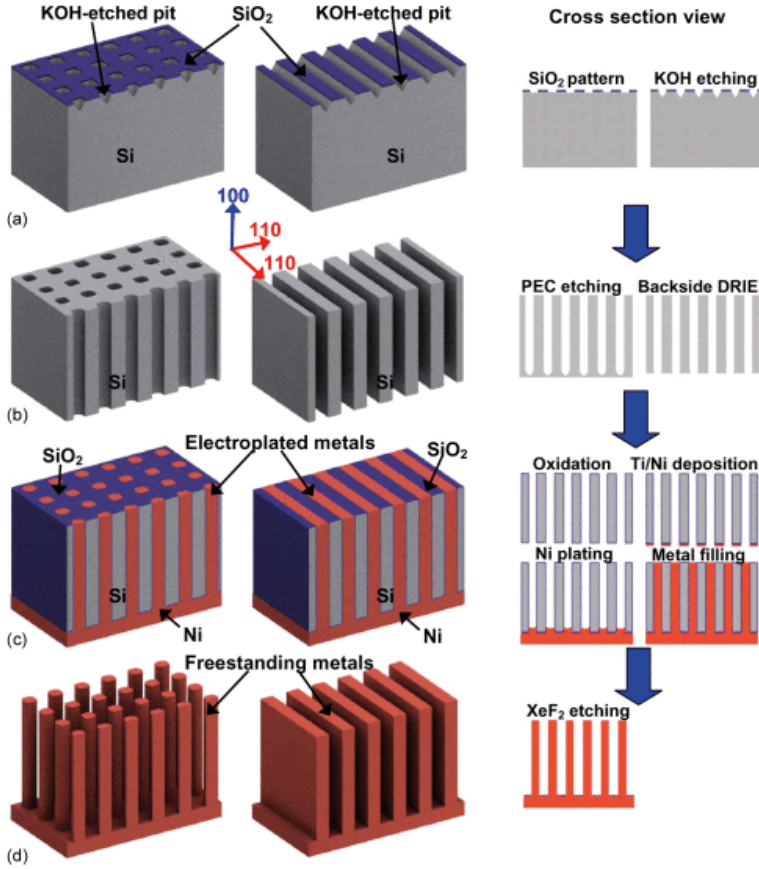


Figure 2.3. Schematic illustration displaying the process used to fabricate high-aspect-ratio metal micro-pillars and trenches. Reproduced from Ref [69] with permission from ©2011 IEEE

electrodeposition of metals in the pores of AAO membranes [71,72,77]. These electrode structures have so far been employed as supports for a wide variety of negative and positive active materials [56, 59, 78]. A full-cell 3D microbattery was realized by Liu *et al.* based on a single AAO template coated on both ends with active materials via atomic layer deposition (ALD) [79].

2.1.3 High-aspect ratio micro-channel electrodes

Micro-perforated silicon substrates have also been proposed as 3D electrode architectures for microbatteries [58,80–84]. The electrode fabrication involves etching channels or trenches into silicon wafers by means of photolithographic approach and deep reactive-ion etching [85]. The resulting electrode architectures were employed as 3D supports for a wide range of active materials. All-solid-state full-cell microbatteries have also been built based on both the micro-channel and trench geometries [58,85,86]. A typical electrode arrangements can be seen in the schematic given in *Figure 2.4*. Apart from semi-3D arrangements, a 3D-interlaced microbattery was developed by Ripenbein *et al.* based on a silicon substrate perforated on both ends, and then coated with active materials. The porous silicon wall in between acted as a separator [87]. Another similar approach advanced by Notten *et al.* consisted of trenches etched into silicon substrates that were readily coated with active materials and a solid electrolyte to build all-solid-state 3D microbatteries [81]. Like the silicon array electrode designs, this electrode geometries are also suitable to be integrated with the current microelectronic systems which are based on silicon-wafer technology.

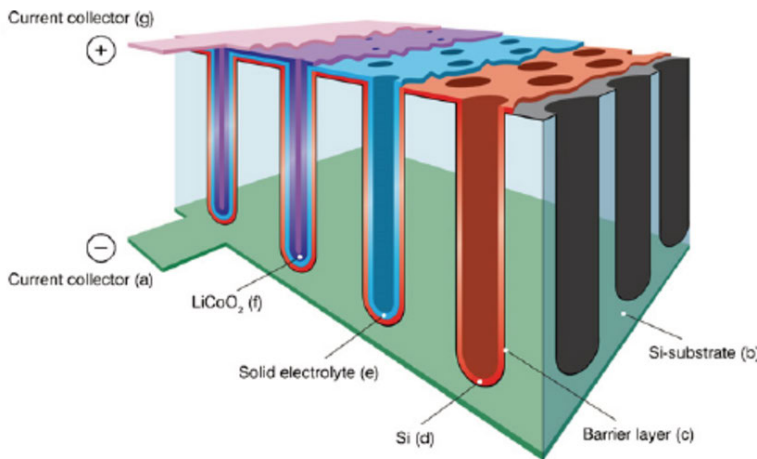


Figure 2.4. An all-solid-state 3D microbattery based on micro-channelled silicon substrate. Reproduced from Ref [86] with permission from ©2009 Elsevier.

2.1.4 Foam electrodes

Foam or 'sponge-like' architectures featuring networked voids with periodic and aperiodic arrangement have been pursued as alternatives to the electrode geometries discussed above [1, 64–66]. For an application as a 3D current collector, a porous electrode is required to be (a) fully networked to support electron flow throughout the electrode architecture (b) non-tortuous to facilitate ion transport with minimum ohmic drop (c) mechanically stiff to avoid detachment of the active materials during cycling (d) electrochemically stable in the working voltage window and (e) able to provide a high surface area available for coating with active materials and an electrolyte. Aperiodic 3D electrode designs made of carbon and metals have widely been explored and few examples are presented as follows. Reticulated vitreous car-

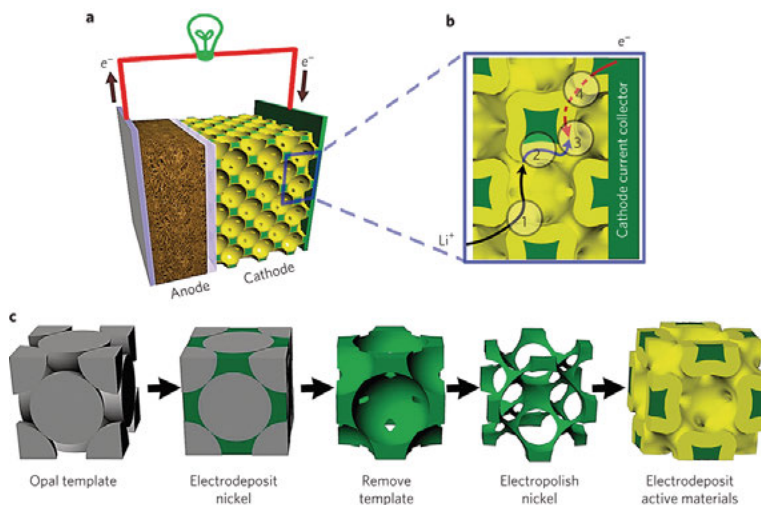


Figure 2.5. A schematic illustration of the fabrication of bicontinuous Ni-foam electrodes and the subsequent material deposition procedure. Reproduced from Ref. [88]. Permission to reuse granted by the ©2011 Nature Publishing Group

bon (RVC) foam has long been used as an electrode in electroanalytical studies and has been investigated for potential use as a 3D substrate for active materials in microbatteries. The latter use was demonstrated by Johns *et al.*, who electrodeposited a conformal coating of MnO_2 cathode on RVC [65]. Results indicated a substantial improvement in the electrochemical performance and footprint area capacity of MnO_2 as compared to planar geometries. These same RVC substrates were also coated in LiFePO_4 using a spin coating method where state-of-the-art footprint capacities and rate capabilities were observed [66]. Aside from glassy carbons, graphene foams have recently been tried as 3D substrates for battery materials and notably high rate performances have been reported [89–91]. However, these foam structures are not suited for 3D microbattery applications as the majority of the voids

therein are extremely large ($> 500 \mu\text{m}$). Another type of carbon foam can be prepared by nanocasting self-organized colloidal silica or polymer templates, and is commonly termed 3D ordered macroporous material or 3DOM for short. Following the first report in 1998 by Zakhidov *et al.* [92], 3DOM carbon foams have been synthesized from a variety of carbon precursors, and used in diverse electrochemical applications [93–95]. Notably, Lee *et al.* demonstrated that monolithic macroporous electrodes consisting of highly periodic pores could store lithium ions corresponding to a reversible gravimetric capacity of 299 mAh g^{-1} at 15.2 mA g^{-1} [94]. The electrodes were fabricated by carbonizing phenolic resin replicas of colloidal crystal templates based on poly(polymethyl methacrylate) (PMMA). A similar study made efforts to investigate the effects of hierarchical porosity and texture on the electrochemical performance of the anodes [96, 97]. To prepare the 3DOM electrodes, the authors pursued the common approach of nanocasting monoliths of silica as templates for phenol-formaldehyde resins, which were in turn carbonized to yield carbon foams [97]. Metal foams are also potential contenders as 3D substrates in microbatteries. Especially, over the last few years the use of metallic 3DOMs as 3D current collectors has received significant attention. For instance, Zhang *et al.* reported the electrodeposition of nickel through colloidal crystal templates to generate bicontinuous electrode structures, and deposited NiOOH and MnO_2 active materials for use in NiMH and Li-ion batteries, respectively [88]. A schematic description is given in *Figure 2.5*. Perhaps, the most relevant applications of such electrodes was later demonstrated in the same research group [98]. Though, nothing novel was reported as regards materials selection, the work presented an ingenious electrode design consisting of interdigitated arrangement of 3DOM Ni scaffolds which were coated in negative and positive active materials.

2.2 Materials selection and deposition

The next crucial stage in developing 3D microbatteries after electrode fabrication is the deposition of current collectors (if needed), active materials, and electrolytes making use of a variety of strategies. The most common approaches are atomic layer deposition [56, 83, 99], physical vapor deposition (PVD) [100], chemical vapor deposition (CVD) [101], pulsed laser deposition [102, 103], RF-sputtering [104–106], sol-gel processing [107], electrodeposition [52, 65, 78], electrostatic spray pyrolysis [108], and dip-spin coating [66]. Like conventional batteries, microbatteries rely on a selection of active materials based on all types of energy storage mechanisms including lithium ion insertion, conversion, and alloying. A schematic of the mechanisms is shown in *Figure 2.6*. Insertion-based materials such as LiFePO_4 [107], LiCoO_2 [100, 106], LiMn_2O_4 [109], $\text{Li}(\text{NiMnCo})_{1/3}\text{O}_2$ [105], TiO_2 [104], and MnO_2 [64] have widely been used in microbattery electrodes. Elec-

trochemical energy storage based on alloying in Si [80,110], and Sn [111], and conversion reactions in Fe_3O_4 [72], Cu_2O [77], and *et cetera* have also been utilized in various electrode configurations of microbatteries.

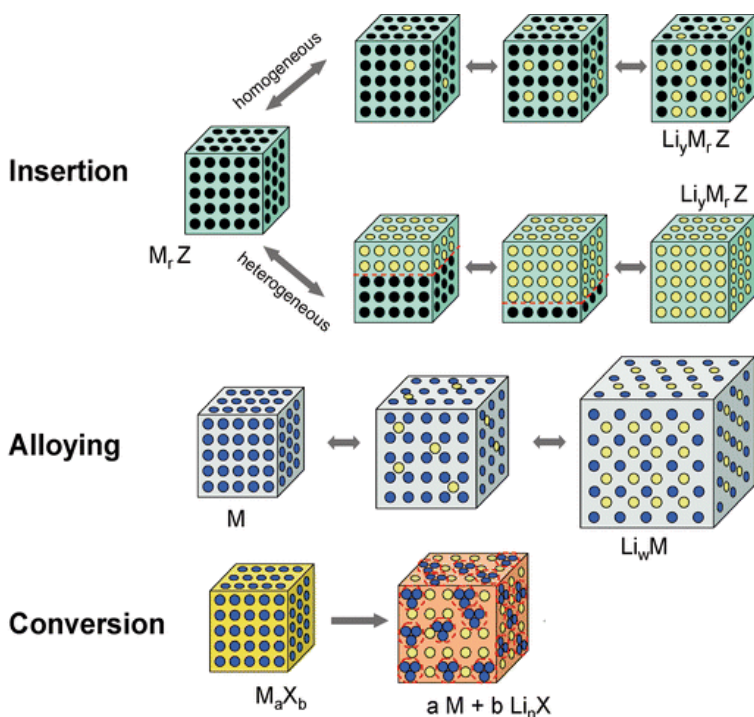


Figure 2.6. A schematic illustration of the different reaction mechanisms which underlie the electrodes of lithium and lithium-ion batteries. The black, blue, and yellow circles represent vacancies in the crystal structure, the metal, and lithium (lithium ions), respectively. Adapted from Ref. [112] by permission of ©2011 The Royal Society of Chemistry

Apart from the redox active materials, electrolytes constitute the integral part of microbatteries as well. Unlike thin film microbatteries, which contain thin layers of solid electrolytes [53, 113], most 3D microbatteries use liquid electrolytes. The liquid electrolyte consists of lithium salts dissolved in a mixture of organic solvents. Current efforts focus on the development of solid electrolytes for 3D microbatteries. Solid electrolytes are by and large of two types. Those based on lithium salts dissolved in polymer matrices [114, 115], which are known as polymer electrolytes, and those made of ceramic ionic conductors [116]. Solid ionic conductors are usually composed of mobile lithium ions occupying specific sites in crystalline solids. Significant achievements have been gained recently in terms of producing solid electrolytes possessing high ionic conductivities that can rival or even exceed those of liquid electrolytes, thermal stability, wide electrochemical window (0 to 5 V)

and no risk of fire and health hazards [116, 117]. These favorable characteristics enable solid electrolytes to be used in combination with high voltage cathodes and metallic lithium with minimal risk of side reactions and thermal runaway. Thus, all-solid-state batteries incorporating these electrolytes can promise superior energy and power densities, long cycle life and low safety risks. Even so, ceramic electrolytes are too brittle to be applied on 3D electrode designs; thus, their use has so far been limited to thin film (micro)batteries [113, 118, 119]. Mostly, solid electrolytes based on polymeric matrices are promising for 3D microbattery applications [115, 120, 121].

3. Synthesis of Carbon Foams from Emulsions

This chapter presents the results obtained on the various aspects of the synthesis and characterisation of emulsion-templated carbon foams. It begins with discussing the strategies used to produce the carbon foams and to optimize their specific surface areas, porosity, microstructures and chemistry. The chemical transformations involved during pyrolysis at various temperatures and their bearing on the pore microstructures, surface chemistry and degree of graphitization of the resulting carbon foams are discussed in details.

3.1 Overview of emulsion-templated carbon foams

Carbon foams are sponge-like carbon structures consisting of reticulated open-celled macropores with interconnecting windows. A number of synthesis strategies have been developed in order to synthesize monolithic carbon foams. Often, carbon foams are obtained from the pyrolysis of pitches [122], pre-formed polymer foams [123], and polymer foams prepared via phase separation [124, 125], gas-foaming [126], colloidal crystal-templating [127] and nanocasting [97, 128, 129]. In this section, a state-of-the-art review is presented on the carbon foams derived from high internal phase emulsion polymers (polyHIPEs).

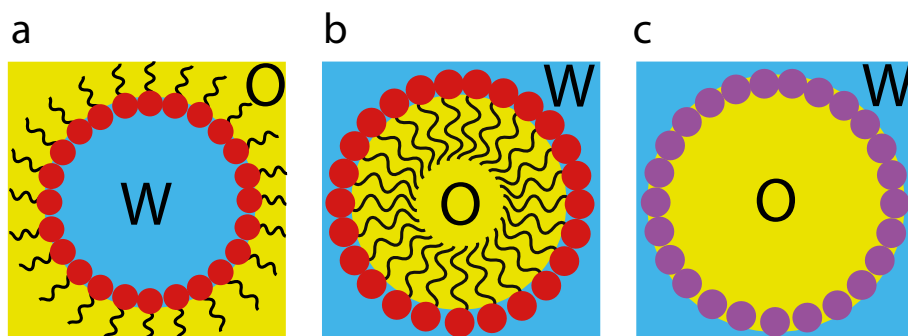


Figure 3.1. Schematic of simple high internal phase emulsions (HIPEs), namely a) water-in-oil, b) oil-in-water, and c) Pickering HIPEs. The symbols 'O' and 'W' stand for oil phase, and water phase. The red circles are surfactants and the purple circles in c) represent particle stabilizers.

3.1.1 Polymerization and pyrolysis of high internal phase emulsions

A high internal phase emulsion (HIPE) is a generic term that encompasses a class of concentrated emulsions that form upon mixing two immiscible liquids in the presence of interface stabilizers like surfactants [130–135]. Based on the formulation of the constituent liquids and surfactants, various types of HIPEs can be prepared: water-in-oil [130,133,136–138], oil-in-water [136,139–144], and Pickering HIPEs [145]. A schematic description of the three HIPE is given in *Figure 3.1*. The first kind of HIPE is formed when a substantially higher proportion of an aqueous phase is blended with an organic phase with the help of a suitable surfactant. The aqueous phase is usually composed of a stabilizing salt and an initiator to start off the polymerization of the monomers dissolved in the organic phase. In essence, the continuous organic phase forms the solid polymer network while the aqueous internal phase provides templates to create pores. In contrast, in oil-in-water HIPEs the polymerization occurs in the aqueous phase around the template formed by the droplets of the organic phase. Evaporation of the internal porogen phase yields cellular porous polymers with hydrophilic surfaces. Lastly, pickering HIPEs use solid particles to stabilize the emulsions instead of soluble surfactants [146]. All types of high internal phase emulsion polymerization have been used to prepare monoliths of highly porous polymers that have been used to synthesize carbon foams. The porogens are the liquid droplets which constitute the internal phase and assemble to form close-packed templates of deformed polyhedra, which are in turn surrounded by the polymerizing continuous phase [130–132]. As the monomers in the continuous phase polymerize, the droplets in the internal phase evaporate leaving pores in their stead. Thus, highly porous polymer foams form. Various types polymerization reactions can occur in the continuous phase. Most common reactions include radical polymerization [130,133,136,137], photo-induced polymerization [147–151], polycondensation [152,153], ring-opening metathesis polymerisation (ROMP) [154,155], and reversible addition-fragmentation chain transfer polymerization (RAFT) [156]. Subsequent post-synthesis functionalizations [157] may be needed to render the polymers thermally resistant against degradation [158] thereby increasing the char-content obtained after pyrolysis [137,159]. Various types of polyHIPEs have been utilized to prepare carbon foam monoliths, which are sometimes known as CarboHIPEs. Below are some examples of carbon foam monoliths that are derived from polyHIPE templates.

3.1.2 Carbon foams from water-in-oil polyHIPEs

An archetype of porous polymers derived from water-in-oil HIPEs is based on styrene and its derivatives as monomers. In the first-ever report made by

Unilever [160], styrene, divinylbenzene, and vinylbenzyl chloride were used as monomers to prepare highly cross-linked and low density monoliths of polyHIPEs. A modification of the same recipe has been employed to prepare porous polymer precursors for the synthesis of carbon foams. For instance, Wang *et al.* demonstrated that styrene-based polyHIPEs can be utilized to prepare highly porous carbon foams, and presented detailed data on the chemical composition and mechanical strength of the resulting carbon foams [137]. Since polystyrenes lack sufficient thermal stability, post-synthesis crosslinking had to be carried out via sulfonation using concentrated sulfuric acid and acetylsulfates. A schematic synopsis of the whole process is given in *Figure 3.2* to illustrate the various steps involved in the fabrication of polyHIPE-derived carbon foams. These types of carbon foams are characterized by unique features that define their open porosity, network structures, structural hierarchy and physico-chemical properties. The BET specific surface areas of these carbon foams can reach beyond $600 \text{ m}^2 \text{ g}^{-1}$. Other polymers have also been used to prepare carbon monoliths. Crosslinked polyacrylonitrile polyHIPEs were made use of by Cohen *et al.* to fabricate carbon foams with a BET specific surface area of $26.5 \text{ m}^2 \text{ g}^{-1}$ and consisting of largely interconnected macropores decorated with mesopores in their walls [138]. Depending on the pyrolysis temperature, PAN polyHIPEs can be used as precursors to synthesize nitrogen-containing carbon foams that are potentially attractive for use in catalysis, for instance. Other similar examples of polyHIPE precursors include Poly(1,1-dichloroethene) [161].

3.1.3 Carbon foams from oil-in-water polyHIPEs

As stated above, this class of polyHIPEs is derived from emulsions in which the polymerization of the monomers takes place in the aqueous phase. At the same time the evaporation of the organic phase leaves behind extended porosity. Typical examples include resorcinol-formaldehyde (RF) polyHIPEs. The carbonization of RF polyHIPEs produces carbon foam monoliths characterized by hierarchical structure consisting of large macropores and mesopores, as evidenced by Hg-porosimetry and N_2 physisorption. [153] In effect, the carbon foams contained mesoporosity usually associated with aerogels derived from RF-resins [162] and large macroporosity typical of polyHIPEs. Such type of carbon foams are not readily prepared through traditional routes. Using similar strategy, Szczurek *et al.* prepared carbon foams from tannin-based polyHIPEs [144]. The oil-in-water HIPE was obtained from an aqueous solution of tannin, hexamethylenetetramine as a crosslinker, p-toluene sulphonic acid (pTSA) as an initiator and Kolliphor® ELP as an emulsifier, and an internal droplet phase composed of sunflower oil. Polycondensation in the continuous aqueous phase and extraction of the oil phase with acetone yielded polyHIPEs that were subsequently carbonized to monoliths of carbon foams.

Studies on the porosity, surface areas, and some applications of emulsion-templated carbon foams can be found in the literature [163–166]. Monolithic silica polyHIPEs have also been synthesized by hydrolysis of tetraethylorthosilicate (TEOS) in an oil-in-water HIPE and further used as templates to prepare carbon foams with an inverse replica structures [167].

3.1.4 Carbon foams from Pickering polyHIPEs

In Pickering HIPEs surfactants are substituted by solid particles which are able to adsorb onto the hydrophobic-hydrophilic interface to stabilize the emulsion. [146] Commonly used particle stabilizers are TiO_2 [146], SiO_2 [168, 169], Al_2O_3 [168], Fe_2O_3 [168], poly(styrene-co-methacrylic acid) (PS-co-MAA) latex particles [170], poly(N-isopropylamide-co-methacrylic acid) (PNIPAM-co-MAA) microgel particles [171], poly(urethane urea)-(vinyl ester resin) (PUU-VER) nanoparticles [172], metal organic frameworks (MOF) [173–175], and carbon nanotubes [176]. Upon polymerization, porous polymers, aptly termed Pickering polyHIPEs, are formed, which afterwards serve as templates for preparing carbon foams [177, 178]. Both the polymers and the carbon foams derived therefrom feature networked structures of cellular voids [177, 178]. Additional pores and increased specific surface areas can be generated in the structures by physical or chemical activation [178]. Carbon foam monoliths with relatively open-cell frameworks and multi-scale porosity were prepared using poly(Si-HIPE) obtained from Pickering oil-in-water emulsions [179].

3.2 Synthesis procedure

The research projects covered in this thesis are based on carbon foams derived from styrene-based polymer foams which arise from the polymerization of water-in-oil HIPEs. Two general objectives have been set in relation to the fabrication of hierarchically porous carbon foams and their use in microstructured batteries.

In the first instance, the aim was to fabricate 3D electrodes that can be employed in microbatteries as hosts for lithium ions and as substrates for other active materials in lieu of commercial carbon foams. To begin with, the HIPEs were prepared at 1300 rpm using magnetic stirrer. A high internal phase emulsion was prepared according to Wang *et al.* [137] by mixing, under constant stirring, an oil phase containing styrene (6 mL, Sigma-Aldrich®, $\geq 99\%$), divinylbenzene (3 mL, Aldrich®, 80%), 4-vinylbenzyl chloride (1 mL, Fluka®, $\geq 90\%$) and Span 80 (3 g, Sigma®) as a surfactant and a droplet-forming aqueous solution of $\text{CaCl}_2 \cdot 2\text{H}_2\text{O}$ (1.65 g, Sigma-Aldrich®, $\geq 99\%$) and $\text{K}_2\text{S}_2\text{O}_8$ (0.15 g, Merck®, 99%) initiator in distilled water (60 mL). The emulsion was stirred vigorously for several minutes before being transferred to a PTFE mold and stored in an oven at 65 °C for 48 hours to polymerize. Afterwards, pieces

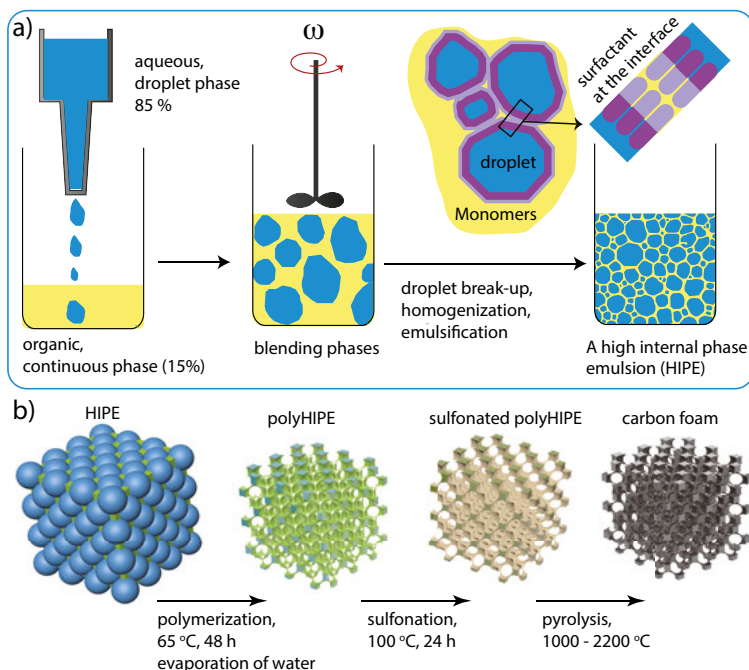


Figure 3.2. Schematic illustrations displaying the steps involved in the a) preparation of a high internal phase emulsion (HIPE) and b) the subsequent polymerization, sulfonation and pyrolysis to fabricate monoliths of carbon foams. An HIPE forms when a sufficiently hydrophobic organic phase containing monomers and a surfactant is blended with a much higher proportion of aqueous phase ($> 80\%$ by volume) composed of a stabilizing salt and an initiator. Polymerization of the monomers and evaporation of the aqueous internal (droplet) phase yield porous polymers, which are sulfonated and then pyrolyzed to carbon foams.

of the polymer were immersed in distilled water (24 h, $90\text{--}100\text{ }^{\circ}\text{C}$) and absolute ethanol (48 h, $70\text{ }^{\circ}\text{C}$) to leach out the stabilizing salt, the initiator residues and the surfactant. Prior to carbonization, the polymers were functionalized with concentrated H_2SO_4 . Clean pieces of polymers were sulfonated at $100\text{ }^{\circ}\text{C}$ for 24 hours. The sulfonated polymers were then carbonized at a range of temperatures (700 to $1500\text{ }^{\circ}\text{C}$) in alumina boats in a tube furnace (Heraeus® Tube Furnace) under a constant flow of inert gasses (Ar or N_2). A generalized schematic representation of the synthesis procedure is given in *Figure 3.2*. The temperature program used for stepwise pyrolysis of the sulfonated polymers is shown in *Figure S1* in Paper I.

Secondly, efforts have been directed towards optimising the specific surface areas, void size distributions, and degree of graphitization. Keeping all synthetic conditions same, the aqueous and organic constituents of the HIPEs were blended using a rotor-stator homogenizer. In *Figure 3.3*, a pictorial summary of the procedure is given. The volumes of the two phases were 5 times

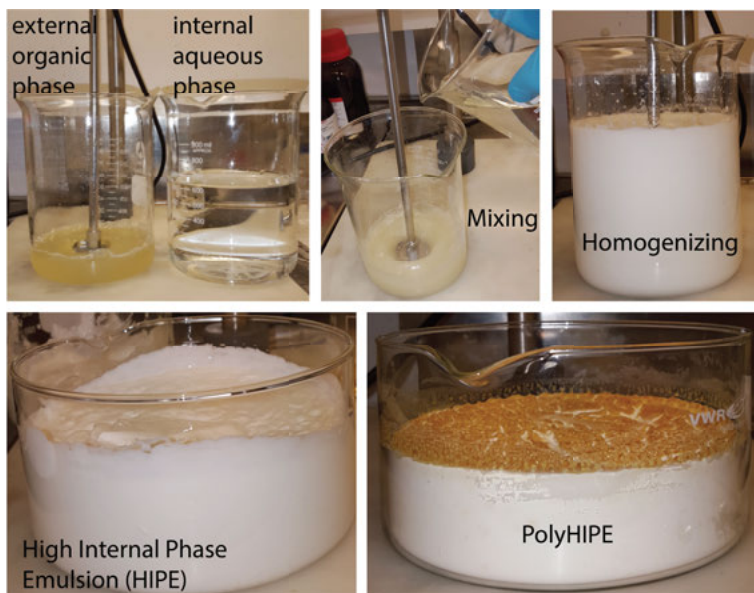


Figure 3.3. A photographic summary of the preparation and polymerization of a high internal phase emulsion.

higher than those given in the recipe above. By varying the the rotor angular velocity (ω), different droplet size distributions in the HIPEs and hence void size distributions in the resulting polyHIPEs could be achieved. After the usual washing steps and sulfonation process as described above, the sulfonated polymers were carbonized at 1000 °C in a quartz tube furnace under a constant flow of Ar. The as-prepared carbonfoams were further heated in a graphite furnace in order to improve their degree of graphitization. Cylindrical graphite crucibles (MTI[®]) were used as sample holders. The carbon foams were heated at 1500 and 2200 °C. A series of techniques including gas physisorption analysis, electron microscopy, Raman and X-ray photoelectron spectroscopy, powder X-ray diffraction were employed to fully characterize the properties of the carbon foams as a function of heating temperature. Most importantly, the consequence of higher pyrolysis temperature on the electrochemical performance of the carbon foams was investigated.

3.3 The microstructure of emulsion-templated polymer and carbon foams

As discussed in the previous chapter, fabrication of the carbon foams begins with the preparation of high internal phase emulsions (HIPEs). Monoliths of porous and cellular polymers are obtained after polymerising the HIPEs. After sulfonation with concentrated H_2SO_4 , the polymers are heated at various

temperatures to prepare carbon foams. In Paper II, acetylsulfate was used as the sulfonating agent instead of concentrated H_2SO_4 . The scanning electron micrographs (SEM) of the polymer (electron beam 3 keV), the sulfonated polymer (3 keV) and the carbon foams (5 keV) are shown in *Figure 3.4*. It can be noted that the granular and porous surface of the polymer is preserved through the sulfonation and carbonization steps. This porosity accounts for the surface area which was assessed using nitrogen gas physisorption method. Transmission electron microscopy was used to characterize the topography,

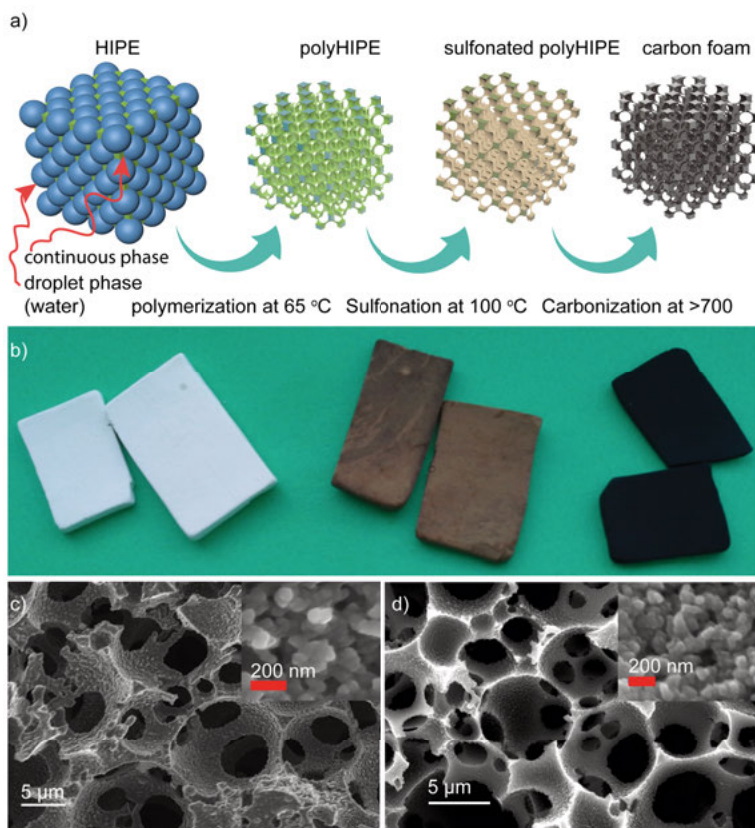


Figure 3.4. Polymerisation and carbonization of HIEs a) An idealized schematic represents the synthesis of a carbon foam from a high internal phase emulsion polymer (polyHIPE®). b) Photographs of the polymer, the sulfonated polymer and the carbon foam (shown from left to right). c) and d) are the SEMs of the sulfonated polymer and the carbon foam, respectively. Reproduced from PaperI with permission from ©2016 John Wiley & Sons

morphology, porosity and microscopic structure of the carbon foams as a function of pyrolysis temperature. In *Figure S5* in Paper I, the scanning transmission electron micrographs (STEMs) are shown for the carbon foams prepared at temperatures from 650 to 1500 °C. Since STEM is sensitive to mass, atomic

number and thickness contrast, it is possible to study the 3D topography and porosity of the carbon foams. Due to mass contrast, the pores appear darker in the micrographs as compared to the carbon, which is brighter. The pores are clearly visible at the edges of the carbon foam struts which are thinner and thus the electron beam can pass through with little or no multiple scattering. All in all, the carbon foams display a wide pore size distributions: micrometric voids with highly porous and rough surfaces. The microstructures of the emulsion-templated polymer and carbon foams are characterised by networks of voids (macropores) which are interconnected with each other through windows, as indicated in *Figure 3.5* Based on manual measurements on the SEMs, the distributions of void and window sizes have been evaluated for both samples. The plots are given in *Figure 3.6 d)* and *e)*. In general, both the voids and windows undergo substantial contraction as a consequence of pyrolysis at elevated temperatures, *i.e.*, the carbon foams possess smaller voids and windows.

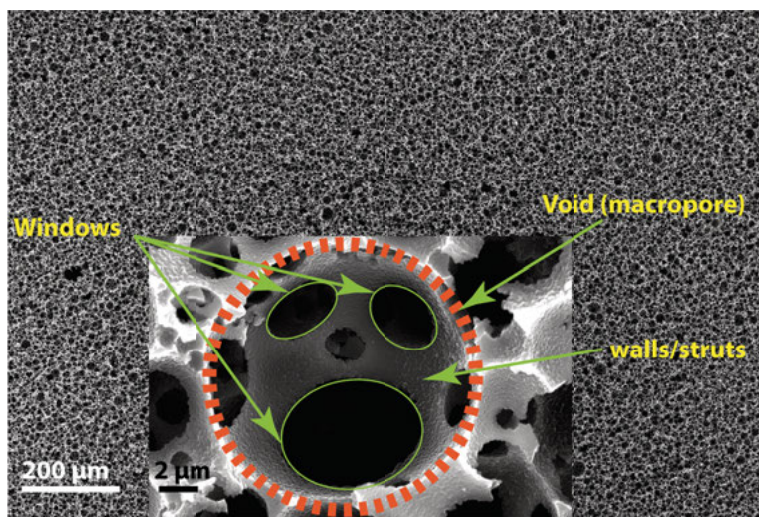


Figure 3.5. A secondary electron scanning electron micrograph (SEM) of the carbon foam synthesized by carbonizing a sulfonated polymer at 1000 °C. The inset SEM shows the main geometrical features which characterise the carbon foam monoliths such as voids, interconnecting windows and struts.

The specific surface area and porosity (with pore width below 100 nm) were evaluated based on the N_2 -gas sorption isotherms provided in *Figure 3.6*. Accordingly, the polymers and the carbon foam are hierarchically porous in that the walls of the voids are interspersed with much smaller pores: mainly mesopores and macropores are observed. The presence of micropores is attested by the t-plot method. The specific surface areas could easily reach as high as $600 \text{ m}^2 \text{ g}^{-1}$, as reported in Paper I. Furthermore, more microporosity can be generated inside the macropores by means of chemical or gas-phase ac-

tivation, raising the specific surface area to about $1400 \text{ m}^2 \text{ g}^{-1}$ [178]. Such microstructural hierarchy is very rare in commercial carbon foams. Hence, emulsion-templated polymers can be used to manufacture carbon foams possessed of much lower void sizes, hierarchical porosity and thus high specific surface areas.

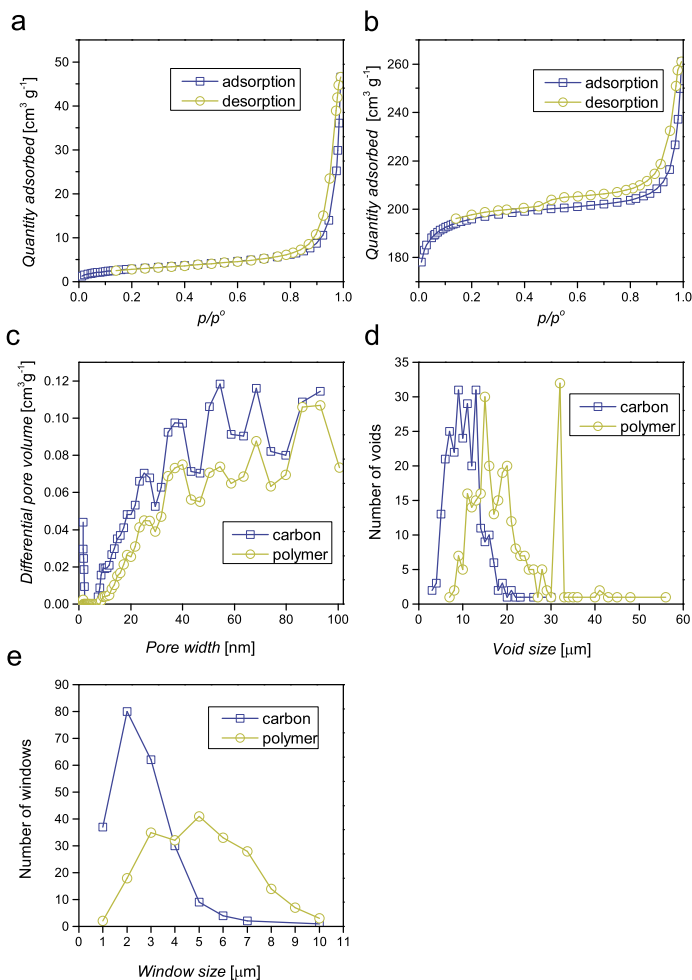


Figure 3.6. Assessment of the specific surface areas and porosity of the sulfonated polymer and the carbon foam derived therefrom based on nitrogen gas physisorption. (a) and (b) represent the adsorption-desorption isotherms of the sulfonated polymer and the carbon foam. (c) shows the pore size distribution of the two porous materials evaluated based on the respective isotherms provided in (a) and (b). (d) and (e) represent the void (large macropore) size distributions evaluated manually on the scanning electron micrographs.

3.4 Optimizing surface area and porosity

As described in detail in the preceding sections, a high internal phase emulsion (HIPE) can be polymerized to prepare porous polymers characterised by extensively networked voids and windows [130, 157]. The pyrolysis of the polymers has become an attractive approach to synthesize carbon foams with void dimensions much smaller than commercial carbon foams [137]. In this work, efforts have been geared specifically to optimize the void sizes and specific surface areas. Obviously, the void sizes in the polymer and, hence, the carbon foams are dependent on critical sizes of the droplets in the internal phase of the HIPE precursor. It is well-known that parameters like blend-

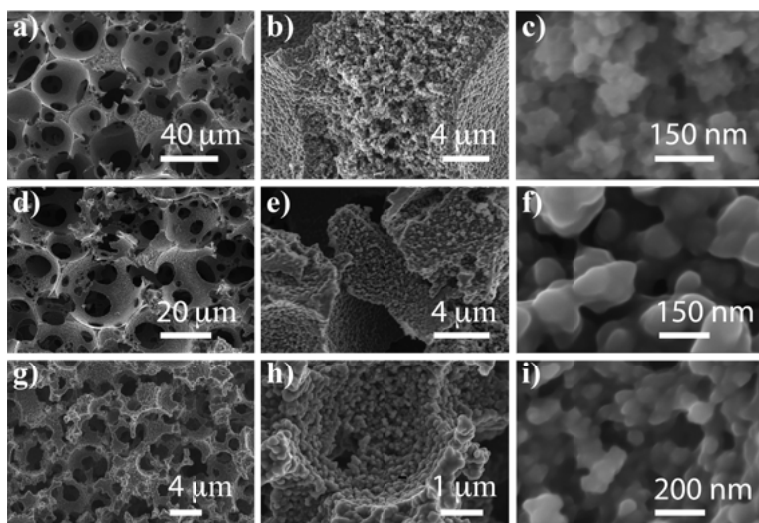


Figure 3.7. The scanning electron micrographs (SEMs) display the pore microstructures and detailed surface morphologies of the sulfonated polymers derived from HIPEs prepared at different mixing or homogenizing angular velocity. The micrographs show from a) to c), d) to f), and g) to i) corresponding to the polymers prepared at 500, 1000, and 2000 rpm, respectively.

ing shear rate (γ) or angular velocity (ω), viscosity of the continuous phase (η_{con}), temperature (T), the partition coefficient of the surfactant, the interfacial surface tension coefficient (σ), and the composition of the HIPE play significant roles in controlling the critical size (R_{crit}) of the droplets in the internal phase [133, 180–182]. Qualitative prediction of R_{crit} [180–182] may be formulated making use of these parameters as shown below

$$R_{crit} \propto C_a \frac{\sigma}{\eta_{con} \gamma} \approx C_a \frac{\sigma}{k \omega \eta_{con}} \quad (3.1)$$

where C_a , and k represent, respectively, the capillary number and the form factor used to relate the angular velocity (ω) of the homogenizer (rotor-stator)

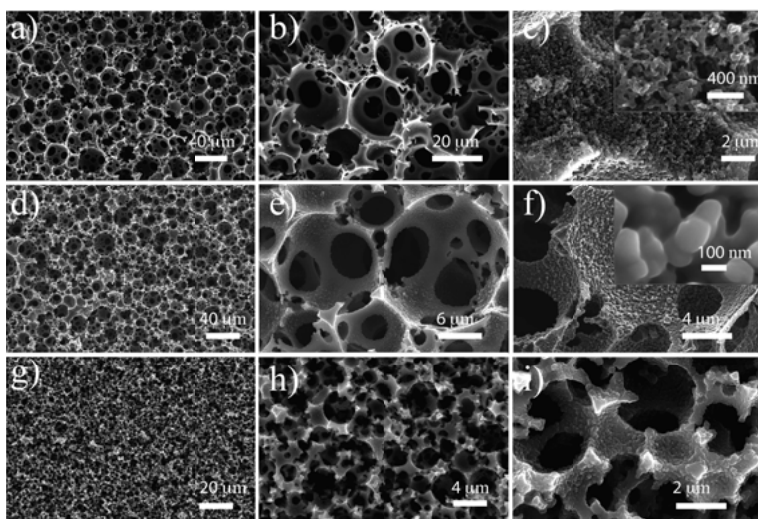


Figure 3.8. The scanning electron micrographs (SEMs) display the pore microstructures and detailed surface morphologies of the carbon foams obtained after pyrolysis of the corresponding sulfonated polyHIPEs at 1000 °C. The micrographs are shown for a) to c) for 500 rpm, d) to f) 1000 rpm, and g) to i) 2000 rpm. The insets in c) and f) provide closer inspection into the granular and porous features of the carbon foams.

to the shear rate (γ). Accordingly, a highly hydrophobic continuous phase and surfactant, and a higher shear rate (angular velocity) lead to HIPEs with small droplet sizes. In our study, the angular velocity of the homogenizer was varied from 500 to 2000 rpm. The influence of HIPE preparation on microstructures of the polymers and carbon foams is visible in the SEM images shown in *Figure 3.7* and *Figure 3.8*. Based on the SEM images of the polymer and

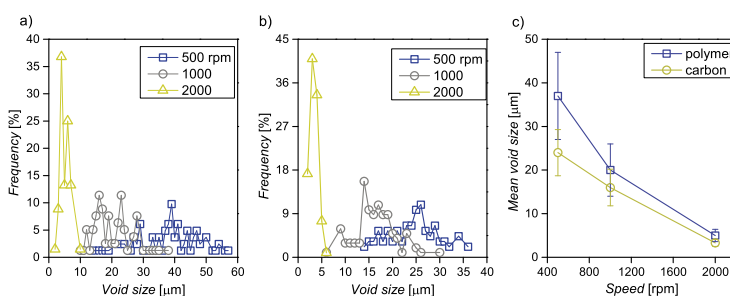


Figure 3.9. The size distributions of the voids in the a) sulfonated-polymers and b) carbon foams are evaluated manually on the respective scanning electron micrographs (SEMs) of each material derived HIPEs prepared at 500, 1000, and 2000 rpm angular velocity of the homogenizer. The plots in c) present the mean size of the voids as a function of the angular velocity. Each value is given along with its error bars showing the standard deviation.

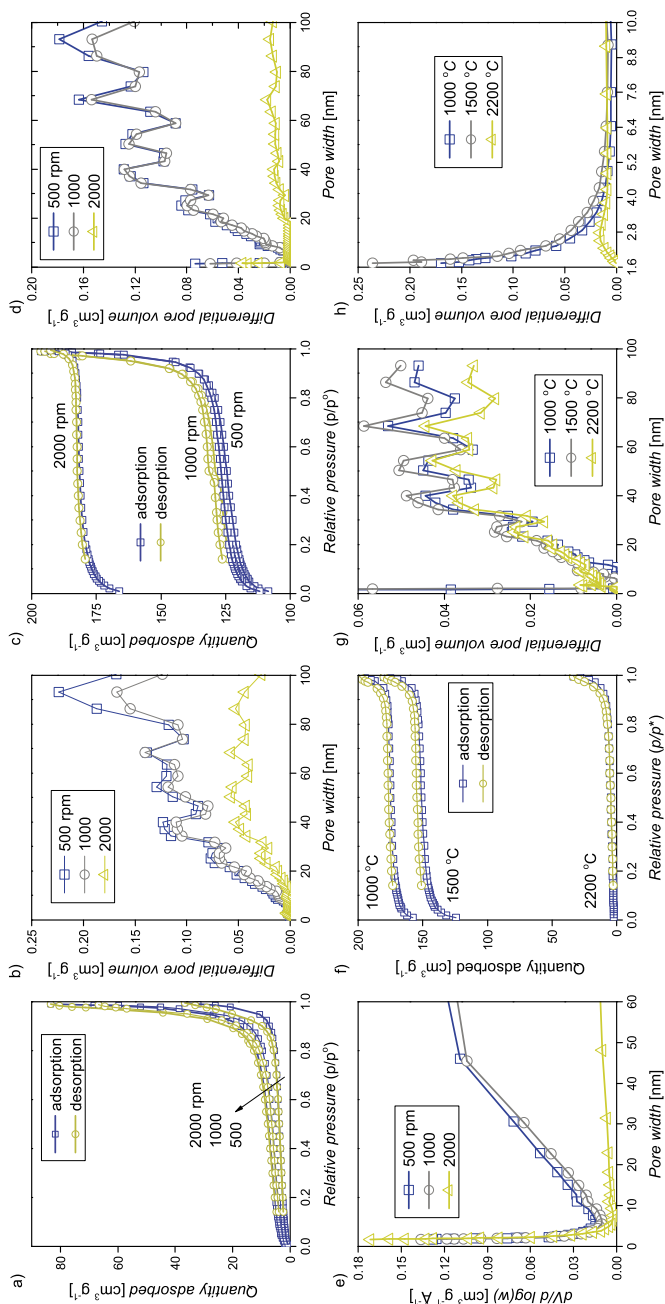


Figure 3.10. The BET specific surface areas and pore sized distributions of the polymer and carbon foams prepared at different homogenization speeds and pyrolysis temperature were evaluated using N_2 -gas physisorption analyses at 77 K. a) The adsorption-desorption isotherms of the polymer foams obtained by polymerizing the HIPEs prepared at 500, 1000, and 2000 rpm. b) The corresponding pore size distributions are assessed from the isotherms based on DFT kernels. After pyrolysis of the polymers at 1000 °C, carbon foams with higher specific surface areas and pore volumes are obtained as can be seen in the c) adsorption-desorption isotherms and d) the DFT pore size distributions. In e) the zoomed view of the curves of the pore size distribution shows that the carbon foams obtained from the 2000 rpm polymers has the highest meso-porosity. Further variation in the specific surface areas and porosity of the carbon foams in consequence of pyrolysis at different temperatures (1000, 1500, and 2200 °C) are seen. The f) adsorption-desorption isotherms, g) DFT pore-size distributions, and h) BJH (Barrett-Joyner-Halenda) pore size distribution which indicate that the BET specific surface areas and meso-porosity decrease significantly with increasing pyrolysis temperature.

carbon foams, one can conclude that there is strong correlation between the HIPE preparation and the microstructures of the voids. The void (macropore) size distributions of the polymer and carbon foams have been evaluated manually from the corresponding SEMs and can be observed in *Figure 3.9*. As expected, the void sizes decrease with increasing rate of HIPE homogenization. The distribution is also observed to get narrower as ω increases from 500 to 2000 rpm. The pore characteristics and specific surface areas of the carbon foams can be observed in *Figure 3.10*. A summary on the N_2 physisorption analyses is also provided in *Table S1 to S3* in Paper **III**.

3.5 Chemical transformations during pyrolysis

The sulfonation of polymers to enhance the thermal stability has become a common practice in the synthesis of carbon materials from polymer precursors. In this section and Paper **I**, a thorough scrutiny is performed to find out the actual role of sulfonation during the pyrolysis of polymers [125, 137].

To begin with, *in situ* infrared spectroscopy was carried out to monitor the pyrolysis of the pristine and the sulfonated polymers. The IR spectra, given in *Figure 3.11*, were collected for both samples at various temperatures using diffuse reflectance FTIR spectrometer. A summary of the experimental set-up is shown in *Figure S3* in the supporting document of Paper **I**. The IR absorption vibrations that are observed in the region ranging from 900 to 690 cm^{-1} can be assigned to out-of-plane bending $-\text{C}-\text{H}$ and $-\text{C}-\text{C}-$ vibrations and indicate the presence of both mono- and di-substituted benzenes [183–185]. After sulfonation, strong absorption bands emerge in different regions of the spectrum in addition to those of the pure polymer [125, 185]. The bands point to the presence of $-\text{OH}$, signified by the broad band around 3600 to 2600 cm^{-1} and $-\text{SO}_3\text{H}$ groups giving rise to the sharp peaks at 1361 and 1169 cm^{-1} due to asymmetric and symmetric stretching vibrations of $-\text{SO}_2-$ [125, 185–189]. When the sulfonated polymer is heated at 250 °, the intensity of the sulfonic acid functionality diminishes and the vibration band gets sharper signifying that it has undergone chemical transformation. It is likely that the sulfonic acid group has converted to sulfones as evidenced by the $-\text{SO}_2-$ stretching vibrations around 1358 (asymmetric) and 1176 cm^{-1} (symmetric) [185, 187, 188]. Further increase in the temperature of pyrolysis goes to show that the bands due to the sulfones cease to exist which indicates in turn that a completely different functional group has formed. This is likely due to the deoxygenation of the sulfones to yield thioether $-\text{C}-\text{S}-\text{C}-$ crosslinks [189, 190], which lack specific vibrational frequencies in the IR spectra [185]. Further analyses were undertaken using X-ray photoelectron spectroscopy and x-ray absorption near-edge fine structure spectroscopy.

The magnitude of the binding energy of a given photoelectron is affected by the oxidation state of the ion from which it is removed. Thus, XPS helps

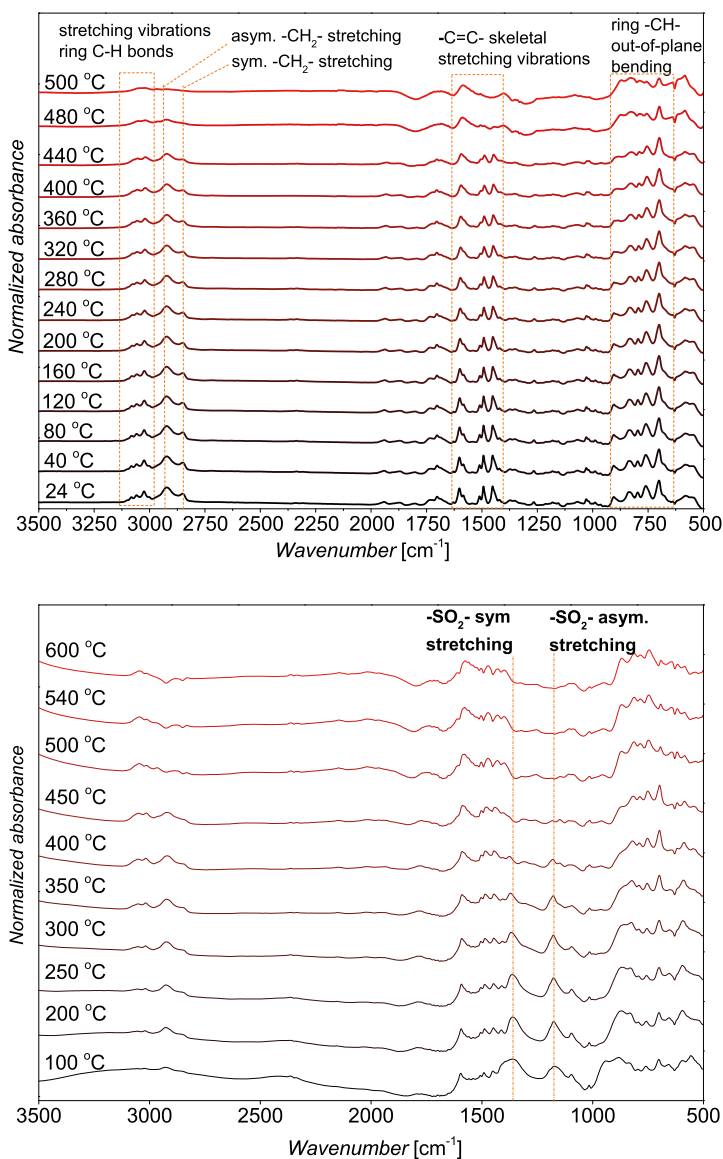


Figure 3.11. In situ infrared spectroscopy is used to monitor the course of pyrolysis of the polymers. (a) IR spectra of the pure polyHIPE polymer show the most common bands characteristic of polystyrene (b) IR spectra of the sulfonated polyHIPE at various temperatures. The bands which correspond to $\text{--SO}_2\text{--}$ stretching vibrations are designated by parallel lines.

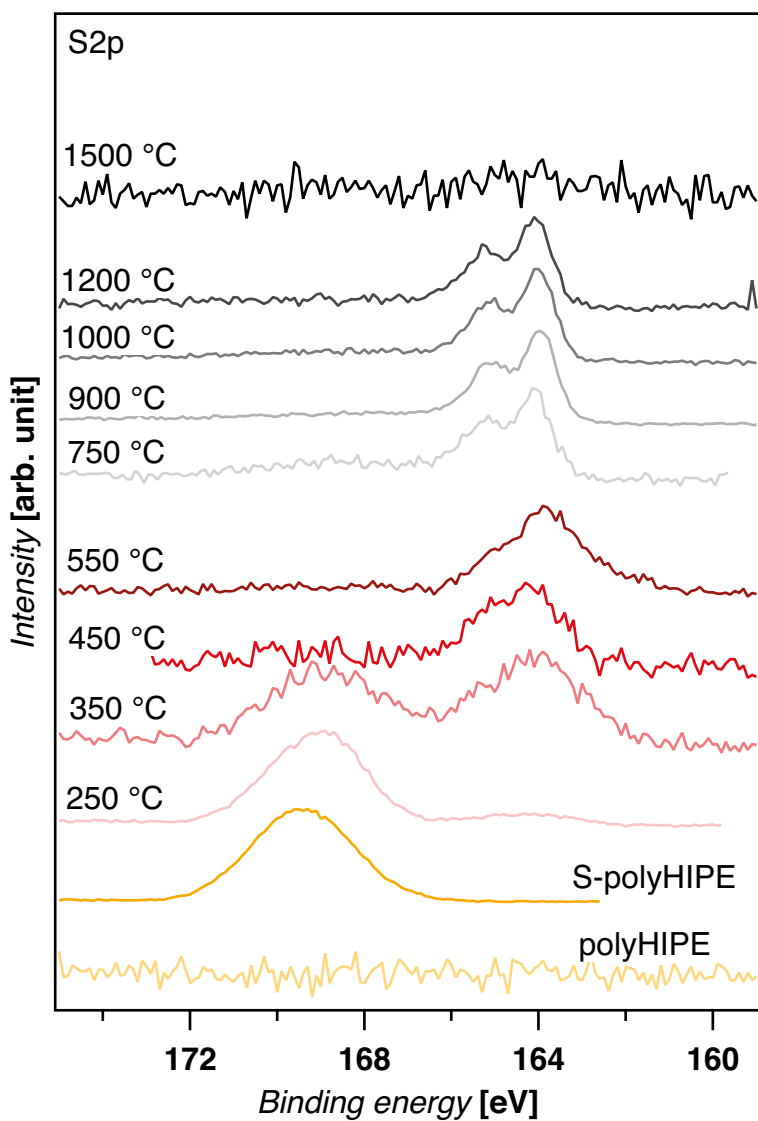


Figure 3.12. The S 2p X-ray photoelectron spectra of the pure polymer, the sulfonated polymer and the carbon foams obtained at various pyrolysis temperatures. The S 2p spectra reveal the chemical states of the sulfur species as a function of temperature.

determine the oxidation states of ions or atoms which constitute a given substance. Shown in *Figure 3.12* are the S 2p XPS spectra of the pristine polymer, the sulfonated polymer (S-polyHIPE) and several other samples obtained by heating the sulfonated polymer at different temperatures. One can see that the sulfonated polyHIPE displays a broad peak centered on a binding energy of 169.5 eV that typifies highly oxidized sulfur species [189,191]. Undoubtedly, the sulfur 2p peak seen at higher energy can be assigned to the $-\text{SO}_3\text{H}$ functionality. It can be noted that a new peak emerges as the sulfonated polymers are heated at 250 °C. The peak has shifted by 5 eV and corresponds to $-\text{C}-\text{S}-$ bond, hinting at the onset of deoxygenation of the sulfone $-\text{C}-\text{SO}_2-\text{C}-$ bonds [189,191]. In the sample heated at 350 °C, the sulfur exists in two different states, as evidenced by the peaks appearing at two different binding energies of approximately 169 and 164 eV. Both oxidized and reduced forms of sulfur are present at this stage. Further heating above 450 °C leads to the formation of predominantly $-\text{C}-\text{S}-\text{C}-$ bonds in the carbon foams. Based on XPS analyses, the sulfur persists even at temperatures as high as 1200 °C. Beyond 1500 °C, however, no detectable amount of sulfur was observed. Additional XPS data and the atomic percentage of sulfur at the surface as a function of temperature are given in *Figure S9* and *Figure S10* of the supporting document appended to Paper I. As XPS probes only few nanometers deep

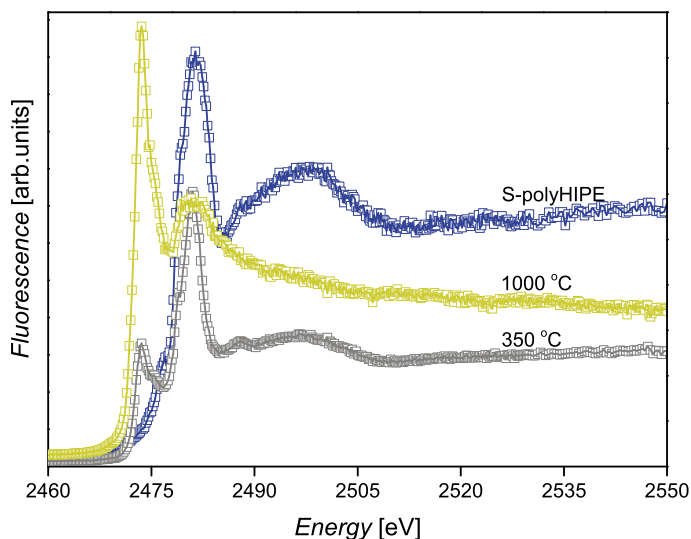


Figure 3.13. In the XANES part of the X-ray absorption spectra, the K-edge absorptions were used to determine the oxidation states of sulfur at three selected temperatures

into the surface, results discussed so far reflect only the elemental make-up of

the samples at the surface. Insight into the chemical nature of the bulk of three selected samples was obtained through X-ray absorption near edge fine structure (XANES) measurements conducted in the fluorescence yield mode. The spectra are shown in *Figure 3.13*. The sulfur species in each sample were identified by their oxidation states deduced from the 'white-lines' of the absorption S K-edges. Furthermore, the spectra of the sulfur species were compared to absorption edges of different sulfur species reported in published literature. A summary is given in *Figure 5 c)* in Paper I. Accordingly, the sulfonated polymer prior to thermal treatment contains sulfur in the form of sulfonates as indicated by the peak around 2481.4 eV. Changes in the peaks occur as the polymer was heated to 350 °C. The spectrum indicates the presence of both oxidized and reduced sulfur as evidenced by the peaks centered around 2481 eV for sulfone and 2473.6 eV for sulfide bonds. The carbon foam prepared at 1000 °C contains mainly thioether bonds with a maximum binding energy of 2473.6 eV. These results are consistent with the conclusions drawn on the basis of the XPS analyses and prove the existence of same chemical species of sulfur on the surface and in the bulk of the samples.

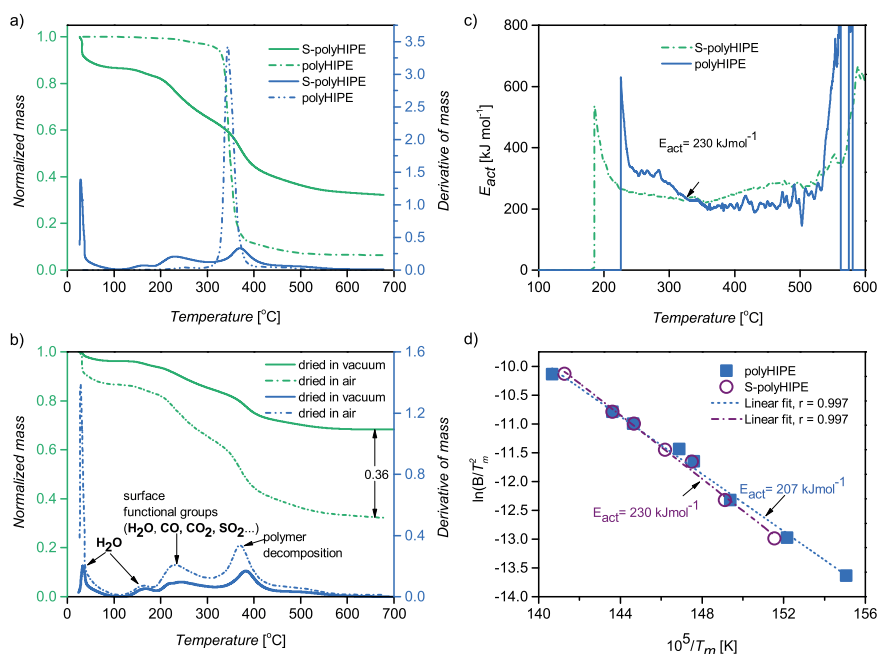


Figure 3.14. Modulated thermogravimetric analyses (MTGA) are conducted on the pristine and sulfonated polymers. a) TG curves showing the decomposition patterns of the pristine and sulfonated polymer. b) The influence of excess adsorbed water on the pyrolysis of the sulfonated polymers. c) A plot of activation energy versus temperature as determined by modulated TGA. d) Kissinger's plots of decomposition activation energies.

How do such chemical transformations affect the thermal properties of the polymers? Thermogravimetric analyses were performed on both the pristine and the sulfonated polymers to study their thermal stability and decomposition kinetics. In the case of the pure polymer, the decomposition takes place rapidly within a narrow temperature range. As shown in *Figure 3.14 a*), the TGA curve falls off sharply as opposed to that of the sulfonated polymer in which case stepwise decomposition patterns are observed. Initial mass loss can be attributed to evaporation of moisture adsorbed on the surface or entrapped in the pores of the polymer. The influence of adsorbed water on the pyrolysis of the sulfonated polymer can be seen in *Figure 3.14 b*), which displays the decomposition behaviors of the sulfonated polyHIPE before and after drying under vacuum for 24 hours. Accordingly, the carbon content increases by almost 36 % for the vacuum dried polymer. This is presumably linked to the fact that sulfonation is reversible in the presence of water, particularly at elevated temperatures [192, 193]. In brief, adsorbed water leads to the expulsion of sulfonic acids and hence compromises the thermal stability of the sulfonated polymer during pyrolysis. As the temperature increases the release of other gases such as CO, H₂O, CO₂, SO₂ *et cetera* accounts for the drop in the mass of the sample. A detailed explanation is given in the discussion of the residual gas analysis. In *Figure 3.14 c*), plots of activation energy of pyrolysis of the pristine and the sulfonated polymers are given as a function of temperature. Obviously, the plots indicate that the activation energy of decomposition is zero at the beginning as no chemical reaction occurs. As the temperature increases, the polymers start to decompose, and the activation energy for the unmodified polymer decreases whereas that of the sulfonated polymer increases. The depolymerization of the pristine polymer is favored, and thus increasingly lower activation energy is required until more or less the entire polymer is degraded. In addition, as shown in *Figure 3.14 d*) the use of Kissinger's equation [194] indicates that the decomposition of the sulfonated polymer requires higher activation energy (around 23 kJ mol⁻¹ higher) than the untreated polymer.

A summary of the residual gasses emitted as a result of the thermal decomposition of the sulfonated polymer is given in *Figure 10.1*. Initially, water is the predominant emission detected by the mass spectrometer. As the temperature increases, however, other gasses are also produced. The principal emissions up to 300 °C occur with m/z ratios of 18, 28, 44, and 64 which correspond to water, carbon monoxide, carbon dioxide and sulfur dioxide, respectively. At around 400 °C, the polymer starts to decompose giving off volatile organic molecules such as benzene (m/z 78), methylbenzene (m/z 91) and styrene (m/z 104) in addition to the gases listed above. One can also note that at temperatures above 800 °C carbon monoxide is the major gas being emitted along with dihydrogen gas and water. This indicates that the surface of the carbon has been oxidized in the course of pyrolysis, probably as a result of the deoxygenation of –SO₂– to sulfide moieties. Another important

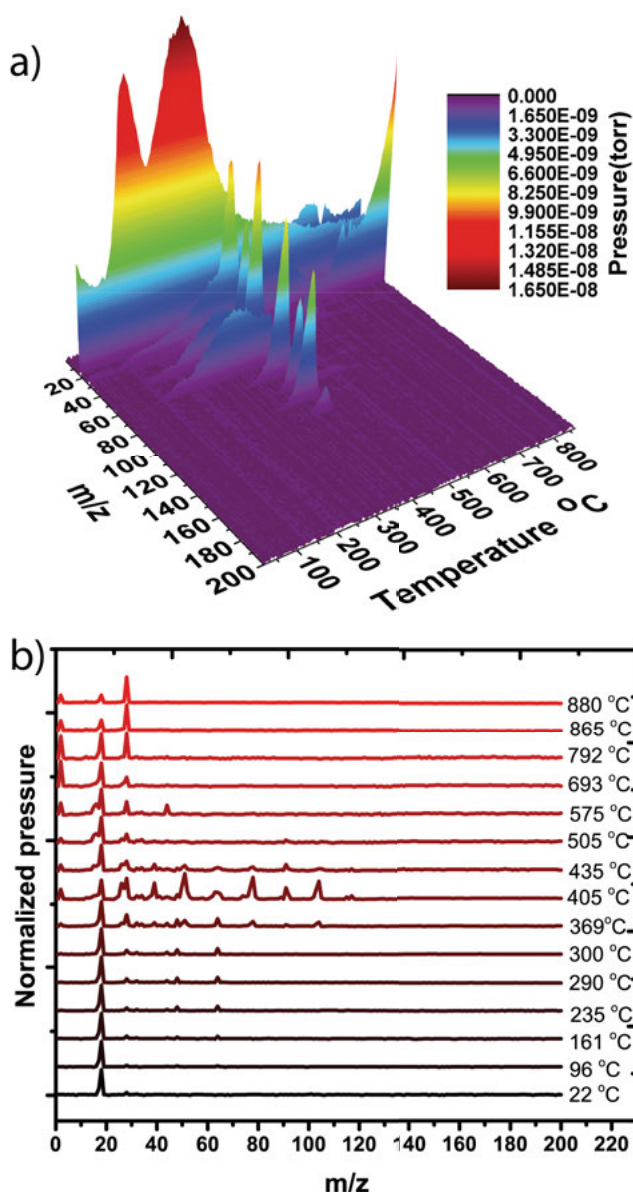


Figure 3.15. In situ residual gas analysis (pyrolysis-mass spectrometry) performed on the sulfonated polymer to identify the various gases emitted during pyrolysis. a) The 3D colour map shows the gaseous emissions identified by their mass-to charge ratios and as a function of temperature. b) A summary of the results showing the different gases given off at selected temperatures.

point is that all the sulfonic acid groups do not end up being reduced to form thioether bonds. There is competition between reduction to sulfide bonds and

desulfonation leading to the release of sulfur dioxide. However, it is evident, as discussed above, that part of the sulfonic acid groups are reduced to form —C—S—C— links unlike some literature reports purporting that desulfonation results in a complete removal of sulfur from the carbon materials during pyrolysis [125, 137, 195]. Evidently, our results argue against these claims and are in good agreement with the report by Matsuda *et al* [190].

In conclusion, the data discussed above confirm that the pendant sulfonic acid groups undergo chemical transformations to —C—S—C— crosslinks in the course of pyrolysis. The thioether (—C—S—C—) bonds reinforce the thermal stability of the polymer thereby reducing the extent of depolymerization and boosting the charring tendency of the porous polymers.

3.6 Structural evolution during pyrolysis

Another interesting feature of the XPS data is that the C 1s peaks become increasingly more well-defined with increasing pyrolysis temperature. The peaks appear to have well-separated and sharp doublets. This phenomenon may be indicative of the increased order and homogeneity in the carbon-carbon bonds as predominantly sp^2 -type carbon forms at higher temperature. The C 1s XPS spectra are provided in *Figure 5 b*) in Paper I. Studies on the

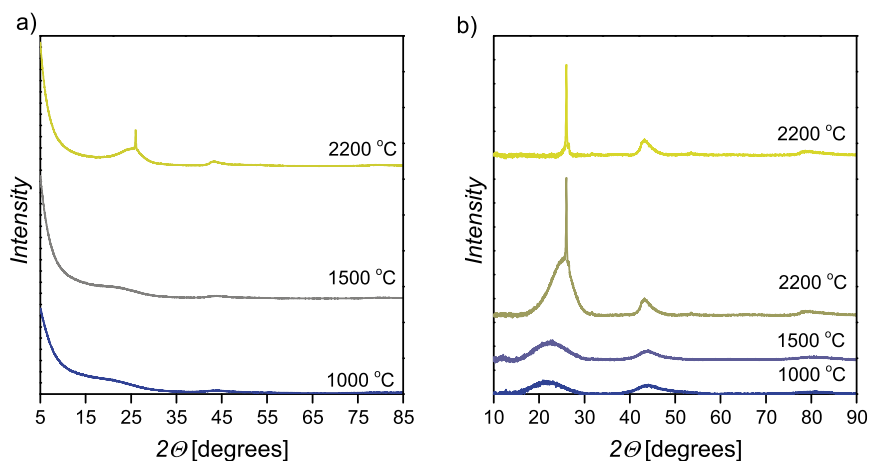


Figure 3.16. Structural changes in the carbon foams synthesized at 2000 rpm and pyrolysis temperature of 1000, 1500, and 2200 °C were investigated using powder X-ray diffraction (XRD). In the XRD patterns a) with diffuse scattering backgrounds and b) obtained after removing the diffuse scattering backgrounds show the impact of pyrolysis temperature on the ordering and size of the crystallites in each carbon foam.

microstructure of the carbon foams were conducted using X-ray diffraction, high resolution TEM and Raman spectroscopy. The X-ray diffraction patterns of the carbon foams are shown in *Figure 3.16*. After stripping the diffuse

background off by spline fitting, the XRD patterns clearly display the changes in the width and intensity of the (002) peak that is attributed to stacking of graphene layers along the c-crystallographic direction. As a matter of fact, the structure of carbon materials can be explained in terms of the stacking order of the graphene layers, and the extent and orientation of the graphitic crystallites. In Figure 3.16 b), it can be noted that the broad peak centered initially on around $2\theta = 22^\circ$ for the 1000 °C carbon foam moves to higher angles, and becomes sharper progressively with increasing pyrolysis temperature. This trend arises from the increasing stacking order of the graphene sheets and the increase in the size of the graphitic domains. Carbonization at 2200 °C results in a carbon foam characterized by much sharper and more intense (002) peak around 26° superimposed on a broader one, typical of carbon materials with significant degree of graphitization. As the polymer precursors are extensively crosslinked, one should be aware of the fact that temperature [196–198] alone cannot cause the development of graphitic crystals in the carbon foams. For instance, carbon foams prepared by Hasegawa *et al.* at 3000 °C exhibited much less graphitization level as compared to carbon foams reported in this thesis [199]. It is possible that traces of metal oxides left over from the preparation stages of the polymer and carbon foams may catalyze the graphitization process. Further studies are going on. In the Raman spectra of the samples, it

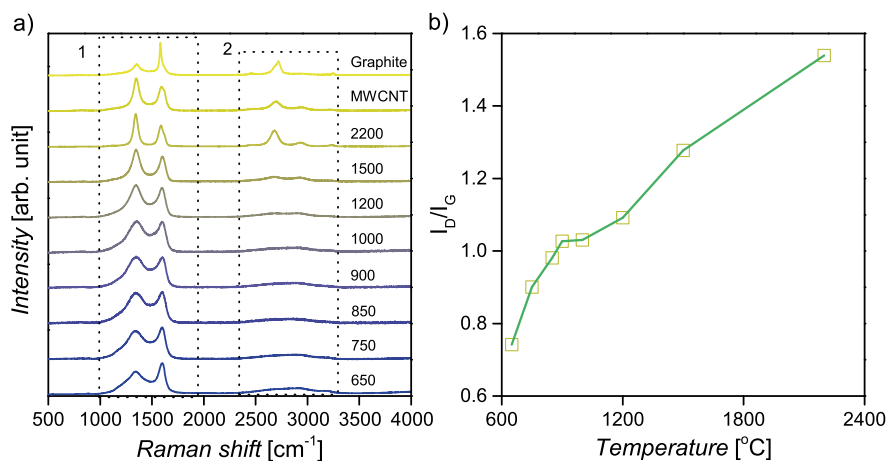


Figure 3.17. Structural changes in the carbon foams synthesized at pyrolysis temperature of 650, 750, 850, 900, 1000, 1200, 1500 and 2200 °C, along with the spectra of commercial graphite and multi-walled carbon nanotubes, were investigated using Raman spectroscopy with 532 nm laser. The structural changes linked to thermal treatments can be noted in the a) first- and second-order Raman scattering bands, which become more distinct and sharper with increasing pyrolysis temperature. In b) a plot of the ratio of the maximum intensity of the disorder band to that of the graphitic bands is given as a function of temperature for the spectra given in a).

is to be observed that the characteristic bands of carbon become increasingly

well-defined with increasing temperature. In *Figure 3.17 a)* plots of Raman spectra collected for samples prepared at different heat treatments are shown. All the spectra, especially below 1500 °C, are dominated by broad and intense bands around 1346 cm^{-1} (D-band) and 1600 cm^{-1} (G-band) which can be assigned to a breathing mode of vibration of A_{1g} symmetry of the six-membered ring and in-plane modes of vibration of E_{2g} symmetry of the conjugated sp^2 bonds, respectively [200–202]. In addition, overtones (2D and G+D, for example) can be seen in the region 2360 to 3380 cm^{-1} [200–205]. The carbon

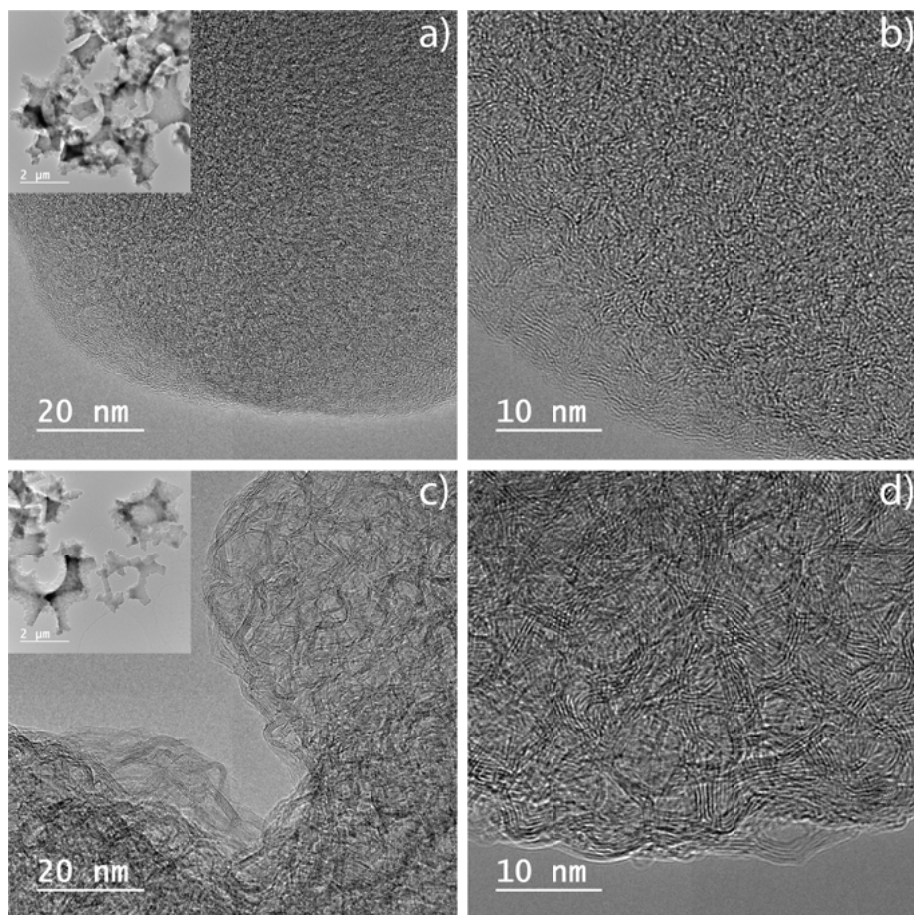


Figure 3.18. Closer inspection of the carbon foams obtained from the polyHIEPs prepared at 2000 rpm and pyrolyzed at a) and b) 1500 °C, and c) and d) at 2200 °C was conducted using high resolution electron microscopy (HRTEM). The insets in a) and c) show the morphologies of carbon foam struts used for the analysis.

foam prepared at 2200 °C exhibits sharp, well-defined Raman bands at 1342.6 and 1588 cm^{-1} . Given that the D- and G- bands are due to sp^2 scattering sites, it can be concluded that the content of sp^2 carbon is increasing progressively with increasing temperature. In an amorphous carbon, the increase in the I_D/I_G

is indicative of ordering in contrast to the case of graphite. Since the D-mode is linked to the presence of six-membered carbon rings, its intensity is proportional to the extent of graphitic clusters (L_D) as described by $I_D/I_G \sim L_D^2$. What is more, the second order Raman scattering bands are also clearly detectable for this carbon. They occur around 2451, 2677, 2932, 3236 cm^{-1} . These bands are characteristic of carbons with finite-sized graphitic crystallites and significant contributions from the edge planes [200–204]. The high resolution transmission micrographs (HRTEM) given in *Figure 3.18*, and in Paper I in *Figure 6* and *Figure S5* show clearly the continuous increase in the order of the carbon foams in good agreement with the Raman spectra. One can note the presence of turbostratically disordered graphene layers whose extent and order increases with increasing pyrolysis temperature. In the high resolution transmission electron micrographs (HRTEM), it can be seen that the carbon foams synthesized at 1000 and 1500 °C are characterized by turbostratically disordered graphene sheets as compared to the carbon foam synthesized at 2200 °C [197, 198].

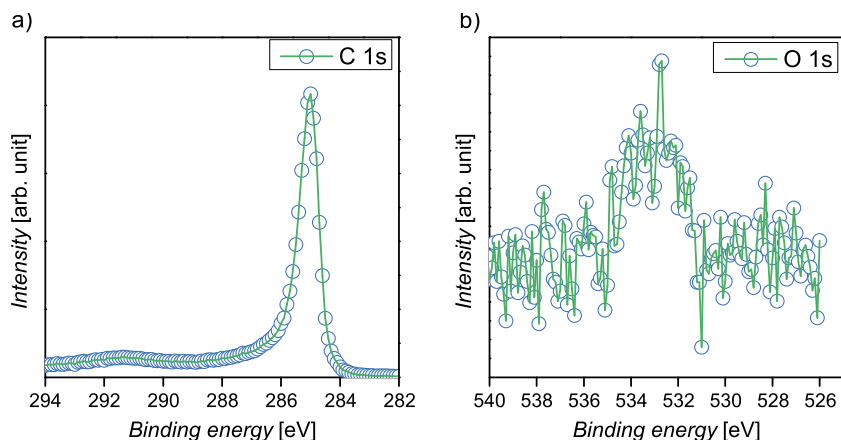


Figure 3.19. The a) C 1s and b) O 1s XPS spectra of the carbon foam synthesized at 2200 °C.

3.7 The surface of carbon foams

Surface functional groups affect the electrochemical performance of carbon materials which are commonly used as anodes in lithium-ion batteries [206–208]. Probing the surface of the carbon foams is, thus, important in order to be able to explain their electrochemical behaviors. A surface study was performed using X-ray photoelectron spectroscopy. The spectra of the carbon foams prepared at various pyrolysis temperature can be seen in *Figure 5 b)* and *Figure S9* and *S10* in Paper I, as well as *Figure S3* and *S4* in Paper II.

Accordingly, the elemental composition of surface functionalities consisting of S and O generally tend to decrease with increasing temperature. In addition, the carbon foam synthesized at 2200 °C is observed to have no detectable amount of sulfur and lower amount of oxygen. The C 1s and O 1s spectra are provided in *Figure 3.19*.

4. Lithium-ion Storage in Emulsion-templated Carbon Foams

This chapter deals with the potential use of a polyHIPE-derived carbon foam as a monolithic anode in lithium-ion microbatteries. The carbon foam is intended to serve dual purposes, namely as an active material and a 3D current collector. In conventional use, porous carbon materials are crushed to powder and cast from a slurry onto metal current collectors along with conductive additives and binders. Providing the porous carbon particles are reduced in size, usually a higher gravimetric capacity is obtained. It is of critical interest to underline the fact that the emulsion-templated carbon foam studied in this thesis can be used in the absence of a binder and a metal current collector. The impact of the pyrolysis temperature on the electrochemical behavior of the carbon foams is investigated. Particularly, the dependence of the initial irreversible loss of lithium ions on pyrolysis temperature is looked into.

4.1 Lithium-ion storage and the structure of carbon materials

Carbon materials are renowned for their structural diversity. Depending on the preparation history and precursors used, they exhibit distinctively different chemical, electrochemical, and mechanical properties. Carbon exists in various forms called allotropes, namely disordered carbon, graphite, diamond, fullerenes, nanotubes, and so on [209]. Those which consist of sp^2 carbon bonds like graphite and disordered carbon materials have long been studied in interest of their ability to store lithium ions. Particularly, graphite is widely used in commercial lithium-ion *rocking-chair* batteries due to its better safety, less reactivity and cost as compared to lithium metal. However, lithium ion intercalation into graphite limits the maximum capacity to 372 mAh g^{-1} which corresponds to LiC_6 staging. Disordered carbons obtained from the low temperature pyrolysis of organic precursors offer remarkably higher specific capacities, but with some limitations such as low density, high irreversible capacity during the first cycle, and hysteresis between charge and discharge voltage-capacity curves [206, 210]. The electrochemical formation of a passivation layer on the carbon surface, i.e., SEI layer, reaction of lithium with surface functional groups, adsorbed molecules and entrapment of lithium ions in nanopores account for the high irreversible capacity [206]. It is worth noting that the structure of disordered carbons varies considerably depending on

the type of precursor and pyrolysis temperature. Same holds good regarding their capability to store lithium ions [37]. Rosalind Franklin is credited for having proposed the classification of carbonaceous materials as (i) graphitizing, (ii) partially-graphitizing, and (iii) non-graphitizing [196]. Based on their electrochemical behaviors, Dahn *et al.* classified carbonaceous anodes as (i) graphitic or *soft*, (ii) hydrogen-containing, and (iii) non-graphitizable or *hard* carbons [37].

4.2 Emulsion-templated carbon foam anodes

4.2.1 The first discharge and pyrolysis temperature

As a rule, low-temperature, disordered carbon materials are plagued with huge irreversible capacity losses during the first discharge as a sizeable amount of lithium is consumed in passivating their large surface areas (SEI layer formation). Irreversible reaction with surface functional groups and adsorbed molecules, and entrapment of lithium in nanopores can be regarded additional sources of lithium ion sinks which contribute to the initial capacity loss. True to form, the polyHIPE-derived carbon foam prepared at 700 °C shows a footprint area capacity of 5.5 mAh cm⁻² on the first discharge; however, the amount of lithium inserted during the first discharge is not fully retrieved during charging and the subsequent cycles. See *Figure 4.1 a*). After the first cycle, the capacity tends to be more stable indicating the increase in reversibility of the lithium insertion process. Improvement in the reversibility means parasitic reactions involving the irreversible reduction of the electrolyte and the surface functional groups have abated. The coulombic efficiency computed as

$$C_{eff} = \frac{Q_{delithiation}}{Q_{lithiation}} \quad (4.1)$$

improves progressively from 31.4 % for the first cycle to 71.4, 82.7, and 85.8 % in the following second, third, and fourth cycles. In the Supplementary document appended to Paper II, XPS measurements used to explore the surfaces of the pristine and cycled carbon foams are presented in detail. Accordingly, the pristine carbon contains oxidized carbon functional groups aside from residual impurities (sulfur and calcium) left over from the preparative process of the carbon foams. Calcium impurities can be effectively avoided by repeated washing of the polymer with water and ethanol before the sulfonation step. After cycling, the XPS spectra of the carbon foam bear the characteristic features of SEI layer as identified by the peaks reminiscent of electrolyte decomposition. The spectra are shown in *Figure S4* and the relative molecular composition of the surfaces are given in *Figure S3*. Detailed discussion can be found in the supplementary information of Paper II.

Success to apply the carbon foam monolithic electrodes in practical micro-batteries is contingent upon the ability to bring the irreversibility down to as

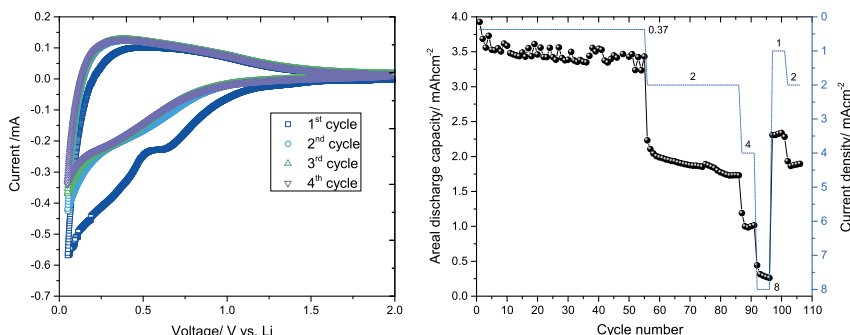


Figure 4.1. Electrochemical behavior of a monolithic carbon foam anode. (a) The first four cyclic voltammograms of the carbon foam scanned at a rate of 0.01 mV s^{-1} in the range 0.05 and 2.0 V versus Li^+/Li . The coulombic efficiency for cycles 1, 2, 3, and 4 are 31.4, 71.4, 82.7, and 85.8 % (b) A plot of the areal capacity at different current densities: 0.37 to 8 mA cm^{-2}

low a level as possible. A tried and tested strategy for ensuring acceptable electrochemical performance would entail optimizing the pore sizes, reducing the specific surface areas, and increasing the degree of graphitic ordering. With this in mind, a set of carbon foams have been prepared by carbonizing the sulfonated polyHIPE (from 2000 rpm HIPEs) at 1000, 1500 and 2200 °C. One needs to understand that the pyrolysis temperature determines the total surface area, pore sizes, morphology, chemical bonding and the structure of the carbon foams. The results obtained from CV analyses are plotted in the graphs given in *Figure 4.2*. It is clearly observed that the CVs for the three different samples are substantially different based on the features visible in the discharge-charge waves. The carbon foam resulting from pyrolysis at 2200 °C exhibits a single, distinct and sharp reduction peak around 0.72 V *Figure 4.2 c*) that is indicative of electrolyte reduction and SEI formation on the carbon surface. This reduction peak appears at a much higher potential, around 1.13 V, and is followed by more features in the CV of the 1500 °C electrode, as can be seen in *Figure 4.2 b*). Such well-defined features are not observed for the 1000 °C carbon foam electrode (*Figure 4.2 a*)). More importantly, the amount of charge wasted due to the reductive decomposition of the electrolyte (and reduction of oxygen containing surface groups) in the high temperature carbon anode appears to be much less as compared to those of the other two electrodes. To be precise, irreversible losses associated with the three electrodes synthesized at 1000, 1500, and 2200 °C are 58.4, 51.5, and 24 %, respectively. As pointed out in detail in the previous chapter, the carbon foams synthesised at a range of pyrolysis temperature differ in terms of the amount and composition of the heteratom functionalities present on their surfaces. Ample references exist in the literature in support of the fact that surface functionalities contribute to the irretrievable capacity loss observed in the course of the initial discharge

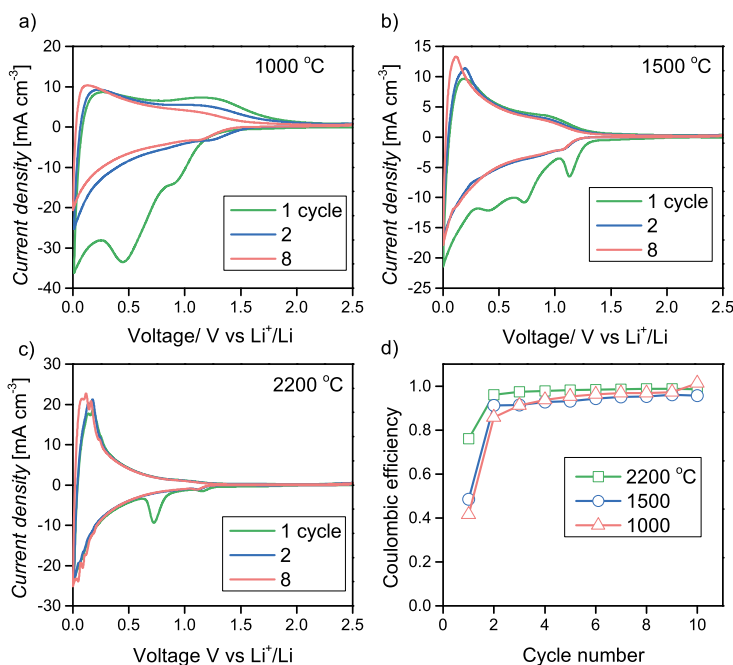


Figure 4.2. Evaluation of the electrochemical performance of each carbon foam obtained by carbonizing the sulfonated polymers prepared at 2000 rpm and at different pyrolysis temperatures. In the cyclic voltammograms (CVs) recorded at a scan rate of 0.05 mV s^{-1} for a) 1000 °C, b) 1500 °C and c) 2200 °C, it can be noted that the first discharge (lithiation) process display some features resulting from irreversible reduction of the electrolyte and surface functional groups. Over the subsequent 10 cycles the coulombic efficiency improves from 41.6, 48.5, and 76 % to 100, 95.6, and 98.6 % for the CVs given in a) to c), respectively.

reaction [206–208]. In a full-cell design, the positive electrode provides the lithium ions that are inserted into the carbon anodes during charge. Excessive loss of the lithium ions is detrimental to the cycle performance and life of the battery. Needless to say, only the 2200 °C is considered promising for successful application as a 3D anode in microbatteries.

4.2.2 Electrochemical performance

As discussed in detail in Paper II, after the cyclic voltammetry experiment galvanostatic cycling tests were conducted on the carbon foam prepared at 700°C. The rate performance of the electrode is shown in *Figure 4.1 b*). For the lowest cycling rate (a current density of 0.37 mAh cm^{-2} corresponding to roughly 0.1

C), a footprint area of 4.0 mAh cm^{-2} is obtained. It should be remembered that in this particular application the carbon foam is acting as both active material and current collector and that the entirety of the 3D geometry may not be accessible to the lithium ions in the electrolyte. Gravimetrically, this capacity amounts to 214 mAh g^{-1} as can be seen in *Figure 6 a)* of Paper II. This is in

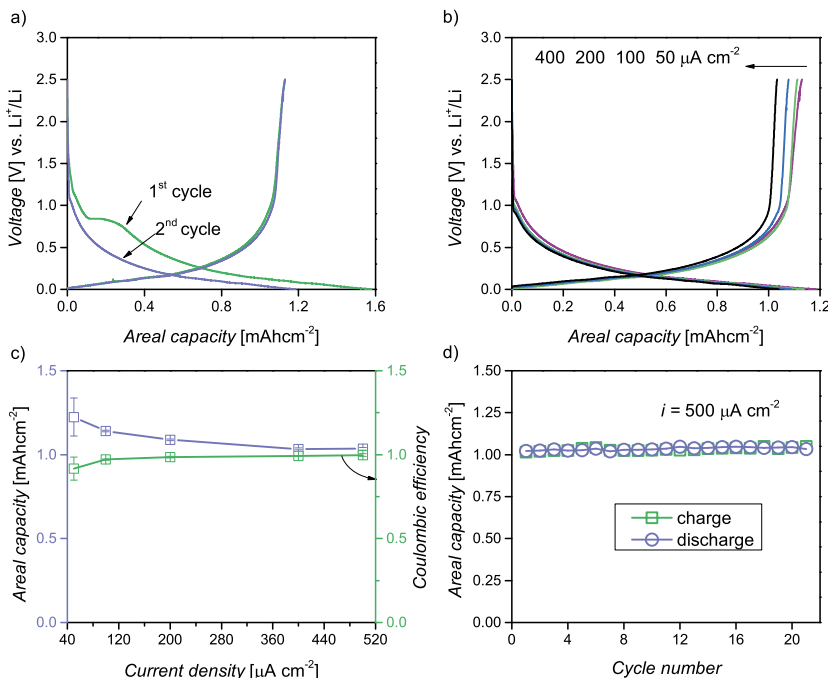


Figure 4.3. The carbon foams prepared at 2200 °C was further characterized by controlled-current cycling at various current densities. a) The first discharge displays a distinct plateau at around 0.84 V vs. Li^+/Li which can be attributed to electrolyte decomposition. b) The voltage-capacity galvanostatic curves obtained for the indicated current densities. The corresponding areal capacities are also shown in the c) capacity-current density plots along with the respective coulombic efficiency. d) The cycling behavior of the electrode is shown for over 20 cycles at a current density of $500 \mu\text{A cm}^{-2}$.

good agreement with Brun *et al.* who demonstrated that a Si(HIPE)-derived carbon foam could supply a stable capacity of 200 mAh g^{-1} for the first 50 cycles [167]. It's worth mentioning, though, that they utilized 10 % carbon additive along with a powdered sample of the carbon foam. At higher cycling rates the capacity drops drastically mainly due to the internal cell resistance as the electrical conductivity of porous and freestanding carbons are usually low [61]. On the whole, large capacity losses, and low coulombic efficiency, during the first discharge are the hallmark of carbon anodes with disordered structures and scale with increasing specific surface areas [206–208]. So, it

suffices to state that carbon foams ideally suited to microbattery applications are the ones with high degrees of graphitization and low specific surface areas. In practice, pyrolysis of the polymer foams at higher temperatures tends to diminish the specific surface areas and increase the density of the carbon foams thereby redoubling their mechanical stiffness as a result. In addition to cyclic voltammetry (CV), galvanostatic or controlled-current methods have been used to study the performance of the carbon foam electrodes.

In *Figure 4.3*, the voltage-capacity curves associated with the first and second cycles are recorded at a current density of $50 \mu\text{A cm}^{-2}$. As can be seen in the initial discharge curve, a distinct plateau appears around 0.84 V vs. Li^+/Li that is characteristic of electrolyte decomposition, and the formation of the SEI layer, which is true of graphitic carbon anodes with pristine surface. The influence of increasing current density on the areal capacity can be observed in *Figure 4.3 c)*. High areal capacities of 1.22 and $1.03 \text{ mA h cm}^{-2}$ are obtained when the carbon foams were cycled at 50 and $500 \mu\text{A cm}^{-2}$. Accordingly, despite the 10-fold increase in the current density, approximately 85 % of the low rate capacity is accessible which in turn hints at the suitability of the materials for high power applications. The good cyclability of the electrode can also be seen in the capacity-cycle number plot provided in *Figure 4.3 d)* for over 20 cycles. However, further investigation is needed to study the power performance of the carbon foam in the future.

5. Emulsion-templated Carbon Foams as 3D Substrates

This chapter is based on the results reported in Paper II and IV, and discusses the potential use of carbon foams as substrates for active materials that can be deposited via electrodeposition and sol-gel processing. As described in the preceding sections, polyHIPE-templated carbon foams are of immense interest due in large part to their high specific surface areas and well-networked structures. To prove their applicability in electrodeposition of battery materials, a layer of polyaniline (PANI) was electrodeposited on the carbon foams and used as a cathode versus lithium. The synthesis of LiFePO_4 on the carbon foams by means of a sol-gel approach, and the electrochemical performance of the composite electrode as a cathode for 3D microbatteries have been accomplished.

5.1 PANI-coated carbon foams for 3D lithium microbatteries

Polyaniline (PANI) is a classic example of polymers which are rendered conductive by appropriate oxidation or doping [211]. Ideally speaking, polyaniline exists in one of the three chemical forms which have different colors and electrical properties: (a) leucoemeraldine: colorless and insulating, (b) emeraldine: green/blue and highly conducting in its salt form, and (c) pernigraniline: blue/violet and weakly conducting [211]. In its fully reduced state polyaniline is known as leucoemeraldine. The fully oxidized form is termed pernigraniline. Both leucoemeraldine and pernigraniline are poor conductors. The emeraldine base, which is a combination of benzoid and quinoid structures, is the most useful form of polyaniline. Doping of emeraldine base gives rise to a highly conducting form of polyaniline, emeraldine salt.

5.1.1 Electrodeposition of PANI

Polyaniline is commonly synthesized by oxidative polymerization of aniline either chemically using ammonium peroxydisulfate as oxidant, for example, or electrochemically. Cyclic voltammetry (CV) is the major electrochemical technique employed to prepare polyaniline from a wide selection of deposition baths, both aqueous and non-aqueous [212–215]. In *Figure 5.1* are shown

the cyclic voltammograms for PANI deposition on several substrates. Accordingly, the CV for the electropolymerization of aniline, as indicated in Figure 7a, shows two sets of prominent peaks on anodic and cathodic sweeps. The first peak is associated with the oxidation of leucoemeraldine state of polyaniline and is believed to occur without the participation of protons; it involves the release of electrons and formation of quinoid rings. The position of the second peak has been found to vary with the pH and is assigned to the oxidation of emeraldine to pernigraniline state of polyaniline. Removal of one mole of electrons is accompanied by the release of four moles of protons which leads to the formation of additional quinoid ring [216]. There is also a pair of small peaks which have been linked to intermediates formed during the electropolymerization [212,217]. In Paper II, polyaniline was electrodeposited by

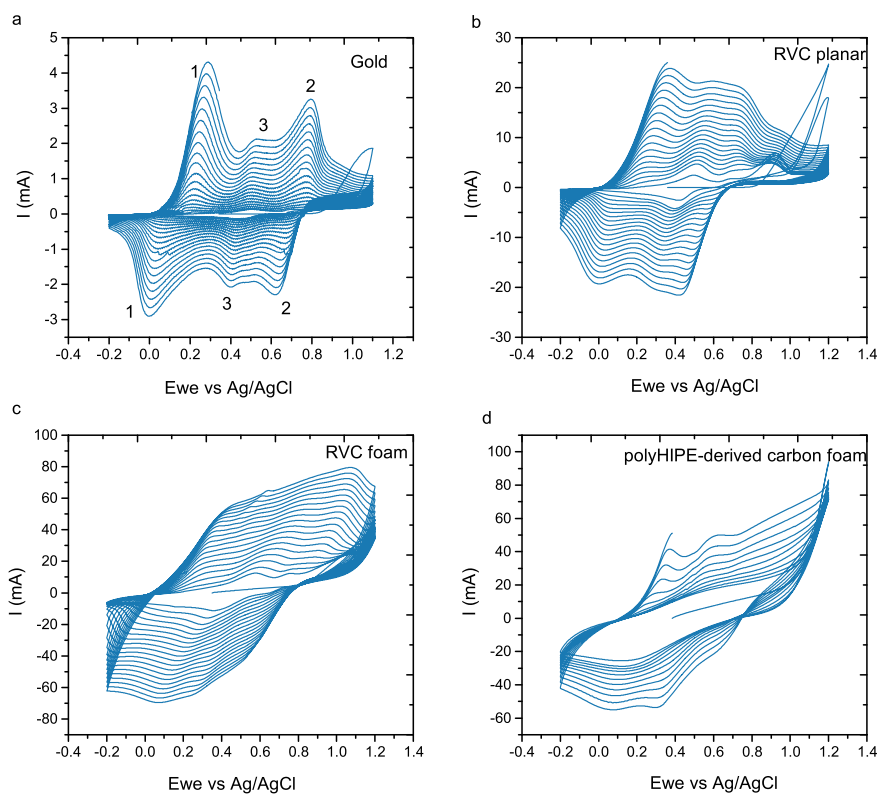


Figure 5.1. Cyclic voltammograms of polyaniline deposition from aqueous solution of 0.1M aniline in 0.25 M H_2SO_4 on different substrates: (a) planar gold (b) planar reticulated vitreous carbon (RVC) (c) 100 ppi RVC foam and (d) polyHIPE-derived carbon foam. In all cases, a scan rate of 100 mV s^{-1} was used.

CV on 1 mm thick 100 ppi compressed RVC and polyHIPE-derived carbon foams from an aqueous solution of 0.1 M aniline and 0.25 M H₂SO₄ using multiple cycling at a sweep rate of 100 mV s⁻¹ in the potential range -0.2 to 1.2 V vs. Ag/AgCl. This was done in a standard three-electrode setup with a stainless steel plate counter electrode using an SP240 Biologic potentiostat. After deposition, excess sulfuric acid was carefully rinsed off with distilled water and the PANI coatings on the substrates were dried in air.

5.1.2 PANI in lithium batteries

Because of its metal-like conductivity (~ 1 to 18.8 S cm^{-1}), good redox reversibility, light weight, stability, chemical properties and low cost, polyaniline has a tremendous potential for applications in electronics and energy storage devices [218]. MacDiarmid and coworkers presented a detailed report on a rechargeable battery constructed from emeraldine base form of polyaniline as cathode and lithium metal as anode [216]. According to their work, polyaniline could supply a capacity of circa 147.7 mAh g^{-1} and energy density of 340 Wh kg^{-1} with a coulombic efficiency greater than 98 %. In the same report, it was demonstrated that the mechanism responsible for the electrochemical performance of PANI is the reversible anion doping and dedoping. According to Macdiarmid and coworkers the charge and discharge reactions of emeraldine base form of polyaniline can be designated by the following equation:

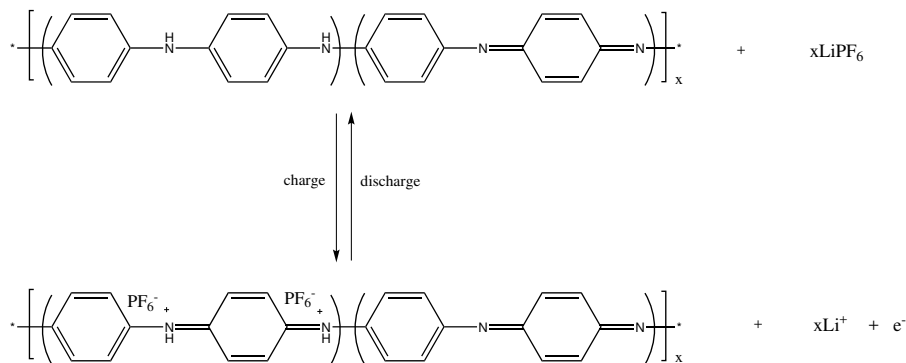


Figure 5.2. Anion doping-dedoping is the underlying mechanism of energy storage in the electrochemical cycling of PANI versus Li.

The electrochemical characteristics of the different forms of polyaniline, i.e., emeraldine base, emeraldine salt and leucoemeraldine versus lithium have been studied, as well [219]. The results borne out that emeraldine base had higher capacity and better charge recovery, 95 % as compared to the other chemical states of PANI. Various dopants such as LiClO₄, LiPF₆, LiBF₄ and polymer electrolytes have been used with polyaniline and its derivatives. Manuel et al., evaluated the performance of polyaniline doped with LiPF₆ and LiClO₄

in a 1:1 mixture of EC/DMC versus lithium and found out that LiPF_6 -doped PANI delivered higher capacity (125 mAh g^{-1}) and coulombic efficiency [219].

5.1.3 Electrochemical study on PANI-coated carbon foams

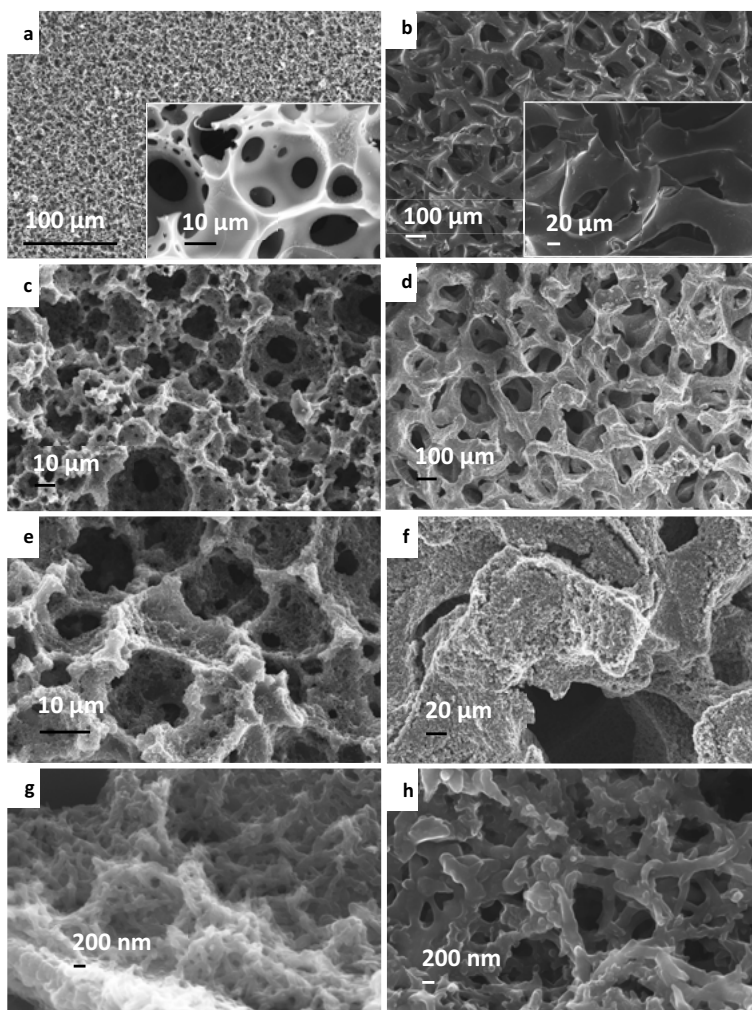


Figure 5.3. Scanning electron micrographs of bare and PANI-coated polyHIPE-derived carbon (bare: a and inset, coated: c, e and g) and RVC (bare: b and inset, coated: d, f and h) foams taken at different magnifications. For each substrate 10 cycles of deposition were performed using cyclic voltammetry. Note: Each micrograph in the second and third rows represents same image as the one directly above it but is taken at a higher magnification.

In Paper II, the polyHIPE-derived carbon foams, synthesised at 700 °C, and some commercial RVC substrates (for comparison) were coated in layers of polyaniline as described in the experimental section. The SEM images of the bare and coated carbon foams can be seen in *Figure 5.3*. The PANI coating on the RVC and polyHIPE-derived carbon surface is clearly seen as a porous layer of entangled fibers as compared to the smooth surface of the bare substrates. In both cases the deposits look to be reasonably conformal. SEM images of the cross-section of these structures were also taken and PANI deposits were observed throughout with some thinning towards the center as shown in *Figure S6* in the supportive information of Paper II.

Infrared and electron dispersive X-ray spectroscopy (EDX) analyses were carried out on the polyHIPE-derived carbon foams so as to confirm the presence of polyaniline. The EDX measurement (*Figure S2* of Paper II) clearly shows the presence of the polyaniline coating as nitrogen is detected. Carbon from both the polymer and the carbon foam is detected along with sulfur which is partly due to the sulfate dopant introduced during the electropolymerization and some remnants of the sulfonation treatment performed in the course of preparing the carbon foam. The IR spectrum is presented in *Figure 8* in Paper II and displays the most prominent absorption bands corresponding to aromatic and quinoid rings. A detailed assignment of the peaks can be found elsewhere [220]. The characteristic absorption bands of PANI salt appear at wavenumbers 1574, 1488, 1301, 1246, 1121, 804 and 702 cm^{-1} . The bands at 1574 and 1488 cm^{-1} pertain to C-N stretching of quinoid and benzenoid rings, respectively. The peak around 1301 cm^{-1} can be assigned to C-N stretching of secondary amine. The other peaks located around 1246 and 1121 cm^{-1} are due to C-N stretching in BBB unit and C-H in-plane deformation in $\text{Q}=\text{NH}^+-\text{B}$ or $\text{B}-\text{NH}^+-\text{B}$ unit, respectively (B: benzenoid ring, Q: quinoid ring). Around 804 cm^{-1} appears a slightly weaker band which is due to C-H out-of-plane deformation in the benzenoid and quinoid rings.

The electrochemical performance of the PANI-coated carbon foams was evaluated at current densities by means of controlled-current technique. The discharge curves recorded at a current density of 133 $\mu\text{A cm}^{-2}$ shown in *Figure 5.4*. The discharge occurs with a linearly decreasing voltage profile between 4 and 2.5 V vs. Li^+/Li and the majority of the capacity can still be accessed above 2.8 V. A sharp drop in discharge capacity is seen at higher cycling rates (particularly above 2 C rate) possibly due to the electrical resistivity of the carbon foam. The electrochemical cycling of PANI-coated polyHIPE carbon foams in the voltage range 2.5 to 4.0 V versus Li^+/Li proceeds with high coulombic efficiency reaching in excess of 99 % and a small hysteresis of 0.15 V (*Figure 5.4*). As shown in *Figure 5.5* the capacity is well maintained until rates above 2 C are applied; however, almost 50 % of the slow rate capacity is achieved at 5 C which is competitive with other materials reported in the literature [59, 221]. The decrease in capacity at higher cycling rates may be attributed to resistive losses as porous carbons are generally not known to

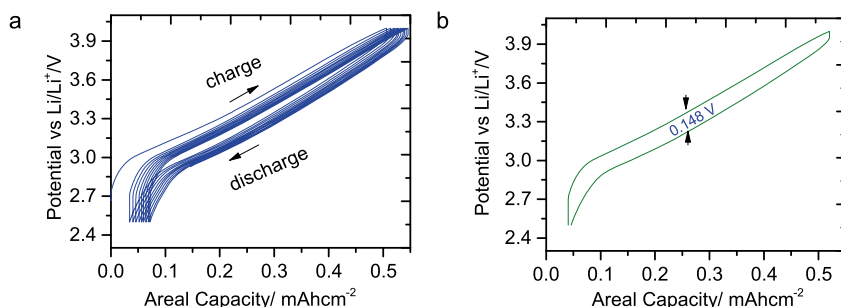


Figure 5.4. Electrochemical behavior of PANI-coated polyHIPEC foam versus lithium was examined with the help of controlled-current techniques. a) The voltage profiles obtained when a current density of 133 $\mu\text{A cm}^{-2}$ is applied. b) A voltage-capacity profile displaying the hysteresis between the charge and discharge curves.

be sufficiently good electrical conductors. It should be noted that much less areal capacity is obtained for the RVC substrate, presumably due to its lower specific surface area.

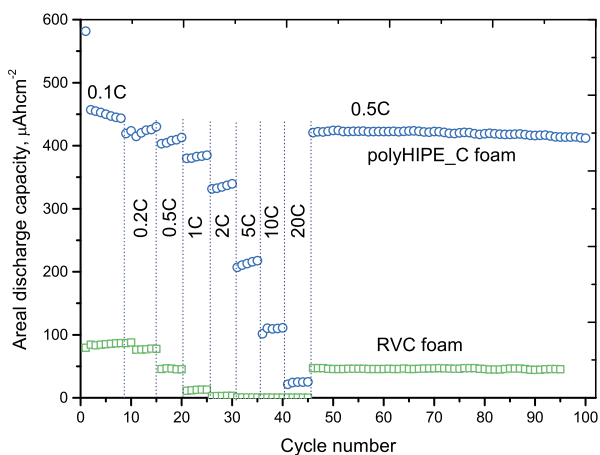


Figure 5.5. Electrochemical behavior of PANI-coated polyHIPEC foam versus lithium was examined by means of controlled-current techniques. A comparison of the rate performances of PANI-coated polyHIPEC and RVC foams are shown for several C-rates.

5.2 LiFePO₄-coated carbon foam as a positive electrode

This section deals with the synthesis of LiFePO₄ coated carbon foams and their use as monolithic cathodes in 3D microbatteries. A variety of tech-

niques are used to characterize these electrodes prior to electrochemical testing. In general, LiFePO_4 is synthesized in the carbon foams by sol-gel assisted method in which the carbon foams are dip-coated with the precursor solution. The procedure of the synthesis is described in detail in the experimental part of Paper IV.

5.2.1 Sol-gel synthesis of LiFePO_4

As a topical cathode material, LiFePO_4 has attracted a great deal of attention since the seminal work of Padhi *et al.* [20]. One of the most common preparative routes to nano-sized LiFePO_4 is sol-gel method. The synthesis approach requires the use of chelating ligands such as citric acid not only to prevent the oxidation of ferrous ions but also to generate carbon residues as the ligand undergoes pyrolysis upon heating. The carbon residues improve the electrical conductivity of the particles and create porosity desirable for electrolyte percolation [222, 223]. In addition, sol-gel synthesis of LiFePO_4 produces nanoparticles with more or less controlled size distributions. In Paper IV, thin pieces of as-prepared polyHIPE-derived carbon foams were immersed in a sol-gel precursor of LiFePO_4 . This consisted of 0.2 M $\text{FeSO}_4 \cdot 7\text{H}_2\text{O}$, 0.2 M $\text{NH}_4\text{H}_2\text{PO}_4$, 0.4 M citric acid, and 0.2 M lithium acetate in a 9:1 mixture of distilled water and methanol. The solution containing the carbon foams was evacuated in a vacuum chamber to drive out air from and to force the solution into the interior of the carbon foams. Part of the solvent was evaporated at 70 °C for 12 h leading to thicker gel due to self-condensation of citric acid. The carbon foams were taken out of the thick gel and dried at 70 °C overnight. Then they were dried under vacuum at 120 °C. The dried carbon foams were heated in a tube furnace up to 700 °C at a rate of 1 °C min⁻¹ in Ar atmosphere for 8 h.

5.2.2 Characterization

It is of primary importance to make sure that the bicontinuous structure of the carbon foam remains intact after synthesis, with no blocking of the open-celled voids. Such evidence comes from electron microscopy techniques. In Figure 5.6 (and Figure 3-5 and Figure S1 of Paper IV) SEM, TEM and STEM (HAADF-TEM) images are given. From the SEM images (using secondary electrons) it is evident that the carbon foams have been successfully coated with a layer of the active material without blocking the voids. Based on TEM images given in Figure 5.6 and Figure 4 in Paper IV, the LiFePO_4 particles are embedded in or surrounded by a porous carbon layer (< 200 nm) which is deposited on the carbon foam. Since they are heavier than the carbon particles and thus scatter electrons more strongly, they appear in the STEM (dark field) images, Figure 5.6 f), brighter than the surrounding carbon. In addition,

high resolution TEM indicates that these particles are highly crystalline as evidenced by the lattice fringes as shown in *Figure 5.6 e*). XRD pattern shown in *Figure 2 b*) of Paper IV confirms that LiFePO_4 has been synthesized in the desired crystal structure. Providing that LiFePO_4 is a complete insulator, the

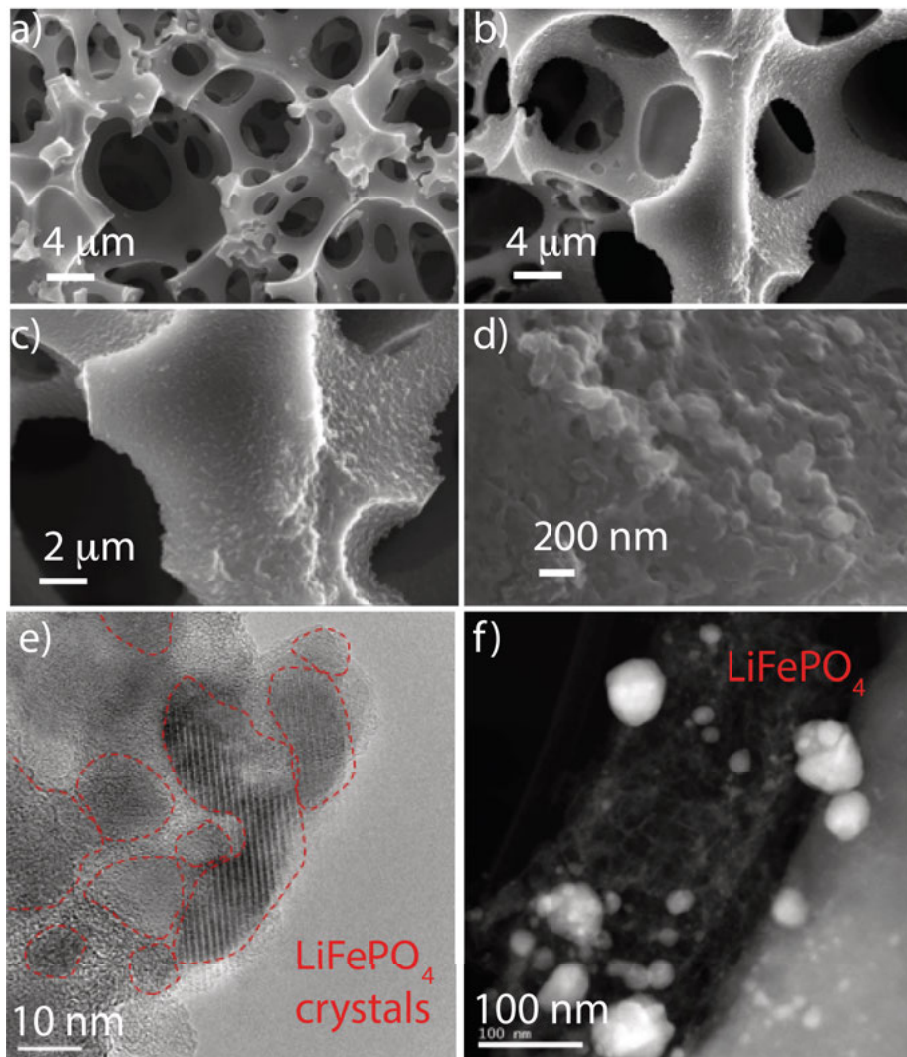


Figure 5.6. Electron micrographs show the distribution of LiFePO_4 and topography of the 3D electrodes. (a) The SEM of uncoated carbon foam, (b) to (d) The SEM of the coated carbon foams taken at different magnifications, (e) and (f) are the bright field TEM and STEM (dark field) images of the coated carbon foams, respectively, and show that crystalline LiFePO_4 particles are distributed throughout the carbon foam.

possibility of nano-sizing and carbon coating will allow for high rate cycling of the active materials. In the supplementary information of Paper IV (*Figure*

S2), the size distribution of the nanoparticles, which is evaluated on the basis of electron microscopy, indicates the majority of them are below 70 nm. Needless to say, nanoparticles are preferred for battery use as they provide shorter path length for the solid-state diffusion of the lithium ions [224].

$$\tau_D \approx \frac{L^2}{2D} \quad (5.1)$$

The above relation applies to one-dimensional diffusion processes. The variables τ_D , L and D stand for the time constant required for the diffusing species to complete a distance of L at a diffusion coefficient of D . Porosity is believed to be, as explained by Dominko *et al.*, essential for the electrolyte to permeate the vicinities of the active materials and thus facilitate the movement of ions during battery operation [222].

5.2.3 Electrochemical investigation

Next, the electrochemical behavior of the LiFePO_4 -coated carbon foam is studied using cyclic voltammetry and controlled-current techniques. Pouch cells were assembled using a piece of carbon foam (footprint areas ranging from 0.12 to 0.20 cm^2 , 400 μm in thickness) as the working electrode, a lithium foil as the counter and the reference electrode and a separator soaked in electrolyte. The gravimetric loading of the active materials is 37% of the total weight. The overall cycling and rate performance of the electrodes are shown in *Figure 5.7*. The contribution of the carbon foam substrate to the total charge and the stability of the electrolyte in contact with the carbon surface has been studied using XPS. Detailed explanation is deferred to the supporting information of Paper **IV**. Clearly, the electrode performs remarkably well at all rates in terms of both areal capacity (as shown in *Figure 5.7*) and coulombic efficiency. The latter exceeds 99.5 % and almost 60 % of the slow rate capacity (1.72 mA h cm^{-2}) is accessible at a current density 60 times higher. The gravimetric capacity at 0.2 mAh cm^{-2} (≈ 0.1 C-rate) is calculated to be approximately 157 mAh g^{-1} which corresponds to 92 % of the theoretical capacity of LiFePO_4 . *Table S1* in the supplementary information of Paper **IV** presents a summary of literature reports on different electrode materials suggested for use in microbatteries. In comparison, the performance of LiFePO_4 -coated carbon foam compares reasonably well with those of the electrodes for which the highest footprint area capacities are reported in the literature. Be that as it may, the capacity falls continuously as the rate of cycling is increased. This can be associated with ohmic losses (due to internal resistance of the cell), diffusion-limitation in the solid active materials and uneven current density distributions (inhomogeneous reaction rates) across the carbon foam electrodes. In general, the potential difference across a cell can be expressed in terms of (i) the open circuit or equilibrium potential, V_{OCV} (ii) the surface (activation) overpotential, η_a (iii) the concentration overpotential, η_c and (iv) the ohmic potential

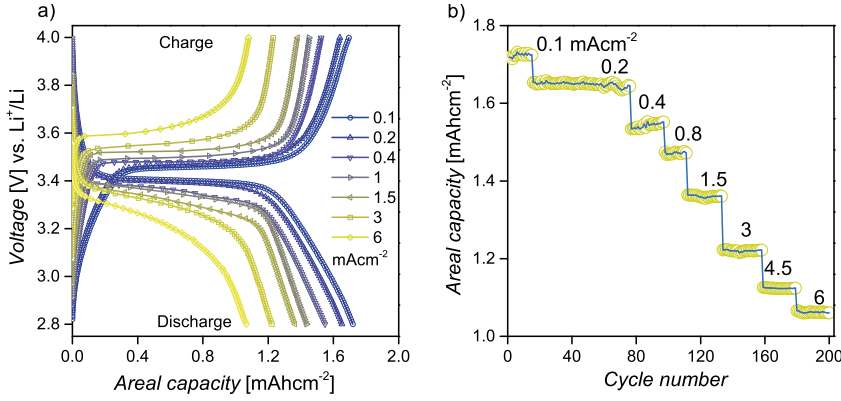


Figure 5.7. Galvanostatic cycling at different current densities (a) The charge/discharge voltage profiles of LiFePO₄-carbon foam are shown for the voltage range from 2.8 to 4.0 V vs. Li (b) areal discharge capacities are given for several current densities.

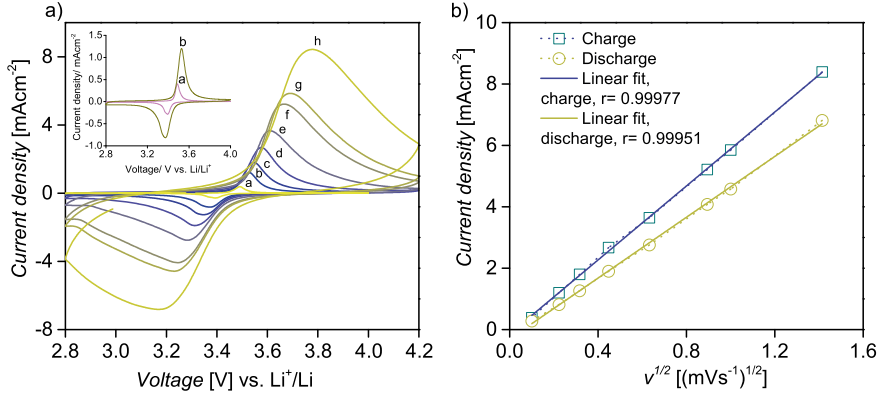


Figure 5.8. Diffusion limitation can account partly for the decrease of capacity at high rates. (a) Cyclic voltammograms of LiFePO₄-coated carbon foam at different scan rates. The CVs labeled as a, b, c, d, e, f, g, and h correspond, respectively, to scan rates of 0.01, 0.05, 0.1, 0.2, 0.4, 0.8, 1, and 2 mV s⁻¹ (b) Linear dependence of peak current densities (absolute values) on the square root values of the scan rates indicate that insertion or deinsertion of lithium ions in LiFePO₄ particles is diffusion-controlled. The symbol r stands for the correlation coefficient of linearity.

drop, IR_{ohmic} . [48] as discussed in Section 1.2 of this thesis. In Paper IV (Figures 7c and S6), a detailed explanation is provided regarding the dependence of the peak current densities on the potential of the working electrode. For the scan rates used in the CV experiment (Figure 32 (a)), the peak currents tend to follow the relation

$$\Delta E_p = I_p R \quad (5.2)$$

which indicates that resistive losses are more dominant than kinetic limitations. See *Figure 7(c)* in Paper IV. It is customary to enlarge the working voltage window to recover the capacity lost due to IR drop; however, still less capacity is obtained at higher rates even if the voltage window has been extended by 200 mV (*Figure 7(d)* in Paper IV) which more than compensates for the ohmic drop deduced from the galvanostatic curves (see *Figure S7* in the supporting information of Paper IV). This may suggest that factors other than IR drop are implicated in the high rate capacity losses. In the presence of mass transfer effects, the peak current, I_p , is supposed to follow a linear dependence on the square-root of the scan rate, v , as discussed in Section 10.8.1 and expressed by the Randles-Sevcik equation.

$$I_p = (2.69 \times 10^5) n^{3/2} A D_o^{1/2} [C_o]^b v^{1/2} \quad (5.3)$$

The plots of charge and discharge peak current densities against the square roots of scan rates are shown in *Figure 5.8 b)*. Accordingly, the peak current densities of the voltammograms vary linearly with the square root of scan rate. This behavior has been widely reported in other similar works and suggests that the electrochemical activity of LiFePO_4 is diffusion-controlled [225–227]. This is partly responsible for the incomplete utilization of the active materials at high rates. As explained in Paper IV, the solid-state diffusion coefficient of lithium ions in the active materials is dependent on the state of charge (SOC), defect concentration, particle size and so on. The diffusion coefficient that is commonly reported in the literature ranges from 10^{-12} to $10^{-14} \text{ cm}^2 \text{ s}^{-1}$ [226–229]. Assuming an average particle size of 40 nm, and using the equation provided in Section 5.2.2, the time constant for a complete charge and discharge is of the order of

$$\tau_D \approx \frac{L^2}{2D} = 10 \text{ to } 10^3 \text{ s}$$

It is worth bearing in mind that the diffusion of lithium ions will take longer times in particles bigger than 40 nm. At higher cycling rates, the diffusion of the ions in the active materials may not be sufficient to support the applied current. Notably at 6 mA cm^{-2} , the discharge process lasts for 11 minutes and only 64 % of the lowest rate capacity is obtained. Additionally, inhomogeneous reaction rates (current distributions) through the depth of the porous electrode, which are common in porous electrodes, can also be responsible for aggravating the capacity loss observed at high rates of cycling. Such inhomogeneous current densities can result in an uneven rate of consumption of lithium ions in the pore electrolyte [63]. In some regions where the reaction rate is higher, the discharge of the FePO_4 particles can end prematurely due to the depletion of the lithium ions in the electrolyte at a rate that cannot be replenished by diffusion [230]. It is relevant to mention that Strobridge *et al*

reported in a recently published work similar behavior for the electrochemical reaction of LiFePO_4 through porous electrodes [231]. To sum up, it is rather complicated to pinpoint the origin of the capacity loss in porous electrodes as it is difficult to straightforwardly separate the factors mentioned above: ohmic drop, mass transport processes in the solid active materials and in the pore electrolyte, and inhomogeneous current distributions.

6. Synthesis of Mixed-Valence Niobium and Molybdenum Oxides Through Carbothermal Reduction in Emulsion-templated Carbon Foams

Oxides of niobium and molybdenum have long attracted attention as active materials in lithium batteries and pseudocapacitors [232–234]. Both molybdenum and niobium are characterized by multiple oxidation states, and hence their oxides are of particular interest to electrochemical energy storage. A variety of approaches exist for their synthesis. Sol-gel processing of the oxides is well-established and commonly used to prepare nanoparticles of MoO_3 and Nb_2O_5 from the respective alkoxides or chloride salts [232, 234, 235]. Carbothermal reduction of these oxides has been employed to synthesize MoO_2 and NbO_2 [233, 236]. This chapter explores the use of emulsion-templated carbon foams as monolithic reactors for synthesizing transition metal oxides consisting of mixed-valence cations. Initially, amorphous oxides MoO_3 and Nb_2O_5 are produced inside the carbon foams through the hydrolysis of MoCl_5 and NbCl_5 in a mixture of ethanol and water. Carbothermal reduction allows for the synthesis of nanoparticles embedded in the porous structures of the carbon foams. The resulting composite electrodes have been investigated as monolithic electrodes for 3D microbattery applications.

6.1 Sol-gel synthesis of niobium and molybdenum oxides on carbon foams

Porous carbon materials like carbon foams can be attractive candidates as three-dimensional substrates for transition metal oxides. A variety of approaches have been used to achieve the deposition of oxide active materials on carbon foam substrates. Solution-based approaches like electrodeposition and sol-gel synthesis are particularly efficient to prepare conformal coatings or distributions of the oxides throughout the carbon substrates. A sol-gel synthesis approach was adopted to coat the bespoke carbon foams in niobium oxide nanoparticles. First, a stock solution was prepared by dissolving NbCl_5 (23 g, Aldrich[®], 99 %) in absolute ethanol making up to a total volume of 25 mL. To prepare the sol-gel precursor solution, 2.5 mL of the stock solution, 5 mL of ethanol and 0.2 g of PEO ($M_n=10,000$, Aldrich[®]) were mixed while heating

at 60 °C. The clear solution was cooled to room temperature and then 1 mL of distilled water was added under constant stirring. Pieces of the carbon foams were immersed in the precursor solution for 48 hours at room temperature. Afterwards, they were taken out of the solution and dried at 70 °C for 24 h. The coated carbon foams were then heated at 390 °C in air for 1 h in order to form amorphous Nb₂O₅. The oxide was then crystallized and partially reduced by heating it at 1100 °C in Ar atmosphere for 1 h. For the synthesis of the active material Mo₃Nb₂O₁₁ the following procedure was employed. The precursor materials were purchased from AlfaAesar and used as received. In a typical synthesis, 0.82 g of MoCl₅ and 0.54 g of NbCl₅ were dissolved in 12 mL of absolute ethanol and the deep blue solution was kept stirring for an 1 hour at room temperature. Then, 1 mL of distilled water was added to initiate hydrolysis of the salts, formation of sols. The dark-green sol solution was stirred for 30 minutes. A portion of the solution was added onto thin pieces of the carbon foams kept in a glass vial and left to soak for 48 hours. Afterwards, the carbon foams bearing the sol-gel precursor solution were taken out and allowed to age and dry at 90 °C in air for two days. Complete oxidation and evaporation of water was carried out by heating the coated carbon foams at 300 °C in air for 2 hours. Subsequently, the materials were put in a horizontal tube furnace and heated at first 600 °C for 5 hours and then at 750 °C for 2 hours in argon atmosphere. A continuous flow of gas (100 cm³ min⁻¹) and a heating rate of 5°C min⁻¹ were applied. The treatment at elevated temperature was meant to reduce Mo^{VI} to Mo^{IV} and crystallize the resulting oxide nanoparticles inside the porous structure of the carbon foams.

6.2 Structural investigation: over-stoichiometric NbO₂

Characterizations using electron microscopy, X-ray diffraction and Raman spectroscopy were conducted on the composites in order to determine the microstructures of the 3D electrodes and identify the crystal structure of the oxide particles. The scanning electron micrographs shown in *Figure 6.1* display the cellular morphologies of the carbon foams supporting the niobium oxide particles that are distributed throughout the substrate. It is crucial for the particles to maintain intimate electrical contact with the carbon foam. The particles are clearly visible in the SEM obtained by collecting the back-scattered electron, which scatter strongly and elastically from the high atomic number elements. On the basis of the HRTEM, the SAED pattern, XRD, and Raman spectra provided in *Figure 6.1* and *6.2* the synthesized oxide has tetragonal NbO₂ structure, which belongs to the space group I41/a (88) [237]. However, the X-ray photoelectron spectrum (XPS) as provided in *Figure 6.2* reveal the existence of mixed valence. Since XPS can delve into only few nanometers below the surface, the surface composition is predominantly Nb^V. This is in agreement with other XPS studies which came to conclusion that niobium oxides tend to

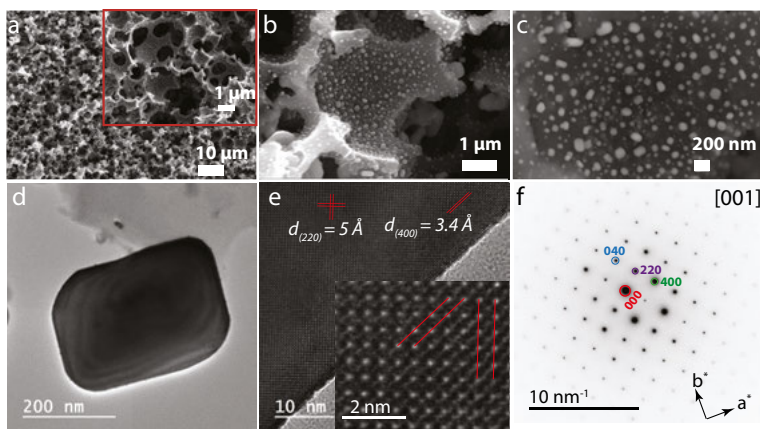


Figure 6.1. The microstructure of the carbon foams coated with niobium oxides has been probed using electron microscopy. The scanning electron micrographs of the carbon foam coated in niobium oxide nanoparticles were taken at various magnifications and at an accelerating voltage of 10 kV. The SEM in (a) is representative of the general topography of the electrodes, which feature open-celled macropores interconnected via windows. The inset image better reveals the cellular topography of the carbon foams and was taken at 3 kV and 2.6 mm distance. The niobium nanoparticles are more visible in the SEM given in (a) and exhibit a wide size distribution. Both (a) and (b) were images were obtained using the secondary electrons. In order to achieve contrast between the carbon and the oxides, the back-scattered electrons were used to collect the micrographs (c). The particles which appear brighter in the SEM represent niobium oxides, as the intensity of the scattered electrons scales directly with the atomic number of the elements in the specimen. Further analyses were conducted on the oxides using transmission electron microscopy. From the particle shown in (d), HRTEM image (e) and SAED pattern were collected and used to identify the crystal structure of the oxide.

oxidize at the surface upon exposure to air [238]. The bulk composition and structure were investigated using electron energy loss spectroscopy (EELS). In EELS, the distribution of the changes in the energy of an electron beam that has passed through a thin specimen is analyzed to determine the composition, the electronic structure and the phase of the substance in the specimen. The full spectrum consists of the zero-loss peak (ZLP), the low-loss region (roughly up to 50 eV) and the core-loss region. The various regions of the EEL spectrum of the niobium oxides can be seen in *Figure 3* in Paper V. Perhaps, the most useful part of the spectrum that can be used for 'fingerprinting' is the O-K edge and its electron loss near edge structure (ELNES). In *Figure 3 f*) in Paper V, the O-K edge, attributed to 2s electrons transitioning to empty 2p states, is shown in the range from 532 to 580 eV. Usually, the O-K shows a pair of peaks for NbO_2 and Nb_2O_5 whose intensity ratio depends on the occupancy of the 4d states. The pair of poorly resolved peaks which are equal in intensity, designated by a and b, alongside the fine structures, designated by c

and d, are typical of NbO_2 . Detailed EELS analysis of various niobium oxides can be found in the literature [239].

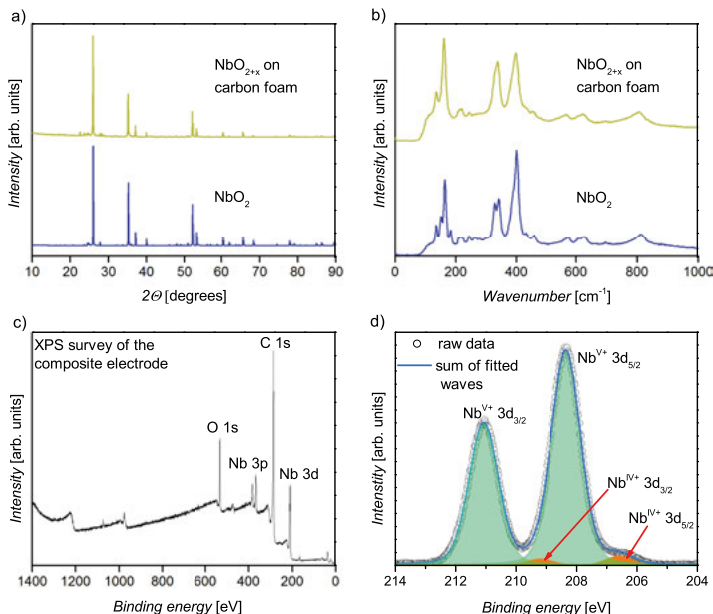


Figure 6.2. Insight into the crystal and electronic structures of niobium oxides was sought with the help of x-ray diffraction, Raman spectroscopy and photoelectron emission spectroscopy. Based on the XRD patterns for the as-prepared niobium dioxide and commercial niobium dioxide shown in (a), the most intense peaks can indicate the presence of NbO_2 . Similarly, the Raman spectrum (b) also bears close resemblance to the commercial NbO_2 . The oxidation states of niobium cations can be determined from the XPS spectrum in (d) after peak deconvolution. The overview of the elements present in the NbO_2 -coated carbon foam can be noted in the survey spectrum in (c).

6.3 Structural investigation: mixed oxides $\text{Mo}_3\text{Nb}_2\text{O}_{11}$

As much as electronic and ionic charge transport pathways are required in redox active materials, electrode formulations are expected to incorporate adequate conductive additive for electronic wiring and continuous porosity to make for percolation of ions in the electrolyte. The utility of highly networked carbon matrices increases the effective electrical conductivity of the 3D heterogeneous nanocomposites. Pieces of carbon foams were added into the solution and left to soak in there for 2 days to allow for infiltration of the solution into the accessible pores present in the carbon foam. The carbon foams coated in the sol were then dried first in ambient conditions at 90°C for two days and then at 300°C to complete conversion into amorphous oxide nanoparti-

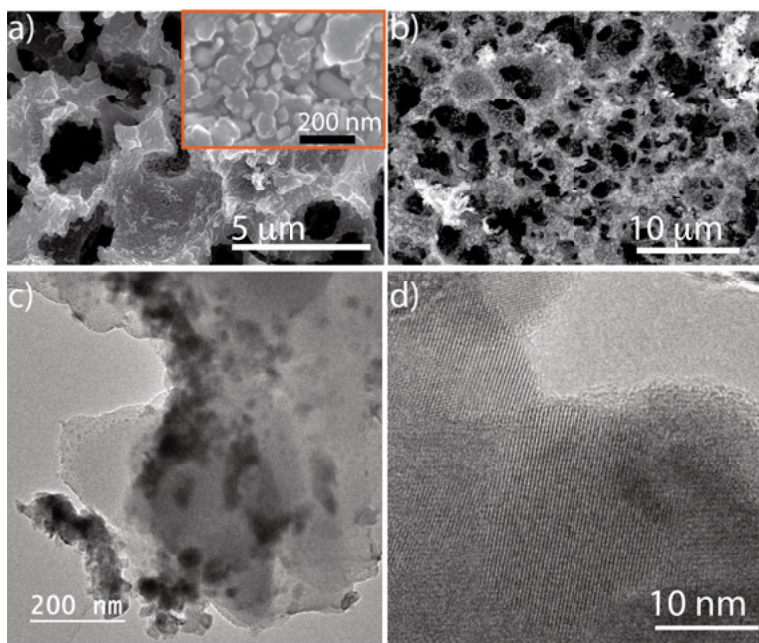


Figure 6.3. Electron microscopy characterization of emulsion-templated carbon foam coated in $\text{Mo}_3\text{Nb}_2\text{O}_{11}$ through sol-gel approach followed by carbothermal reduction at 750 °C: the scanning electron micrographs recorded by collecting a) the secondary electron and b) the back-scattered electron signals. The high resolution transmission electron micrographs (HRTEM) of the samples display in c) the distribution inside the carbon foams and d) the crystallinity of the oxide nanoparticles

cles. The reduction of MoO_3 to MoO_2 and crystallization of $\text{Mo}_3\text{Nb}_2\text{O}_{11}$ were carried out in Ar atmosphere at 600 °C (5 h) and 750 °C (2 h). The SEM and TEM images given in *Figure 6.3* show crystalline particles distributed throughout the porous carbon structure. Specifically, the back-scattered electron micrographs help identify the oxide nanoparticles, in which they appear brighter due to Z-contrast. Powder X-ray diffraction patterns of the oxide after thermal annealing are shown, alongside that of MoO_2 , in *Figure 6.5*. As expected, the material treated at 300 °C is entirely amorphous as indicated by broad XRD pattern, whereas higher temperature treatment give rise to highly crystalline product as verified by the peaks observed in the XRD pattern. The open tunnel frameworks desired for reversible lithium cycling are only available in well-crystallized oxides and thus only the high temperature material has been pursued here for electrochemical testing. Evidence regarding the oxidation states of the transition metal cations has been gathered using XPS, shown in *Figure 6.4*. As expected, the surface of the oxides heated in air at 300 °C consists mainly of molybdenum in the form of Mo^{VI} and niobium Nb^{V} . Upon heat treatment at 750 °C, the molybdenum trioxide undergoes reduction with carbon to form molybdenum dioxide, while the pentavalent niobium remains

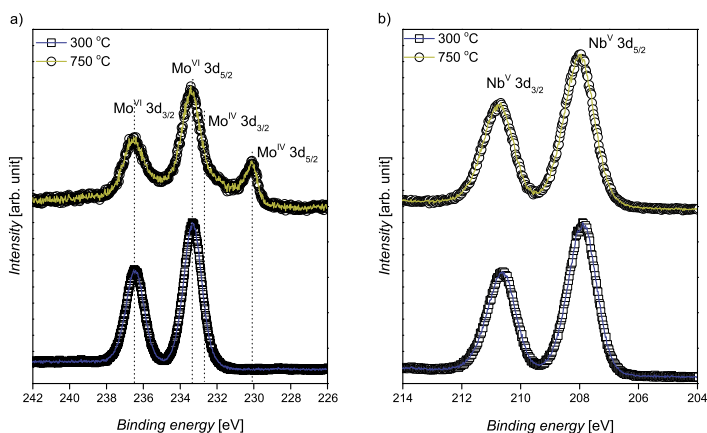


Figure 6.4. The X-ray photoelectron spectra of $\text{Mo}_3\text{Nb}_2\text{O}_{11}$ deposited on carbon foam through sol-gel approach and treated at 300 and 750 °C. In a) Mo^{VI} is reduced by the carbon foam to Mo^{IV} after being treated 750 °C, whereas b) the Nb^{V} remains unaffected.

unaltered. The synthesis approach discussed in this paper may be transferred

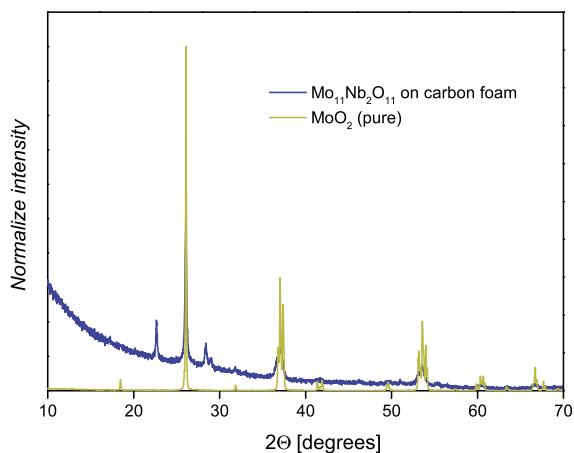


Figure 6.5. The XRD patterns of MoO_2 and $\text{Mo}_3\text{Nb}_2\text{O}_{11}$

to the preparation of other mixed oxides like which are commonly used in the partial oxidation of organic compounds.

6.4 Electrochemical behaviors and rate performance: $\text{NbO}_{2+\delta}$

Comprehensive insight into the electrochemical behavior of the oxides and the rate capability of the electrodes was obtained based on data collected through cyclic voltammetric and controlled-current experiments. The CVs recorded at varying scan rates are depicted in *Figure 6.6*. As can be observed in *Figure 6.6 a)*, multiple peaks can be seen for the redox reactions of $\text{NbO}_{2+\delta}$. It is well-known, and as discussed in the preceding section, that Nb^{V} is the most stable oxidation state of niobium and thus the oxide NbO_2 is prone to surface oxidation upon exposure to air, i.e. pentavalent niobium is detected at the surface of the tetra- and di-valent oxides. The CV given in *Figure 6.6 a)* shows a pair of peaks at around 1.64 and 1.72 V vs. Li^+/Li due to the $\text{Nb}^{\text{V}}/\text{Nb}^{\text{IV}}$ redox couple. The other peaks, 1.34 and 1.37 V, 1.18 and 1.31 appear below 1.5 V, which can be attributed to redox reactions entailing the conversion of Nb^{IV} to Nb^{III} , and vice versa. The overall electrode reaction for the mixed valence oxides can be expressed as



In *Figure 6.6 c)* plots of the total charges passed in the course of electrode reactions are plotted as a function of the square root of the scan rates. As suggested by Ardizzone et al. [248], the following relation

$$Q(\nu) = Q_s + Q_b \quad (6.2)$$

$$Q(\nu) = Q_s + \text{constant}(1/\sqrt{\nu}) \quad (6.3)$$

can be employed to evaluate the contributions of the surface and bulk lithiation to the overall charge as a function of scan rate. In this relation, $Q(\nu)$, Q_s , and Q_b represent, respectively, the total charge associated with the given scan rate ν , charge contributions from the surface activities and the bulk diffusion of the lithium ions occurring during the redox reactions of the active materials. Accordingly, at scan rates up to 6 mV s^{-1} , the time scale of the experiment is long enough to let the lithium ions diffuse into bulk of the active materials and most of the active material can react to provide considerably high capacity. At a scan rate of 9.5 mV s^{-1} , it can be noted that almost half of the slow scan rate (0.05 mV s^{-1}) capacity can be obtained. In contrast, fast scan rates, curtail the extent of diffusion into the electrode bulk and hence the capacity drops rapidly with increasing scan rates [232, 234, 248]. The total charge is mainly due to redox active sites at the surface, which are more accessible to the lithium ions than the bulk is.

The rate capability of the electrode was also investigated by applying different current densities. The galvanostatic curves are given in *Figure 6.6 d)* and *6.6 e)*. The prominent redox plateaus which occur around 1.65 and 1.69 V vs Li^+/Li for discharge and charge, respectively, are associated with the Nb^{V}

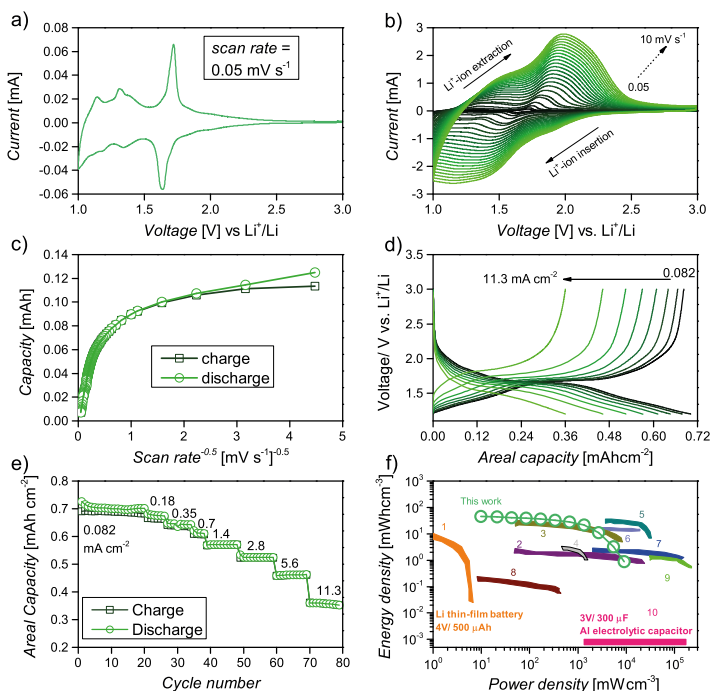


Figure 6.6. In the CV of the composite electrode (a) recorded at a scan rate of 0.05 mV s⁻¹, it can be noted that a pair of redox peaks appear at around 1.64 and 1.72 V vs. Li⁺/Li on reduction and oxidation, respectively. More less intense peaks (1.34 and 1.37 V, 1.18 and 1.31, and a clear oxidation peak at 1.14 V) appear below 1.5 V, which can be attributed to redox reactions entailing the conversion of Nb^{IV} to Nb^{III} and vice versa. The trend and change in position and shape of the peaks with increasing scan rate can be noted in CVs in (b). The scan rates are 0.05, 0.1, 0.2, 0.4, 0.8, 1, 1.5, 2, 2.5, 3, 3.5 to 10 mV s⁻¹. A plot of the charges passed during reduction and oxidation, corresponding to each CV in (b), are presented as a function of the inverse of the square-root of the scan rates (c). The voltage-capacity profiles of the electrodes recorded at current densities ranging from 0.082 to 11.3 mA cm⁻² (d) are used to establish the rate capability of the oxides, along with the cyclability over many cycles (e). A Ragone plot has been prepared to make comparisons with carbon-based supercapacitors and pseudocapacitors consisting of MnO₂ reported in the literature: (1) lithium thin film battery [240], (2) all-solid-state patterned porous carbon micro-supercapacitor [241], (3) laser-scribed graphene-MnO₂ asymmetric micro-supercapacitor [242], (4) MnO₂-reduced graphene oxide micro-supercapacitor [243], (5) activated carbon micro-supercapacitor [240], (6) MXene micro-supercapacitor [244], (7) graphene-based micro-supercapacitor [245], (8) MnO₂-coated carbon fiber micro-supercapacitor [246], (9) carbon onions micro-supercapacitor [240], and (10) Al electrolytic capacitor [247].

cations. Almost half of the capacity is obtained below the plateaus, which indicates that further reduction of the Nb^{IV} cations to Nb^{III} makes significant contribution to the total charge. Additionally, the power performance given in *Figure 6.6 e*) indicate the active materials can sustain high current densities. At 11.3 mA cm^{-2} , which is about 140 times the lowest current density, about 50 % of the capacity is accessible. For good power performance, not only nano-structuring of the active materials, but also excellent electrical conductivity in the active materials is necessary. Detailed analysis of the internal cell resistance of the electrode is given *Figure 5* in Paper V.

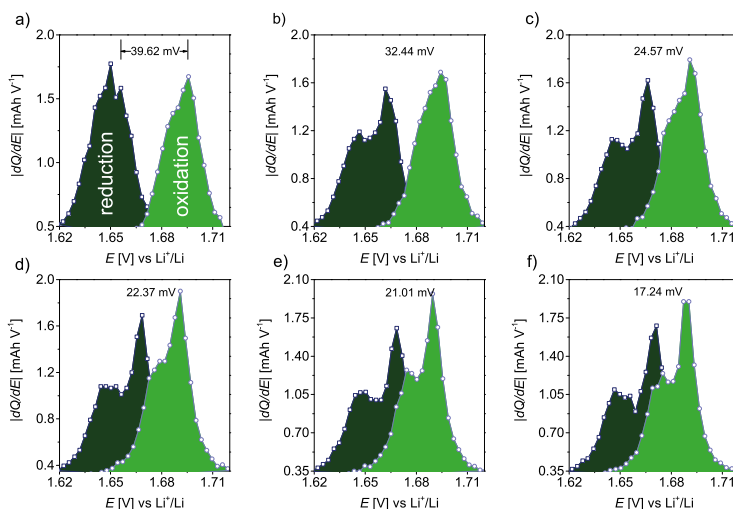


Figure 6.7. Plots of differential capacities as functions of voltages show the continuous changes in the positions of the peaks corresponding to the reduction and oxidation of NbO_2 tethered on carbon foams. The plots from a) to f) represent the respective differential capacities of 1, 2, 5, 10, 15, and 20th cycles for the electrode cycled at 0.082 mA cm^{-2} . The decrease in the potential differences between the pairs of peaks is indicative of improved electrical conductivity and charge transfer kinetics in the electrodes during electrochemical cycling.

6.5 Lithiation-induced enhancement of charge transfer kinetics

Lithiation-driven semiconductor-to-metal transition was observed in MoS_2 and has been attributed to structural transformations to more electronically conductive phase [249]. Similar behavior was reported by Kong *et al.* in niobium oxide nanoparticles. [233] Studies using voltammetric, current-controlled and staircase potentiostatic electrochemical impedance techniques were conducted in Paper V to provide further evidence to the existence of similar behaviour in

over-stoichiometric NbO₂. The data presented in Paper V show that electrochemical lithiation of over-stoichiometric NbO₂ results in progressive decrease in the internal cell resistance. This behavior is manifest in the continuously decreasing peak-to-peak potential difference between the reduction and oxidation peaks in the differential capacity plots shown in *Figure 6.7*. In the differential capacity-voltage plots, the voltage difference between the pair of redox peaks is a measure of the hysteresis in the corresponding galvanostatic curve. It can be observed that the peak-to-peak voltage difference decreases from 38.02 mV to 17.24 mV over the first 20 cycles indicating that some form of structural and/or electronic transformation has occurred. The redistribution of the Nb^V cations from the surface to the bulk of the materials can potentially affect electronic structure of the oxides. Further study is required in order to accurately determine these changes. The plots from a to f represent the differential capacities for the cycles 1, 2, 5, 10, 15, and 20, respectively. The progressive decrease in the hysteresis can be indicative of decrease in cell resistance as a result of enhanced charge transfer kinetics across the electrode interface and increase in the electrical conductive of the active materials.

More evidence has been obtained from EIS studies. The plot in *Figure 6.8 c*) displays the general trend in the charge transfer resistance for a selected number of cycles. For sufficiently small potential amplitude of the AC excitation signal, the Butler-Volmer current-overpotential relation can be linearized [46] to give

$$R_{ct} = \frac{RT}{Fi_0} \quad (6.4)$$

where R_{ct} , R , T , F and i_0 stand for the charge transfer resistance, the ideal gas constant (8.314 J mol⁻¹ K⁻¹), the temperature in K, the Faraday constant (96485.3329 C mol⁻¹) and the exchange current. Accordingly, decreasing charge transfer resistance implies increasing exchange current density which is indicative of the kinetic reversibility of the electrode reactions. The exchange current characterizes the rate of the electron-transfer processes inside the redox couple. To ascertain if any structural changes occurred during the electrochemical cycling *ex situ* XRD was performed on the electrodes stopped at various states of charge. The results can be found in *Figure S5*. Based on the XRD patterns no detectable structural changes or phase transformations occur during electrochemical cycling of lithium in the oxides. Better kinetic facility leads to improved power performance which indicates in turn that the mixed valence oxides are suited for microbattery applications.

6.6 Electrochemical behaviors and rate performance: Mo₃Nb₂O₁₁

Most redox active materials which exhibit high charge transfer kinetics are characterized by open crystallographic frameworks and semiconducting to

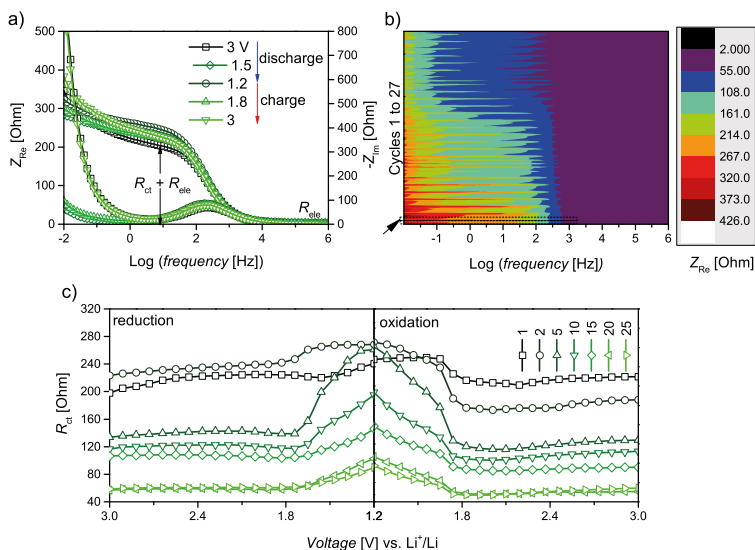


Figure 6.8. Electrochemical impedance spectroscopy study of the NbO_2 electrodes on a carbon foam polarized at various DC potentials and investigated with an AC voltage of amplitude 10 mV and a frequency range of 1 MHz to 10 mHz. The real and imaginary parts of the impedance are plotted in (a) as a function of the logarithm of frequency to help estimate the magnitudes of the electrolyte resistance and the charge transfer resistance for the first cycle. Similar analyses on the 27 cycles show the general trend in the electrode kinetics. The contour color map in (b) presents the whole data collected for the first 27 cycles (1134 EIS data curves). The arrow at the bottom on the left-hand side of the plot points to the box circumscribing the first discharge-charge cycle. (c) Selected values of the charge transfer resistance for cycles 1, 2, 5, 10, 15, 20 and 25 are given as a function of voltage against lithium.

metallic conductivities. High rate lithium ion cycling in these materials occurs via topotactic mechanism favored by two-dimensional layered structures or three-dimensional tunnel structures. Examples recognized for combining favorable intrinsic electronic and ionic conduction pathways include $T-Nb_2O_5$, and hydrogen titanates, particularly $H_2Ti_3O_7$, and their ultimate thermolysis product $B-TiO_2$ [232, 250–252]. Redox-active materials suited for high rate cycling are characterized by fast electron and ion transfer kinetics and do not entail drastic structural/phase changes during lithium insertion and removal. On top of that, it is desirable that they possess high electronic conductivities sufficient to let electrons tunnel across the current collector-active material interface with minimal resistive losses. Carbothermal reduction of MoO_3 yields MoO_2 which is known to be metallic and can be used as a high voltage anode in lithium-ion batteries [253]. Particularly, in its nanosized form it has been discovered to be extrinsic pseudocapacitor [254]. Hence, MoO_2 nanoparticles tethered on 3D electrodes are well-suited for high power microbattery applica-

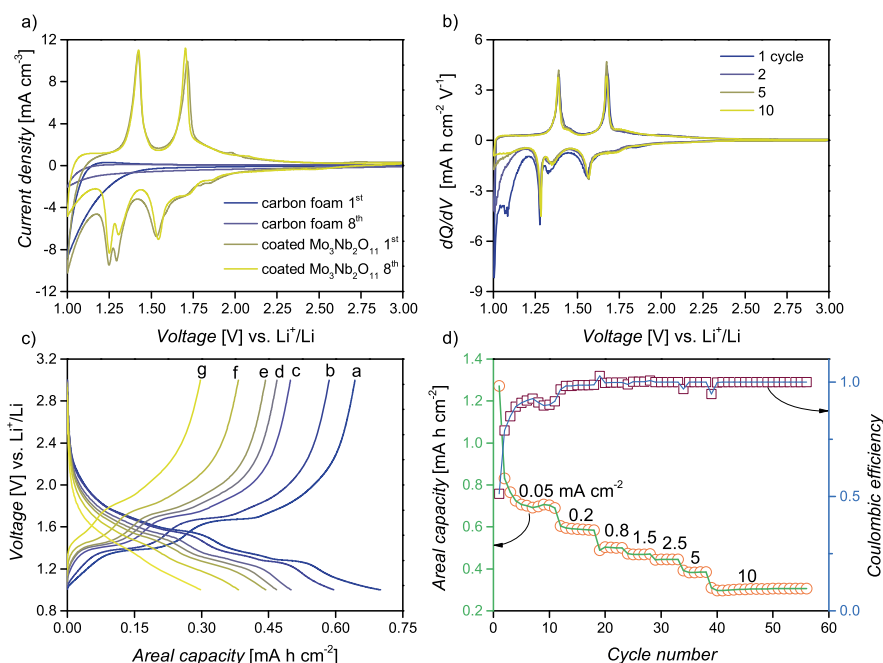


Figure 6.9. The electrochemical performance of $\text{Mo}_3\text{Nb}_2\text{O}_{11}$ deposited onto carbon foam substrates. a) CVs of the coated and bare carbon foams for the 1st and 8th cycles b) the differential capacity-voltage curves of the coated carbon foam electrodes for selected cycle numbers c) voltage-capacity curves recorded at various current densities and d) the rate performance of the electrodes is shown along with the corresponding coulombic efficiencies

tions. As described above, $\text{Mo}_3\text{Nb}_2\text{O}_{11}$ nanoparticles, which is formed from a mixture of MoO_2 and Nb_2O_5 in a 3:2 ratio, was synthesised through a sol-gel approach. The electrochemical performance of the mixed molybdenum-niobium oxide is displayed in Figure 6.9. It should be noted that the origin of the capacity loss observed during the first discharge process is mainly parasitic reaction involving the surface functional groups of the carbon foam. This is manifest in the cyclic voltammogram (CV) of the bare carbon foam, as shown in Figure 6.9 a) along with that of the coated electrode. Probably, the capacity loss could be reduced if carbon foams produced at higher temperatures could be used instead. The overall rate performance of the electrode, as can be seen in Figure 6.9 c), is good both in terms of capacity retention especially up to 5 mA cm^{-2} and cycling stability. Even at a current density of 10 mA cm^{-2} , the electrochemical cell could deliver an area capacity around 300 $\mu\text{Ah cm}^{-1}$ which is higher than what most thin film microbatteries can provide. Thus, this material can be worth investigating further for application in high power density microbatteries.

7. Exfoliation-Deposition of Metal Oxides: A Facile Approach to Material Deposition on Carbon Substrates

Among the hottest and topical research areas in materials science in recent years is the study of the graphene analogues of inorganic materials including transition metal oxides, nitrides, carbides and chalcogenides. An upsurge in the electrochemical study of these materials has recently been witnessed largely owing to their higher electrical conductivities and interfacial surface areas as opposed to their bulk counterparts. This chapter highlights a work on the synthesis and electrochemistry of hydrated V_2O_5 nanosheets obtained through exfoliating VO_2 crystals. Fabrication of freestanding electrodes has been achieved by depositing the exfoliated oxide nanosheets directly onto carbon nanotube paper. Ensuing thorough structural investigations, the composite electrodes were studied for potential application in lithium batteries. The effect of oxide film thickness on the electrochemical performance has been investigated as well.

7.1 Exfoliation of VO_2 (B) in water

A colloidal suspension of vanadium oxide nanosheets was prepared by exfoliating VO_2 (B) in water. The precursor material was synthesised from NH_4VO_3 via the hydrothermal approach reported by Xie *et al.* [255]. To effect the exfoliation of the bulk VO_2 was (i) dispersed in de-ionized water and sonicated for about 30 minutes, and (ii) refluxed for several days (1 to 7) with the temperature ranging from 20 to 70 °C. Upon completion, a dark green solution of $V_2O_5 \cdot xH_2O$ was obtained. The suspension of exfoliated oxide nanosheets was then drop-cast onto pieces (1 to 2 cm disks) of multi-walled carbon nanotube paper (MWCNT, NanoTechLabs, US) to fabricate free-standing composite electrodes. Controlled amounts of the suspension were applied on the MWCNT paper disks. After evaporation of the solvent, oxide films with varying thicknesses were achieved.

7.2 Hydrated $V_2O_{5-\delta}$ nanosheets from exfoliated VO_2

Atomically thin materials, especially transition metal oxides and dichalcogenides, are currently in the spotlight of research owing to their intriguing

chemical, electronic, optical, mechanical, catalytic and electrochemical properties. In general, they can be prepared by exfoliating bulk materials mechanically or in suitable solvents, or by bottom-up approaches including chemical vapor deposition [256–258]. Nanosheets of hydrated V_2O_5 were prepared through exfoliation of VO_2 crystals in water. As described in the experimental section, the bulk material undergoes morphological and structural changes as the exfoliation process progressed for several days. In *Figure 1* in Paper VI, the X-ray diffraction (XRD) patterns indicate that the structure of the precursor material changes upon water insertion and further exfoliation. After 6 days of refluxing in the solvent, the XRD patterns display only the peaks corresponding to the $(00l)$ planes, which indicate the expansion of the interlayer distance along the c -direction. The microstructures and morphologies of the exfoliated oxide nanosheets are shown in *Figure 7.1*. In contrast to the bulk, the exfoliated products are composed of an assemblage of nanosheets with significantly less ordering as evidenced by the rings in the selected area electron diffraction in *Figure 7.1 a*). In the course of exfoliation, about 80 % of the V^{IV} cations in the precursor undergo oxidation to V^V based on chemical and spectroscopic evidence. The X-ray photoelectron and X-ray absorption near-edge structure spectra displayed in *Figure 7.2* prove the existence of mixed valent vanadium in the oxide nanosheets. The electrode active material will be represented as $V_2O_{5-\delta} \cdot nH_2O$.

7.3 Deposition of hydrated $V_2O_{5-\delta}$ nanosheets on carbon nanotube paper

To fabricate self-supporting electrodes, predetermined amounts of the colloidal dispersion of the exfoliated materials were poured onto pieces of multi-walled carbon nanotube paper (MWCNT). Layers of hydrated V_2O_5 measuring from 4 to 45 μm were obtained as the solution dries up. The thickness of the oxide films was controlled by varying the concentration of the dispersions, as can be seen in *Figure S5* in Paper VI.

7.4 V_2O_5 -coated CNT paper as a freestanding cathode for lithium batteries

Many published articles exist on the synthesis and electrochemical investigations into vanadium oxides nanostructures [259–262]. The fabrication of composites of vanadium oxides and carbon nanomaterials has also been widely reported [263–268]. The main objective of the work detailed in this chapter is to present exfoliation-deposition as a viable strategy for the deposition of metal oxide nanostructures on carbon substrates. In this study, flexible electrodes made of $V_2O_{5-\delta} \cdot nH_2O$ nanosheets physically tethered onto pieces of

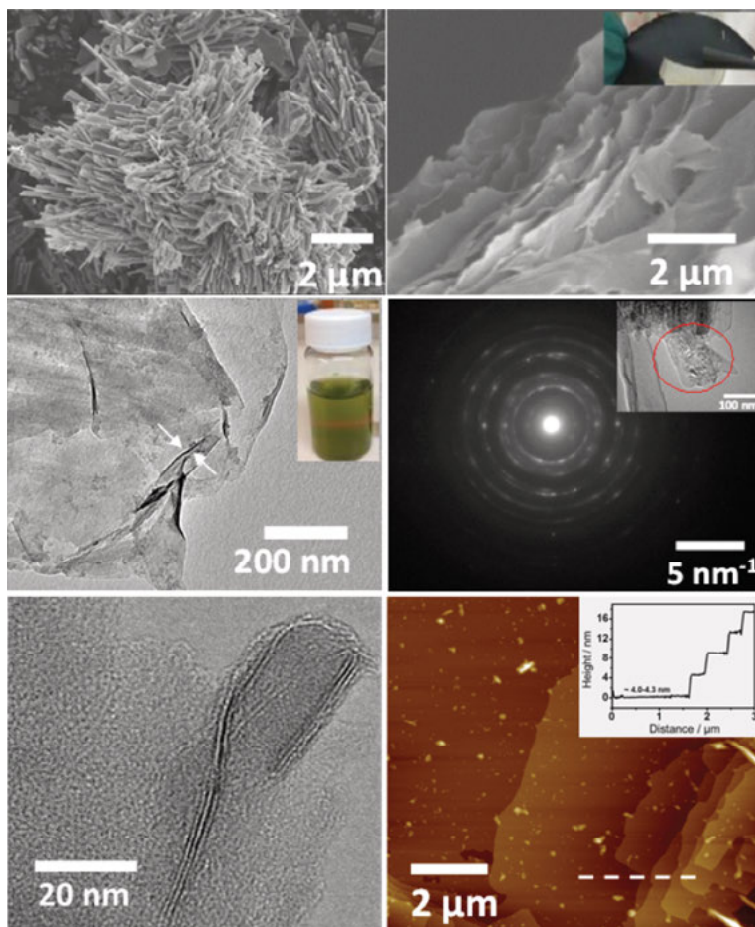


Figure 7.1. (a) and (b) SEM image of bulk $\text{VO}_2(\text{B})$ and the exfoliated $\text{V}_2\text{O}_{5-\delta} \cdot n\text{H}_2\text{O}$ nanosheets, respectively; inset in (b) photograph of a free-standing film of the exfoliated $\text{V}_2\text{O}_{5-\delta} \cdot n\text{H}_2\text{O}$ nanosheets. (c) TEM image of the exfoliated nanosheets; inset in (c) photograph for Tyndall effect of the exfoliated nanosheets dispersed in water. (d) SAED pattern obtained from the highlighted area in the inset TEM image. (e) HRTEM image for $\text{V}_2\text{O}_{5-\delta} \cdot n\text{H}_2\text{O}$ nanosheets showing that the thickness is about 3-4 layers; and (f) AFM image of exfoliated nanosheets; inset in (f) height profile of the highlighted dashed line. Reproduced from Paper VI by permission of ©2016 The Royal Society of Chemistry

multi-walled carbon nanotube (MW-CNT) paper. Four electrodes designated by VO-45, VO-12, VO-7, and VO-4 were prepared with the thicknesses of the active materials being 45, 12, 7, and 4 μm . Electrochemical investigation into these electrode was conducted using cyclic voltammetry (CV) and controlled-current methods. The CVs of the three electrodes were recorded in the voltage range from 1.7 to 3.9 V vs. lithium at a scan rate of 0.05 mV s^{-1} are given in *Figure 7.3 a*). As can be seen in the CVs, the electrochemical lithiation of the

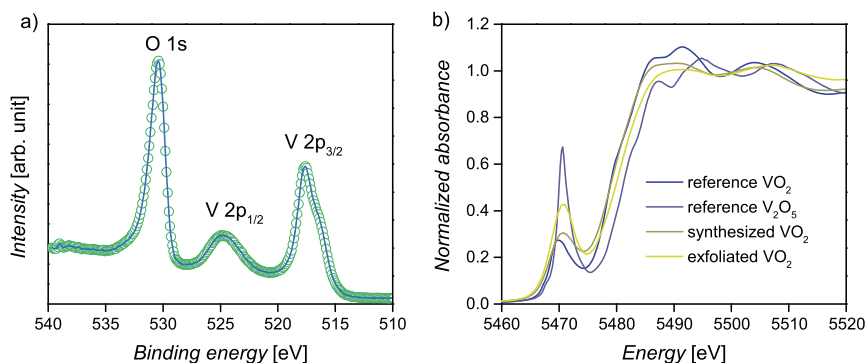


Figure 7.2. The X-ray photoelectron and X-ray absorption fine structure spectra of the hydrated sheets of $V_2O_{5-\delta} \cdot nH_2O$

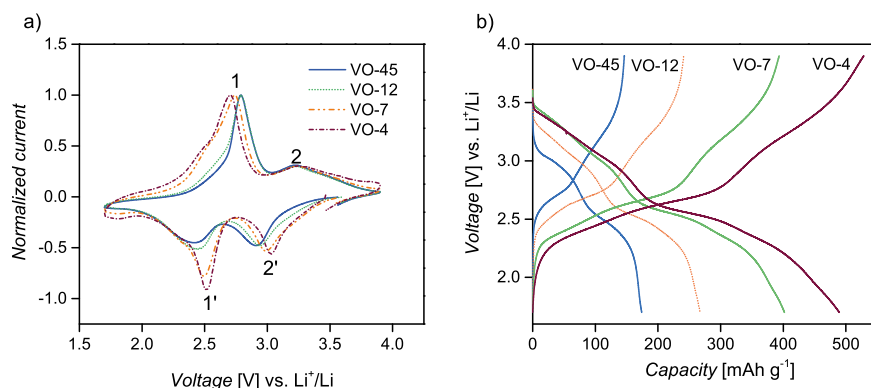
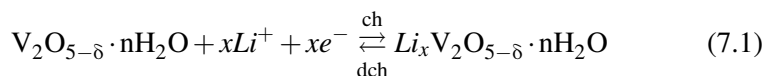


Figure 7.3. Comparison of the electrochemical behaviors of the four electrodes which are designated as VO-45, VO-12, VO-7 and VO-4. a) Cyclic voltammograms at a scan rate of 0.05 mV s⁻¹. b) Discharge and charge curves of the electrodes at an applied current of 10 mA g⁻¹

$V_2O_{5-\delta} \cdot nH_2O$ nanosheets is characterized by two pairs of redox peaks occurring at different potentials. The peaks are designated as 1 and 2 for oxidation, and 1' and 2' for reduction. The electrochemical reaction involving lithium insertion into the nanosheets can be expressed as:



The galvanostatic curves of the four electrodes recorded at a current density of 10 mA g⁻¹ are shown in Figure 7.3 b). In contrast to crystalline phases of V_2O_5 [269], only sloping voltage-capacity profiles are observed, typical of amorphous vanadium oxides [270]. The exfoliated nanosheets of $V_2O_{5-\delta} \cdot nH_2O$ can be reduced to 1.7 V vs. Li and no change in the voltage profiles can

observed. This can possibly be owed to the less ordered structure of the exfoliated nanosheets and the increased interlayer distances caused by the exfoliation process owing to intercalated water molecules [271]. Consequently, the nanosheets possess high interfacial electrode area and increased lithium-ion mobility between the oxide layers. The lithium insertion, therefore, can occur in these structures without causing substantial structural alterations in comparison to crystalline V_2O_5 . The effect of interfacial surface area becomes more pronounced as the thickness of the $\text{V}_2\text{O}_{5-\delta} \cdot n\text{H}_2\text{O}$ decreases (VO-4), and thus the discharge capacities increase progressively as 174, 267, 402 and 489 mAh g^{-1} for the electrodes whose thicknesses are 45, 12, 7 and 4 μm . Further insight into the electrode kinetics is obtained from the electrochem-

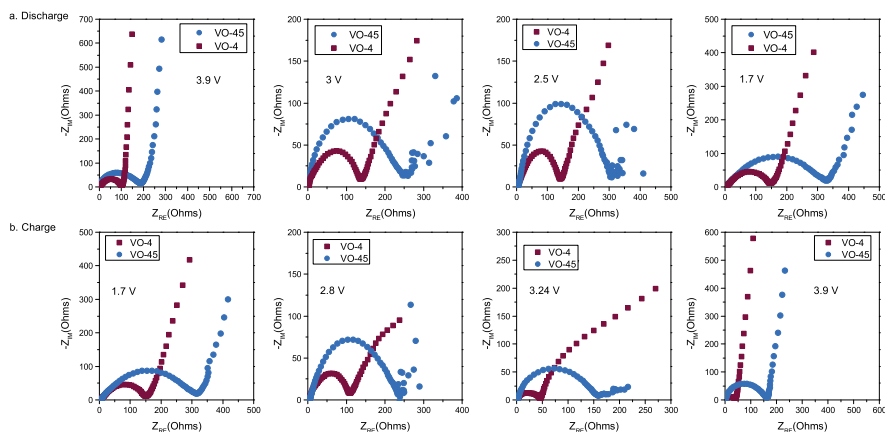


Figure 7.4. Electrochemical impedance spectroscopy (EIS) data collected for electrodes VO-45 and VO-4 at various DC voltages during discharge (a) and charge (b).

ical impedance spectroscopy (EIS) data collected at several state-of-charge for both electrodes during discharge and charge. These data are presented as Nyquist plots in *Figure 7.4* which indicate the thicker electrode suffers from more sluggish kinetics as compared to the electrode with thinner oxide film. This accounts for the fact that electrode VO-4 can be cycled at much higher scan rates with much less severe resistive losses. As pointed out above, electrochemical lithiation of vanadium oxides is characterized by several phase transformations depending on the depth of discharge. Usually, deep discharge causes irreversible structural changes. To find out if similar changes occur in the exfoliated nanosheets, electrodes VO-45 and VO-4 were cycled at a current density of 10 mA g^{-1} . The electrochemical behaviors of the two electrodes over the first few cycles can be noted in *Figure 7.5*. The first discharge curve for electrode VO-45 exhibits more discernible difference, versus VO-4, as compared to the subsequent cycles. This observation can be explained based on the fact that structural changes become less drastic for thinner oxide films as compared with electrode VO-45. Hence, the electrode kinetics

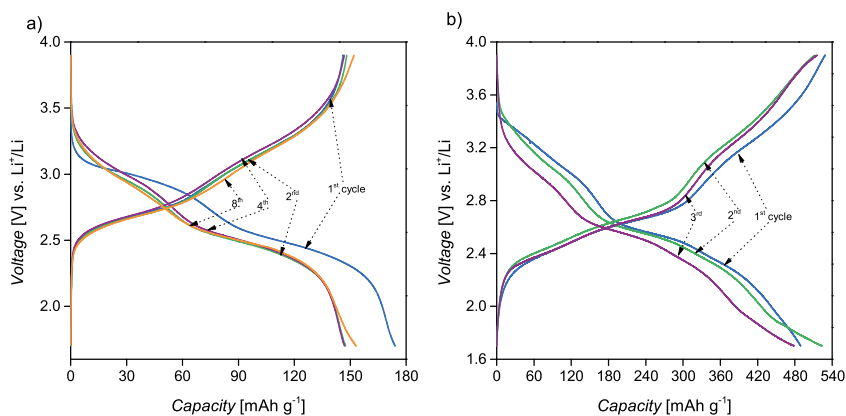


Figure 7.5. The voltage-capacity curves for electrodes a) VO-45 and b) VO-4 display their electrochemical behaviors for the first few cycles.

and charge storage processes in the exfoliated $V_2O_{5-\delta} \cdot nH_2O$ nanosheets are affected by the thickness of the oxide layers deposited on the CNT paper. The conductivity and electrochemical kinetics of the electrodes investigated in this work could be improved if the thickness of the $V_2O_{5-\delta} \cdot nH_2O$ coating can be reduced even further.

8. Conclusions and Outlook

This thesis has set out the synthesis, optimization, and applications of carbon foams that are derived from high internal phase emulsion polymers (poly-HIPEs). In conclusion, the works presented in this thesis have concentrated on two issues of paramount importance to microbattery research:

- *fabrication and optimization of 3D electrode designs based on emulsion-templated carbon foams*
- *synthesis of active materials suited for use in lithium-ion microbatteries*

Synthesis of emulsion-templated carbon foams

The synthesis of the carbon foams begins with the preparation of styrene-based high internal phase emulsion (HIPE) polymers that are extremely porous and fully networked. Due to their tendency to volatilize at elevated temperatures, styrene-based polyHIPEs cannot be carbonized readily without prior chemical modification. Sulfonation is commonly carried out to introduce potential moieties ($-\text{SO}_3\text{H}$) for crosslinking during pyrolysis. In this work, a range of techniques have been used to elucidate the chemical transformations the sulfonic acid groups undergo as a function of temperature. Thermogravimetric and spectroscopic analyses indicate that thioether ($-\text{C}-\text{S}-$) crosslinks form at the expense of the sulfonic acid groups during pyrolysis. Due to the increase in the extent of cross-linking and thus the enhancement in thermal stability, the sulfonated polymer tends to pyrolyze at a bit higher temperature and with much less volatilization as compared to the pristine polymer. Consequently, highly networked and rigid carbon foam can be prepared from sulfonated polyHIPEs. According to XPS and mass spectrometry measurements, the carbon foam has oxidized surface and contains residual sulfur species even when synthesized at temperatures as high as 1200°C . Efforts have been made to optimize the void size distributions, specific surface areas, and surface chemistry of the carbon foams. Results obtained indicate that void dimensions are strongly correlated to the homogenization speed used in preparing the HIPE precursor using rotor-stator. Exploiting the rheological properties of HIPEs offers a unique opportunity to optimize the dimensions of the open-cells and the interconnecting voids. By varying the rotational speed of the homogenizing mixer from 500 to 2000 rpm, it was observed that the void size distributions get narrower, with the corresponding mean void sizes being 24 and $3.3\text{ }\mu\text{m}$. As far as the application of the carbon foams as freestanding anodes is sought, it is desirable for

the void sizes to be as small as possible in order to reduce the dead volume occupied by the electrolyte. This work demonstrates that the voids of the carbon foams can be reduced even further if higher rotational speeds can be employed while preparing the HIPEs. In addition, increasing the pyrolysis temperature is observed to lead to decreasing specific surface areas and higher degree of graphitization, which are known to promote the electrochemical performance of carbon materials in storing lithium ions with higher cycling stability. The BET specific surface areas decrease from 525 to 11 m² g⁻¹ as the pyrolysis temperature is increased from 1000 to 2200 °C. From applications perspectives, the bespoke carbon foams have been implemented as

- monolithic anodes for storing lithium ions
- three-dimensional scaffolds for active materials
- reactor for carbothermal reduction to synthesize niobium and molybdenum oxides

Emulsion-templated carbon foams as freestanding 3D anodes

Typical of disordered carbons, the carbon foam prepared at 700 °C is observed to consume considerable amount of lithium ions during the first discharge due to parasitic reactions that lead to surface passivation (SEI layer) and reduction of oxygen containing surface functional groups. This would limit the use of the carbon foam as anode material in practical microbatteries. Only after pre-cycling to bypass the initial the capacity loss can the low temperature carbon foam can be used in practical cells. Over the subsequent cycles, a stable cycling capacity of 3.5 mAh cm⁻² has been obtained. The ensuing effort has focused on the optimization of the electrode characteristics including the void sizes and degree of graphitization. A set of carbon foams has been prepared at 1000, 1500 and 2200 ° and fully characterized using various techniques. The increasing thermal treatment leads to more structural order, reduced specific surface areas and suppressed extent of electrolyte decomposition in the course of initial lithiation of the carbon foams. High areal capacities of 1.22 and 1.03 mAh cm⁻² are obtained when the carbon foams were cycled at 50 and 500 μA cm⁻². Above all, the coulombic efficiency tends to improve with increasing pyrolysis temperature. Initially, the carbon foams prepared at 700, 1000, 1500, and 2200 °C exhibited coulombic efficiencies around 31.4, 41.6, 48.5, and 76 %, respectively. It is worth noting that all the samples possessed different specific surface areas, and consisted of varying amounts of heteroatoms in the form of surface functionalities; hence, not only the amount of electrolyte decomposition but also the shapes of the cyclic voltammograms and galvanostatic curves are different.

Emulsion-templated carbon foams as 3D scaffolds for cathode materials

To demonstrate the feasibility of the carbon foam as a current collector for other active materials, layers of PANI and LiFePO_4 have been deposited by electrodeposition and sol-gel method, respectively. Conformal coatings with a polyaniline cathode material have been observed to deliver areal capacities of $500 \mu\text{Ah cm}^{-2}$ and a reasonable rate performance. A stable capacity is noted for more than 90 cycles. Therefore, we conclude that these foam substrates are also ideal candidates for use in lithium-ion batteries as architected current collectors. Similarly, the LiFePO_4 -coated carbon foam has been studied thoroughly to establish its potential use for 3D microbattery applications. Electron microscopy characterizations reveal that a hierarchically porous composite electrode is achieved. When cycled in the range from 2.8 to 4.0 V vs. lithium, the composite electrode exhibits remarkable cyclability and rate performance at different current densities. Footprint area capacities of 1.72 mAh cm^{-2} at 0.1 mA cm^{-2} and 1.1 mAh cm^{-2} at 6 mA cm^{-2} have been achieved for many cycles with significant coulombic efficiency.

Emulsion-templated carbon foams as reducing agents for preparing mixed valence oxides

The synthesis of mixed valence and over-stoichiometric niobium dioxide nanoparticles has been achieved by partial and *in situ* reduction of amorphous niobium pentoxide and molybdenum trioxide nanoparticles inside the carbon foam substrates. The carbon foam provides both mechanical support and reducing environment for converting the niobium pentoxide to dioxide nanoparticles. Such monolithic and freestanding three-dimensionally (3D) architected electrodes are candidates for potential application in lithium-ion microbatteries. The bicontinuous and interpenetrating electronic and ionic conduction pathways present in such electrode structures allow for high rate cycling of the active materials. It is also known that NbO_2 nanoparticles provide higher gravimetric capacity as compared to micro-sized NbO_2 , similar to rutile TiO_2 . Additionally, the presence of Nb^{V} increases the amount of charge stored in the nanoparticles. Electrochemically-driven charge transfer enhancement has been observed using galvanostatic, voltammetric and impedance analysis. Based on *ex situ* XRD, the crystal structure of the niobium oxides remain unaltered during the first cycle. Thus, non-stoichiometric NbO_2 nanoparticles can be used for power applications in lithium microbatteries. The synthesis of $\text{Mo}_3\text{Nb}_2\text{O}_{11}$ nanoparticles on the carbon foams was achieved by combining sol-gel methodology with carbothermal reduction at 750°C . The electrodes were cycled at high rate current densities and can be potentially used for high power applications in 3D microbatteries. In addition, reported approach can be transferable

to the synthesis of other molybdenum, niobium and vanadium containing oxides that are commonly applied in oxidative synthesis of organic molecules.

Water-based exfoliation-deposition of vanadium oxides: A promising strategy for coating carbon substrates

In the last part of the thesis, the synthesis of hydrated vanadium pentoxide nanosheets through water-based exfoliation process and their use in lithium batteries is explored. The synthesis procedure involved refluxing $\text{VO}_2(\text{B})$ in water over several days at various temperatures. Characterizations using X-ray diffraction show that water intercalation plays the most significant role in the transformation of $\text{VO}_2(\text{B})$ to $\text{V}_2\text{O}_{5-8} \cdot n\text{H}_2\text{O}$ nanosheets. The resulting colloidal solution can be cast into a freestanding oxide film, which can be used in a variety of applications. We exploited this simple synthesis strategy to fabricate free-standing and binder-free electrodes for use in lithium battery applications. Composite electrodes consisting of different oxide film thickness were prepared by depositing pre-determined amounts of the colloidal solution on disks of multi-walled carbon nanotube papers. The electrochemical performance of the electrodes is heavily dependent on the thickness of the oxide coatings. The electrode which is 4 μm in thick exhibits similar cyclic performance as V_2O_5 xerogels, whereas the thickest electrode (about 45 μm) behaves to a certain extent like bulk V_2O_5 -based electrodes. In brief, the thinner the coating the better the electrochemical performance. The synthesis strategy can be extended to other types of transition metal oxides or dichalcogenides, which can further be employed to coat carbon foams and design 3D electrodes for lithium microbatteries. Further investigation is sought in order to decrease the thickness of oxide films that can be obtained based on the exfoliation-deposition approach of oxides.

In brief, the research endeavors made in the course of the PhD study have led to the following important milestones:

- the use of emulsion-templated carbon foams for microbattery applications in lieu of commercial carbon foams
- understanding the chemical processes that underpin the increased thermal stability of sulfonated polymers
- optimization of the pore size distributions, specific surface areas, and surface chemistry of the carbon foams
- implementing sol-gel methodology to deposit redox-active materials on highly porous emulsion-templated carbon foams
- the synthesis and application of graphitic carbon foams with optimum void-sizes as freestanding anodes for microbatteries
- identifying exfoliation-deposition as a strategy for coating carbon substrates in oxide nanosheets

Capitalizing on some of these achievements, ongoing research is aimed at producing fully graphitized carbon foams. Preliminary results have proved that graphitic carbon foams with macropores below 4 μm can be prepared via catalytic graphitization. Such materials cannot be obtained by means of traditional synthetic approaches used to fabricate carbon foams. Studies are underway in order to investigate the electrochemical performance of the graphitized carbon foams.

9. Sammanfattning på Svenska

Sedan upptäckten på 1980-talet har litiumjonbatterier utvecklas till det ledande energilagringssystemet i många applikationer innefattande allt ifrån bärbar elektronik till bilar. Ett litiumjonbatteri består av en negativ elektrod, en positiv elektrod och en separator indränkt med en elektrolyt. I elektrolyten rör sig litiumjonerna mellan de två elektroderna när en ström appliceras i den yttre elektriska kretsen. Eftersom litiumjonerna rör sig fram och tillbaka mellan de två elektroderna kallas litiumjonbatterier ofta för "gungstolsbatterier." Som en följd av det ökande intresset för miniatyriseringen av elektroniska apparater finns det idag ett akut behov av små batterier som kan passa i utrymmen av 1 till 5 mm³. Applikationer såsom sensorer, trådlös kommunikation, pacemakers, hörapparater och andra medicinska hjälpmedel kräver ofta batterier med både hög energi- och effekttäthet som kan integreras med enheterna. Hittills har man använt antingen tunn- eller tjockfilms-mikrobatterier, men den plana elektrodkonfigurationen som dessa bygger på är inte kompatibel med både höga energi- och effekttätheter. I ett försök att nå höga energi- och effekttätheter har en övergång till tredimensionella batterier föreslagits. *Figur 9.1* visar några av de elektrodkonfigurationer som skulle kunna användas i 3D-mikrobatterier. En vanlig typ av elektroder som kan användas i 3D-mikrobatterier bygger på användandet av porösa kolmaterial. Deras användning i 3D-batterier har därför rönt ett stort intresse under senare år. Detta beror delvis på kolmaterialens gynnsamma egenskaper när det gäller elektrisk ledningsförmåga, användbarhet, tillgänglighet, kostnad och vikt. Olika typer av kolglasskum och tredimensionella makroporösa (3DOM) kolmaterial har t.ex. använts som 3D-substrat för elektroder för olika mikrobatterier.

Denna avhandling beskriver tillämpningar av en ny typ av kolskum som kan framställas via en enkel syntesmetod och som skulle kunna vara lämplig för massproduktion. Syntesen av kolskummet börjar med beredningen av styrenbaserade hög-inre-fas-emulsion (HIFE) polymerer som har formen av ett mycket poröst nätverk. På grund av deras tendens att förflyktigas vid förhöjda temperaturer, kan styrenbaserade polyHIFEer inte förkolnas utan föregående kemisk modifiering. En sulfonering utförs därför vanligen för att introducera potentiella grupper (t.ex. $-\text{SO}_3\text{H}$) som kan ge tvärbindingar under den efterföljande pyrolysen. I detta arbete har en rad tekniker använts för att studera de kemiska omvandlingar som sulfonsyragrupperna undergår vid olika temperaturer. Termogravimetrisk och spektroskopisk analys indikerar att tioeter ($-\text{C}-\text{S}-$) grupper tvärbinder materialet på bekostnad av sulfonsyragrupperna under värmebehandlingen. Som en följd av ökningen i tvärbindningsgraden

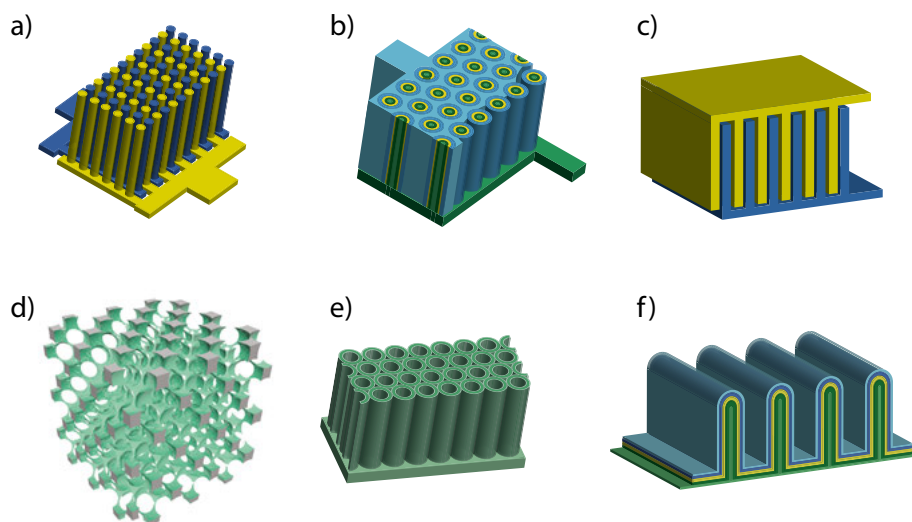


Figure 9.1. Elektrodkonfigurationer so har föreslagits för användning i 3D-mikrobatterier: a) parallella nanostavar b) ett koncentriskt cylinderarrangemang c) parallella nanoark d) en porös svampstruktur e) fristaande nanotuber och f) en veckad nanostruktur

förbättras den termiska stabiliteten, vilket får den sulfonerade polymeren att undergå pyrolys vid högre temperaturer och med mycket mindre kolförluster jämfört med för den ursprungliga polymeren. Följaktligen kan ett kolskum med ett stabilt nätverk framställas från sulfonerade polyHIFEer. Enligt XPS och masspektrometrimätningar har kolskummet en oxiderad yta och materialet innehåller också rester av svavel även efter värmebehandlingar vid så höga temperaturer som 1200 °C.

Ansträngningar har gjorts för att optimera porstorleken, specifika ytareor, och ytkemin för olika kolskum. Den erhållna resultaten indikerar att porenas dimensioner är starkt korrelerad till den omrörningshastighet som används vid framställning av HIFE prekursorerna. Genom att utnyttja de reologiska egenskaperna hos HIFerna ges en unik möjlighet att optimera dimensionerna hos hålrummer. Genom att variera rotationshastigheten från 500 till 2000 rpm, observerades det att porstorleksfördelningen blev mindre, med medelporsstorlekar från 24 till 3,3 μm . När kolskum används som fristående anoder är det önskvärt att minimera för att minska den döda volymen som upptas av elektrolyten. Detta arbete visar att porerna i kolskum kan minskas ytterligare om högre varvtal kan användas vid beredningen av HIFE. Dessutom observerades det att en ökad pyrolystemperatur leder till en minskande specifika ytareal och en högre grad av grafitisering. Dessa egenskaper är gynnsamma för att lagra litiumjoner med en förbättrad cykelstabilitet. Den BET specifika ytan minskade från 525 till 11 $\text{m}^2 \text{g}^{-1}$ när pyrolystemperaturen ökades från 1000 till 2200 °C.

Ett viktigt steg i detta projekt är tillverkningen av 3D-mikroelektroder där man använder kolskummet som (a) ett aktivt anodmaterial i litiumjonbatterier eller (b) en 3D-strömtillledare för andra elektroaktiva material. Typiskt för oordnade kolmaterial är att de förbrukar betydande mängden litiumjoner under den första uppladdningen på grund av parasitiska reaktioner ledande till bildningen av ett passivt ytskikt (ett s.k. SEI-skikt). Denna effekt skulle allvarligt begränsa användningen av kolskum som anodmaterial i mikro-batterier om man inte använder en förnying för att minska den initiala kapacitetsförlusten. Trots bildningen av SEI-skiktet kan en hög grad av reversibilitet och hög laddningseffektivitet uppnås under de efterföljande cyklerna. En stabil kapacitet på 3.5 mA h cm^{-2} erhöles under mer än 50 cykler, vilket mycket väl kan jämföras med resultat från andra studier. Kolskummet som framställdes vid 2200°C har visat bräddre elektrokemiska prestanda, såsom högre coulombisk effektivitet, cyklestabilitet och mindre kapacitetsförlust på första cykeln i jämförelse med de kolskum som tillverkades vid lägre pyrolystemperaturer. De prestanda för detta kolskum visas i *Figur 9.2*. För att demonstrera möj-

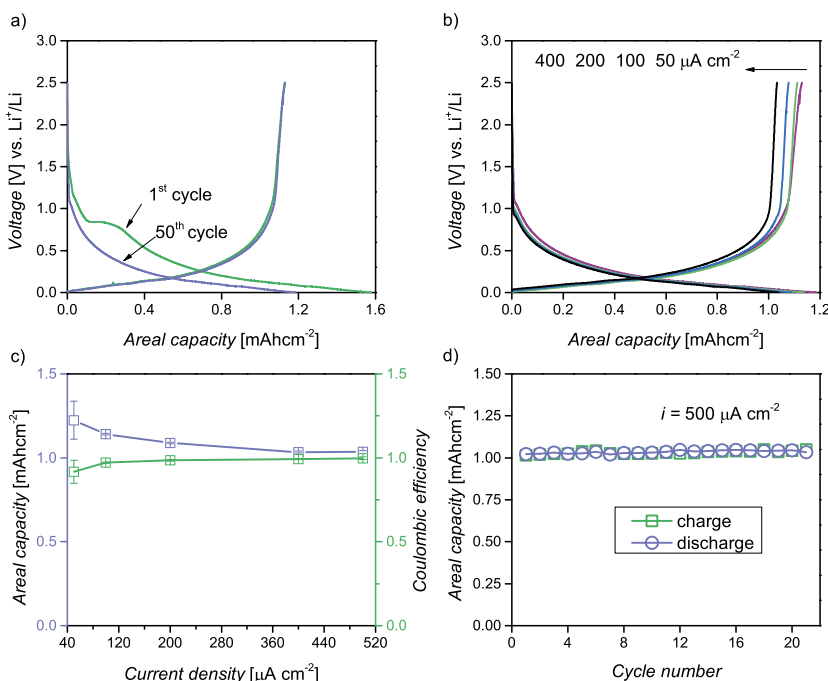


Figure 9.2. Kolskum framställt vid 2200°C som har karakteriserats med hjälp av kontrollerad strömcykling vid olika strömtätheter. a) Den första urladdningen visar en tydlig plåtå på cirka 0.84 V vs. Li^+/Li som kan tillskrivas elektrolytnedbrytning. b) upp- och urladdningsskurvor för de angivna strömtätheterna. c) ytkapaciteter och coulombisk effektivitet som funktion av strömtätheter. d) cyklingsstabilitet under 20 cykler för en strömtäthet av $500 \mu\text{A cm}^{-2}$

ligheten att använda kolskummet som en strömtilliedare för andra aktiva material, har tunna lager av polyanilin (PANI) och LiFePO_4 deponerats med hjälp av elektrodeponering och en sol-gel-metod. Med ett polyanilinbeklätt kolskum som katodmaterial kunde en areabaserad kapacitet på $500 \mu\text{Ah cm}^{-2}$ och bra cyklingshastigheter uppnås. Kapaciteten var också stabil under mer än 90 cykler varför man kan konstatera att dessa kolskums substrat också lämpar sig bra som tredimensionella strömtilliedare i litiumjonbatterier. LiFePO_4 belagda kolskum har också studeras i detalj med avseende på användning i 3D-mikrobatterisammanhang. Elektronmikroskopiska och elektrokemiska karakteriseringar har avslöjat att man får ett poröst hierarkiskt kompositelektrodmaterial som kan cyklas i intervallet mellan 2.8 och 4.0 V mot Li^+/Li och som uppvisar en hög kapacitet och bra upp- och urladdningsprestanda vid olika strömtätheter. Elektroden uppvisade en ytbaserad kapacitet av 1.72 mAh cm^{-2} vid en strömtäthet av 0.1 mA cm^{-2} under många cykler liksom en hög laddningseffektivitet.

Det är också värt att nämna att den ovan beskrivna syntesen av kolskum från polyHIFEer är mycket attraktivt av två huvudsakliga skäl. För det första är metoden enkel och relativt billig vilket gör den lämplig för uppskalning. För det andra så kan ytarean och porositeten hos kolskummet finjusteras antingen genom att man varierar de reagens som används i syntesen eller genom att man ändrar de experimentella förhållandena i övrigt. På detta sätt kan kolskum med olika ytareor och porositet produceras. Emulsionsbaserade kolskum kan också användas i stället för tredimensionella makroporösa material (3DOMs) vars syntes är relativt komplicerad. I syntesen av polymerer med hjälp av vatten-i-olja emulsioner använder man vattendroppar som "mallar" vilket gör processen mer miljövänlig. Det kommande arbetet inom detta forskningsprojekt kommer att inriktas på att (1) Öka mängden av det elektroaktiva materialet på kolskummen för att förbättra den volymsbaserade kapaciteten för dessa 3D-elektroder (2) öka kolskummens elektriska ledningsförmåga och strukturella enhetlighet och (3) minska dödvolymererna i kolmaterialen och optimera deras porstorleksfördelningar.

10. Appendix: Characterization techniques

This chapter provides brief descriptions of a range of techniques employed to characterize the polymer precursors, carbon foams and 3D electrodes.

10.1 Thermal analysis

Thermogravimetry has been widely used to study the kinetics of the decomposition of solids. Various kinetic models are used to fit the TG data to extract important kinetic parameters. The kinetic analyses often assume that decomposition is predominantly dependent on the temperature and the extent of conversion, α . Generally, kinetic models are represented by

$$\frac{d\alpha}{dt} = Z \exp\left(-\frac{E_a}{RT}\right) f(\alpha) \quad (10.1)$$

The parameters Z and E_a in the Arrhenius equation stand for the frequency factor and the activation energy of decomposition, respectively. The function $f(\alpha)$ defines the reaction model used to parameterize the dependence of the kinetics on the extent of conversion [272]. If a first-order reaction is assumed [194], Kissinger's equation is given as

$$\ln\left(\frac{\beta}{T_m^2}\right) = \ln\left(\frac{ZR}{E_a}\right) - \frac{E_a}{R} \frac{1}{T_m} \quad (10.2)$$

where T_m is the temperature corresponding to the maximum of the peaks of the second-derivatives of conversion extents.

A model-free approach, known as Modulated TGA, enables one to determine kinetic parameters from a single TG run [273]. This method makes use of oscillatory temperature program superimposed on a constant heating rate. The modulated TGA expression is given as

$$E_a = \frac{R(T^2 - T_a^2)}{2T_a} \quad (10.3)$$

where T and A are average temperature and temperature amplitude, respectively. And, L is expressed as

$$L = \ln\left(\frac{d\alpha_{c,1}}{d\alpha_{c,2}}\right) \quad (10.4)$$

and represents L the full amplitude of the logarithmic function of the rate of conversion. The respective rates of conversion corresponding to T_1 and T_2 are given as $d\alpha_{c,1}$ and $d\alpha_{c,2}$.

10.2 Residual gas analysis: pyrolysis-mass spectrometry

During pyrolysis, a solid material is heated in a vacuum or inert atmosphere to initiate thermal breakdown of larger molecules into smaller fragments. If the pyrolysis chamber (usually quartz and alumina tube furnaces) is interfaced to an analytical instrument like gas chromatograph, IR spectrometer or mass spectrometer, these fragments can be analysed to quantify, identify or elucidate the structure of the original material [274]. In a typical pyrolysis-mass spectrometer set-up, a residual gas analyser (RGA) is introduced into an ultrahigh vacuum chamber into which the pyrolysis products escape from the furnace. At the ion source, the evolved gasses are ionized when subjected to bombardment by electrons discharged from a heated filament. The molecular ions thus produced will be accelerated onto the mass spectrometer which makes use of four cylindrical electrodes (quadrupoles) to separate the ions by mass. Then, the separated ions impinge on a Faraday cup which generates electric currents proportional to the mass or partial pressure of the residual gasses. Mostly, the signal is given in the form of a plot of intensity or partial pressure as a function of mass-to-charge ratio. A schematic of the integral parts of a typical pyrolysis-mass spectrometer setup is shown in *Figure 10.1*.

In Paper I, RGA (Residual Gas Analysis) was performed to identify the volatile products formed during thermal decomposition of sulfonated poly-HIPE. A sample of about 0.5 mg was placed in a stainless steel sample holder and was heated linearly ($\sim 2.5\text{ }^{\circ}\text{C min}^{-1}$) up to $900\text{ }^{\circ}\text{C}$ under high vacuum ($\sim 10\text{ }\mu\text{Pa}$); the temperatures in the furnace and at the sample site were measured as well as the pressure. A Microvision plus residual gas analyser/mass spectrometer was used to identify the residual gases.

10.3 Electron microscopy

10.3.1 Scanning Electron Microscopy (SEM)

In SEM analysis, a very fine electron beam is scanned across a given specimen in order to obtain topographical and compositional information. Consequent to the interaction between a sharply focused electron beam and a micro-volume of the sample, a wide range of signals is produced: secondary electrons, back-scattered electrons, characteristic X-rays and other photons of varying energies. These signals originate from the elastic scattering (BSE), inelastic scattering of the beam electrons giving rise to ejection of valence electrons from the sample (SE) and X-rays related the removal of core shell electrons. By collecting these signals with different detectors the desired information about the sample can be obtained: topography (SE) and elemental composition (BSE and X-rays).

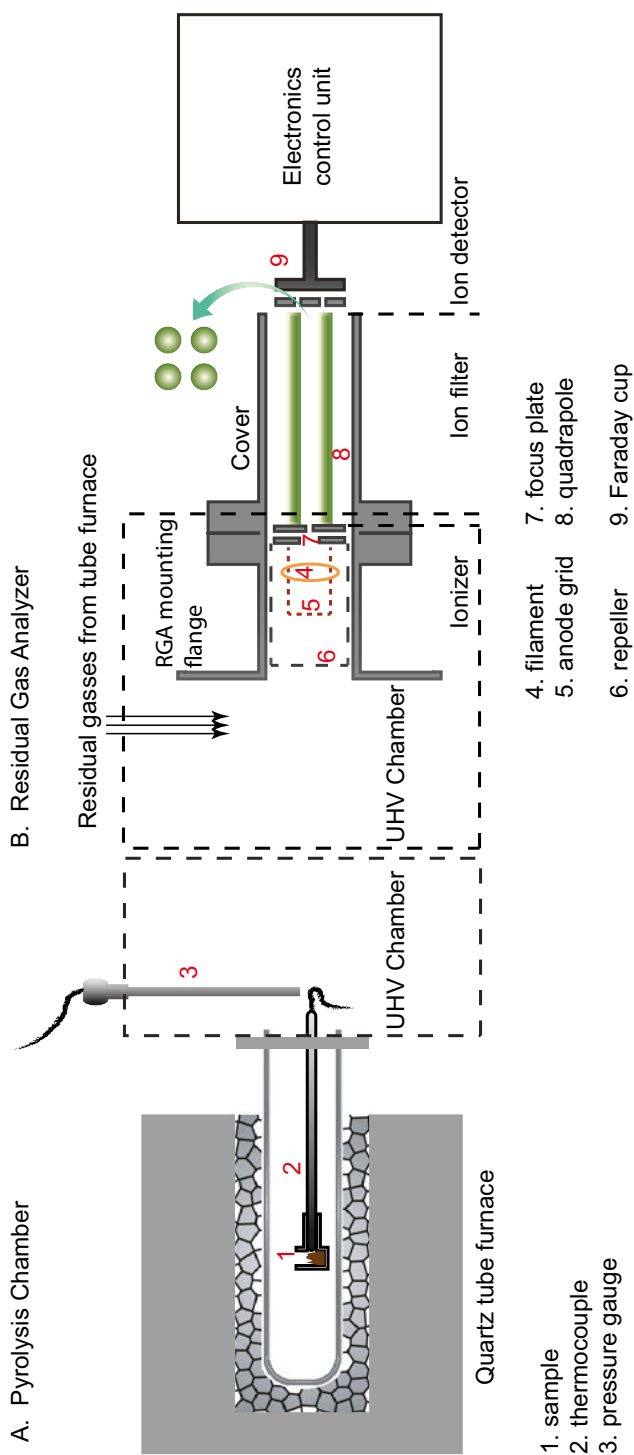


Figure 10.1. The schematic diagram represents a simplified representation of (A) a quartz tube furnace in which a sample of sulfonated polyHIPE is pyrolyzed under vacuum (B) a small quadrupoles mass spectrometer used for detecting residual gases escaping from the pyrolysis chamber.

In Paper **I**, **II** and **III**, thin pieces of the pristine, sulfonated and carbonized polyHIPEs were investigated using SEM of Zeiss Merlin make and equipped with AZtec EDS/EBSD detectors and a BSE detector. A charge compensation utility of the equipment was employed while analyzing the pristine and sulfonated polymers. Analyses of the specimens were carried out at different electron beam energies depending on the information desired from the SEM images. In Paper **IV**, samples of the bare and coated (in polyaniline and LiFePO₄) carbon foams were analyzed by collecting secondary electrons and characteristic x-rays generated as a result of the inelastic scattering of the beam electrons. Scanning electron micrographs of the external and cross-section of coated carbon electrodes were taken using SEM/EDS, Åi Zeiss 1550 instrument (10-15 kV) was used.

10.3.2 Transmission Electron Microscopy (TEM)

TEM exploits the very small wavelength of high energy electrons to probe materials at the atomic scale. In STEM mode, images are formed by collecting electrons scattered incoherently and at high angles with annular dark-field detector. Since elements have different scattering cross-sections, an STEM image exhibits element-specific contrast, i.e., it is sensitive to variations in the atomic number of the atoms present in the specimen.

In Paper **I** to **V**, transmission electron microscopy analysis (TEM and STEM) of finely powdered sample, which were dispersed in acetone and sonicated for several minutes, was done using a JEOL JEM-2100F micro-scope operated at 200 kV and equipped with a Gatan Ultrascan 1000 CCD camera and JEOL annular dark-field (ADF) detector.

10.4 Specific surface area and porosity analysis

Any given porous material can be characterized by its specific surface areas and pore size distribution. These parameters are essential as they determine the properties and performance of the material. Gas physisorption is the most accessible technique employed to investigate porous materials. Particularly, nitrogen adsorption has become the most universally used method for assessing specific surface areas and porosity of powders and porous materials [275]. Physical adsorption refers to the adhering of gas molecules on the surface of a solid material assisted by van der Waals interactions. These weak adsorbate-adsorbent interactions are only measurable at low temperatures; thus, surface area and porosity analysis by N₂-gas adsorption measurements are always carried out in a bath of liquid nitrogen. The amount of gas (adsorbate) that is adsorbed, n_a , on the surface of a solid (adsorbent) material of mass m_s depends on the temperature, applied pressure, and the strength of the gas-solid interactions involved. For an adsorbate below the saturation pressure (p^0) of the gas

and at a constant bath temperature (T), the following relation represents the adsorption isotherm

$$\frac{n_a}{m_s} = f\left(\frac{p}{p^o}\right) T \quad (10.5)$$

After a complete analysis of the adsorption and desorption process at various applied or relative pressures, a graphical representation of the adsorption isotherm is obtained, which is the plot of the amount of adsorbed gas as a function of the respective equilibrium pressure or relative pressure. The evaluation of surface area and pores is conducted with the help of various models like BET (Brunauer-Emmett-Teller), Langmuir, t-plot, BJH (Barrett-Joyner-Halenda) and DFT. The Langmuir model is the simplest isotherm which is premised on the assumptions that only a monolayer coverage of adsorbate occurs on the surface of perfectly flat adsorbent. Since physisorption is not site-specific or selective, the real scenario entails the formation multi-layers of adsorbates beyond the monolayer. The simplest isotherm theory which accounts for multi-layer adsorption is described by the BET relation. The BET relation is the most widely used model on occasion of its simplicity. In its popular form, it is usually written as

$$\frac{p}{n(p^o - p)} = \frac{1}{n_m C_{BET}} + \frac{C_{BET} - 1}{n_m C_{BET}} \frac{p}{p^o} \quad (10.6)$$

where n refers to the amount of gas adsorbed at any given relative pressure (p/p^o) and n_m represents the monolayer coverage. Within a limited region of the isotherm, usually in the p/p^o range of 0.05 to 0.3, a plot of an experimental data in the form of $p/[n(p^o - p)]$ versus p/p^o yields a straight line whose intercept and slope can be used to extract the amount of adsorbate corresponding to monolayer coverage (n_m) and the C constant. Then, the specific BET surface area can be evaluated using the relation below

$$a(BET) = n_m N_A \sigma \quad (10.7)$$

where N_A and σ stand for the Avogadro constant and the average cross-sectional area of an N_2 molecule, respectively.

Beyond quantitative analysis, the shapes and hysteresis loops (if there are any) of the adsorption isotherms provide extensive information respecting the type of pores (shape and width) and the nature of the gas-solid interactions. On IUPAC recommendation, the most common isotherms are classified into six categories, which can be found in various literature [276, 277]. Depending on their widths, pores are classified as macropores (> 50 nm), mesopores (50 to 2 nm), and micropores (< 2 nm). Assessment of pore size distributions from experimental isotherms necessitates the use of various computational models. For mesoporous materials the BJH method, which is based on the Kelvin equation for capillary condensation, is most widely used to generate pore size

distributions from the respective isotherms. The pore-filling phenomena in microporous materials is used to assess microporosity with the help of methods such as DR (Dubinin-Radushkevich) and HK (Horvath-Kawazoe). With the right kernels available, DFT-based methods can be used to evaluate the entire range of pore size distributions from physisorption isotherms. For pore sizes beyond 100 nm, the gas adsorption method is not applicable, and usually liquid (mercury, for example) intrusion porosimetry must be used to evaluate the pore size distributions.

In Paper **I** to **III**, assessments of the porosity and BET specific surface areas of samples of the polymers and carbon foams were conducted based on nitrogen gas sorption analysis at 77 K using a Micromeritics ASAP 2020. All samples (0.2 to 0.3 g) were degassed under vacuum at different temperatures for 12 hours prior to the actual analyses. The equipment used for all measurements is capable of collecting data points above 1.7 nm. Indirect information on microporosity in the samples was obtained from the t-plot method.

10.5 X-ray diffraction

X-ray diffraction is widely used to elucidate the structure of crystalline materials. When a radiation encounters periodically-arranged array of atoms or molecules with interatomic spacing comparable to or larger than its wavelength, an elastic and coherent scattering occurs, giving rise to discrete diffraction patterns. Constructive interferences between the scattered rays occur when the Bragg relation given below is obeyed.

$$n\lambda = 2d\sin\theta \quad (10.8)$$

In **Papers II** to **VII**, powders of the carbon foams (pristine or coated) synthesized at different temperatures were dispersed in ethanol and the drops of the dispersion were scattered on a Si-substrate sample holder. Diffraction patterns were collected using a copper K α radiation source ($\lambda = 1.5418 \text{ \AA}$) on powder diffractometer (Siemens D5000 and Bruker D8 TwinTwin).

10.6 X-ray spectroscopy

10.6.1 X-ray photoelectron emission spectroscopy

X-ray photoelectron spectroscopy is one of the most prominent surface characterization techniques that are used to determine surface composition, local chemical environments, oxidation states of elements, and valence band electronic structures of materials. The working principle of XPS borrows from the photoelectric effect which states that photoelectrons are emitted when a light of certain threshold frequency impinges on metal surfaces. In XPS measurements, a monochromatic X-ray of known wavelength is illuminated on a

sample resulting in the ejection of inner core electrons. Typically, the emitted photoelectrons are collected by the hemispherical detector which measures their kinetic energies. The binding energies of the photoelectrons are calculated as

$$E_b = h\nu - E_k - \Phi_{\text{spec}} \quad (10.9)$$

and used to identify the elements present in the sample. A schematic illustration is given in *Figure 10.2*. An XPS spectrum displays a plot of intensity as a function of binding energies.

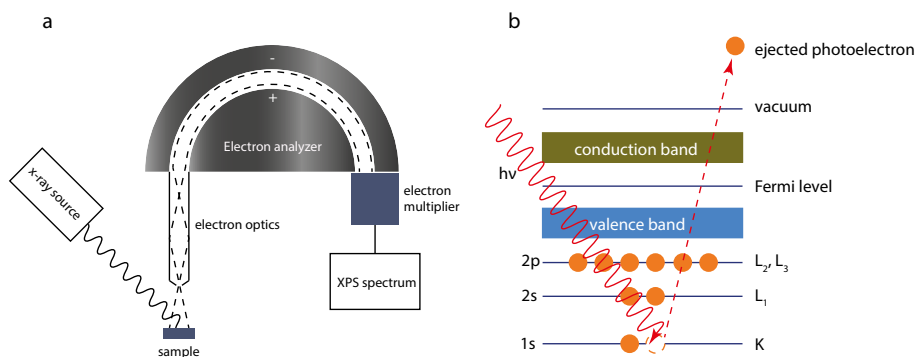


Figure 10.2. Schematic illustration of (a) the components of X-ray photoelectron spectrometer (b) the working principle that underpins XPS are shown.

Analysis of polyHIPE polymers after sulfonation and treatments at various temperatures: XPS analyses were performed on a series of samples of untreated, sulfonated and thermally cured polyHIPE polymers (Paper I). The XPS measurements were performed on a commercial PHI 5500 spectrometer, using monochromatic Al K α radiation (1487 eV) and an electron emission angle of 45°. Cycled carbon foams (Paper II and IV) are washed with dimethyl carbonate (DMC) in an argon-filled glove box prior to XPS measurements. The electrodes were transferred from the glove box to the XPS analysis chamber using a custom-made airtight transfer shuttle to avoid any contamination from air. All the XPS spectra were energy-calibrated by the hydrocarbon peak positioned at the binding energy of 285.0 eV.

10.6.2 X-ray absorption near edge structure spectroscopy

In XANES the photon energy is scanned over a broad range of wavelengths and the intensity of the absorbed X-ray or the fluorescence intensity of the emitted photons is recorded as a function of the photon energy. Absorption edges are observed in a XANES spectrum due to a discontinuous increase in photon absorption occurring when the excitation X-ray energy is sufficient to dislodge the core shell electrons of a given sample. As the absorption edges

are element-specific and depend on the fine structure of the sample, XANES spectrum can be used to fingerprint different phases and identify oxidation states.

The XANES measurements in Paper **I** were performed at the HIKE end-station positioned at the KMC-1 beam line of the synchrotron facility BESSY II operated by the Helmholtz-Zentrum Berlin, Germany. The spectra were recorded at the S K α 1 edge (2.309 keV) within the energy range of 2450 eV and 2550 eV in a fluorescence yield (FY) mode using a BrukerX-Flash 4010 fluorescence detector. In Paper **VI**, the vanadium K-edge XANES measurements were conducted at beamline I811, MAXIV-lab. Typically four scans were collected for each sample and the averaged spectrum was used. All the spectra were energy-calibrated to vanadium metal foil assigning the first inflection point on the edge to 5465.2 eV.

10.7 Vibrational spectroscopy

10.7.1 Fourier transform infrared spectroscopy

Infrared spectroscopy is concerned with the identification and quantification of functional groups and deals with the IR region of the electromagnetic spectrum. As a rule, the mid-ir region which extends from 4000 to 400 cm⁻¹ of energy is used to characterize the vibrational modes of functional groups and to study the roto-vibrational structure associated with the bonds in consideration [185]. Infrared energy absorption is commonly associated with molecules (bonds) in which the electric dipole moment changes as a result of vibrational transitions. By definition, symmetrical molecules are naturally IR inactive as they vibrate without the dipole moment being transitioned. Associated with every molecule are distinct vibrational frequencies that are called normal modes, and their overtones. When the energy of the incident radiation matches that of the vibrational modes, a molecule attenuates the energy of the excitation radiation. The intensity of absorbed or transmitted radiation is plotted as a function of frequency or wavelength to give an IR spectrum. Based on the characteristic group frequencies corresponding to different bonds, a given material can be characterized to identify the functional groups it is constituted of.

In Paper **I** and **II**, an ATR- FTIR spectrometer (Perkin Elmer) was used to characterize polyHIPE polymers before and after sulfonation and pyrolysis at various temperatures. A diffuse reflectance IR spectrometer equipped with a special sample holder was used for *in situ* monitoring of the pyrolysis of the sulfonated polymers.

10.7.2 Raman spectroscopy

Due to its enormous sensitivity to highly symmetric covalent bonds (carbon-carbon), Raman spectroscopy is regarded as the standard technique suitable for probing the morphology, structure, bonding and defects in carbon materials. Irradiation of carbon materials using a monochromatic light like laser causes the polarization of C–C bonds to form oscillating dipoles which scatter the radiation at mainly three different frequencies. A schematic of the working principle of Raman spectroscopy is given in *Figure 10.3*. Valuable information

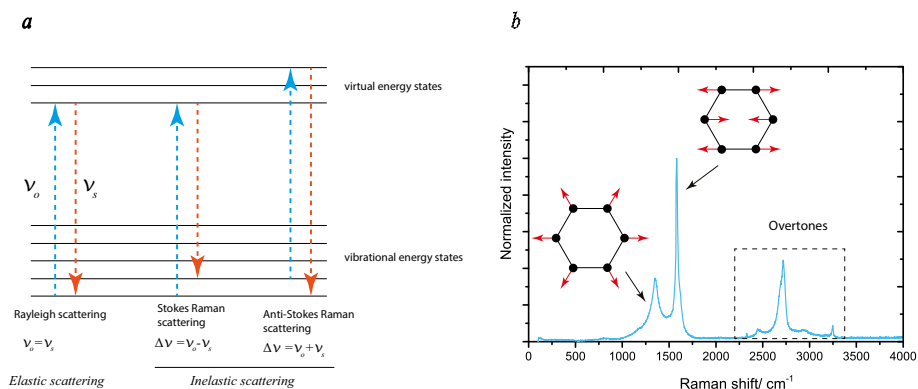


Figure 10.3. Schematic representation of the origin of Raman shift (a) and (b) Raman spectrum of graphite is given alongside the two main vibrational modes of defective graphite.

is garnered from the peak shape, position and width of the Raman bands [200–202, 205]. The Raman spectrum of a highly ordered single crystal of graphite displays a sharp peak (denoted by G) around 1580 to 1600 cm^{-1} assigned to in-plane modes of vibration of E_{2g} symmetry. Disruption of the long-range order, as in polycrystalline graphite and disordered carbon, introduces another peak (D) around 1350 cm^{-1} due to a breathing mode of vibration of A_{1g} symmetry of the six-membered ring. In visible Raman spectrum, the sp² sites in carbons have much higher cross-section of scattering than that of sp³ bonds. Thus, both D and G bands are due to the presence of sp² bonds. Carbons containing sp³ carbons are studied using UV lasers. In addition to the two fundamental vibrations, bands due to overtones are also observed at higher Raman shifts for carbons.

10.8 Electrochemical Methods

10.8.1 Cyclic voltammetry

Cyclic voltammetry is an electrochemical technique that is customarily used to study redox processes occurring within an experimental potential window. In a

CV experiment, the potential of the working electrode is varied at a fixed scan rate and the resultant current is recorded as a function of the potential. [46,278] The potential is swept from the initial value (often the OCV) to the final limit where the direction of the scan is reversed back to the initial (or another) limit. By varying the scan rate, it is possible to diagnose the kinetics and stability of the chemical species being studied. With the help of theoretical considerations crucial parameters can be extracted from voltammograms. Both charge transfer kinetics and mass transport effects can be studied well by manipulating the scan rates. The Randles-Ševčík formulation is the most popular mathematical representation of a CV which relates the magnitude of peak currents (i_p) to the electrode surface (A), the diffusion coefficient (D), the bulk concentration of the redox species (C^b), and the scan rate (v) used in the experiment. Accordingly, the reduction (and oxidation) peak current in a CV can be represented by

$$i_p = (2.69 \times 10^5) n^{3/2} A D_o^{1/2} C_o^b v^{1/2} \quad (10.10)$$

for a Nernstian (reversible) system, and

$$i_p = (2.99 \times 10^5) \alpha^{1/2} A D_o^{1/2} C_o^b v^{1/2} \quad (10.11)$$

for an irreversible system controlled by a one-electron transfer process. The parameters n and α stand for the number of moles of electrons exchanged during the rate-determining step and the transfer coefficient of the electrode reaction. For both reversible and irreversible electrode processes, the peak current is linearly dependent on the square-root of the scan rate. In addition to faradaic reactions, the charging and discharging of the electric double-layer at the electrode-electrolyte interface contribute to the total current measured in a CV experiment. Especially for high surface area electrodes, such as carbon foams, this contribution can be appreciable, and due considerations have to be made if quantitative analysis is sought. Assuming the capacitance (C) of the double-layer is constant, the capacitive current, i_c , is expressed as

$$i_c = C \frac{\partial V}{\partial t} = C v \quad (10.12)$$

which indicates that the current scales linearly with the scan rate. Thus, the peak current in a given CV can be described as the sum of the two contributions. The following general relations are commonly invoked when studying the charge storage mechanisms of pseudocapacitors or batteries.

$$i = a v^b \quad (10.13)$$

or,

$$\log i = \log a + b \log v \quad (10.14)$$

Alternatively, the total current can be expressed as

$$i = i_f + i_c = m v^{1/2} + n v \quad (10.15)$$

or,

$$\frac{i}{v^{1/2}} = m + nv^{1/2} \quad (10.16)$$

The symbols a , b , m , and n are adjustable parameters. Based on equations 10.13 to 10.16, plots of peak currents versus scan rates yield straight lines whose slopes and intercepts can be used to extract valuable information regarding the charge storage mechanism and kinetics of the electrode process in different scan rate regimes. In brief, these relations help decouple the contributions of capacitive processes and faradaic reactions to the total amount of charge passing during a CV experiment.

10.8.2 Controlled-current methods

Galvanostatic cycling with potential limitations is the most predominant electrochemical method used to study the electrochemical behavior, rate capability and cyclability of lithium ion batteries. In this method, a controlled-current is imposed on the electrochemical cell and the potential of the working electrode is recorded as a function of time or charge. Faraday's first law is used to determine the theoretical and the actual specific capacities obtained at different current densities.

$$\frac{nF}{M} = \frac{It}{m} = Q \quad (10.17)$$

where n , F , m , M , I , and t are the number of moles of electrons, the Faraday constant, the actual mass of the active material, the molar mass of the active material, the applied current, and time elapsed to complete the experiment. In addition to specific capacities, an electrode is also characterized by its specific energy and power densities associated with each applied current [45]. The energy density may be expressed as

$$E = \frac{I}{m} \int_0^t V dt = \frac{1}{m} \int_0^Q V(Q) dQ \quad (10.18)$$

while the corresponding power density is given by

$$P = \frac{E}{t} \quad (10.19)$$

In addition, the values of energy and power can be normalized to the volume of the electrode, and expressed as volumetric energy and power densities, respectively. The energy and power densities of various electrochemical systems are usually presented in the form of a chart commonly known as the Ragone plot. Alongside capacity, energy and power densities, it is essential to provide the efficiency of the electrochemical cell in retaining charge over sustained

cycling. The coulombic efficiency (C_{eff}) is generally expressed in terms of the output charge (Q_{output}) and input charge (Q_{input}) as

$$C_{eff} = \frac{Q_{output}}{Q_{input}} \quad (10.20)$$

A coulombic efficiency that deviates substantially from 1.0 may be indicative of parasitic reactions or irreversible structural changes which trap the lithium ions in the active materials. This parameter is particularly essential for full-cell batteries wherein the lithium ions originate from the lithium-containing positive electrode during charging the cell.

10.8.3 Electrochemical impedance spectroscopy

Electrochemical impedance spectroscopy (EIS) is a powerful technique used to probe the dynamics of physicochemical processes that occur in electrochemical systems. During an EIS experiment, an alternating voltage perturbation with an amplitude of V_o is applied to a working electrode at open circuit voltage or around a direct circuit (dc) potential of V_{dc} . [46, 279] The signal can be given as

$$V = V_o \sin(\omega t) \quad (10.21)$$

or

$$V = V_o \exp(j\omega t) \quad (10.22)$$

Varying the perturbation over a range of frequencies (ω) allows for identifying the different physical and chemical processes that influence the performance of a given electrochemical system. The ac excitation voltage causes current to flow through the electrochemical cell. Given, the amplitude of the perturbation is sufficiently small, the instantaneous current response, I , will be at the same sinusoidal frequency, but shifted in phase by (ϕ)

$$I = I_o \sin(\phi + \omega t) = I_o \exp j(\phi + \omega t) \quad (10.23)$$

And the complex impedance (Z^*) will be expressed as

$$Z^* = \frac{V(t)}{I(t)} = \left(\frac{V_o}{I_o} \right) \frac{\exp(j\omega t)}{\exp j(\phi + \omega t)} = Z_o \exp(-j\phi) \quad (10.24)$$

Or equivalently,

$$Z^* = Z_o (\cos\phi - j\sin\phi) = Z_{re} + j(-Z_{im}) \quad (10.25)$$

where Z_{re} , and Z_{im} stand, respectively, for the real and imaginary components of the impedance response. The phase angle, ϕ , may be expressed as

$$\phi = \arctan \left(\frac{Z_{im}}{Z_{re}} \right) = \arctan \frac{1}{\omega RC} \quad (10.26)$$

The phase angle, ϕ , varies from 0 to $\pi/2$ from a purely resistive system to a purely capacitive system, and mixed behaviors in between. The processes occurring within the electrochemical cell can be represented by a network of resistors, capacitors and inductors, to which the collected impedance data can be fitted to extract physically acceptable values for each circuit component. Often, impedance data are presented graphically in *Nyquist* and *Bode* plots as shown in *Figure 10.4*. The plot of $-Z_{\text{im}}$ versus Z_{re} is known as an *Argand diagram* or *Nyquist plot*. In Bode the phase angle and the absolute value of the impedance (s) are plotted as a function of the logarithm of frequency. The

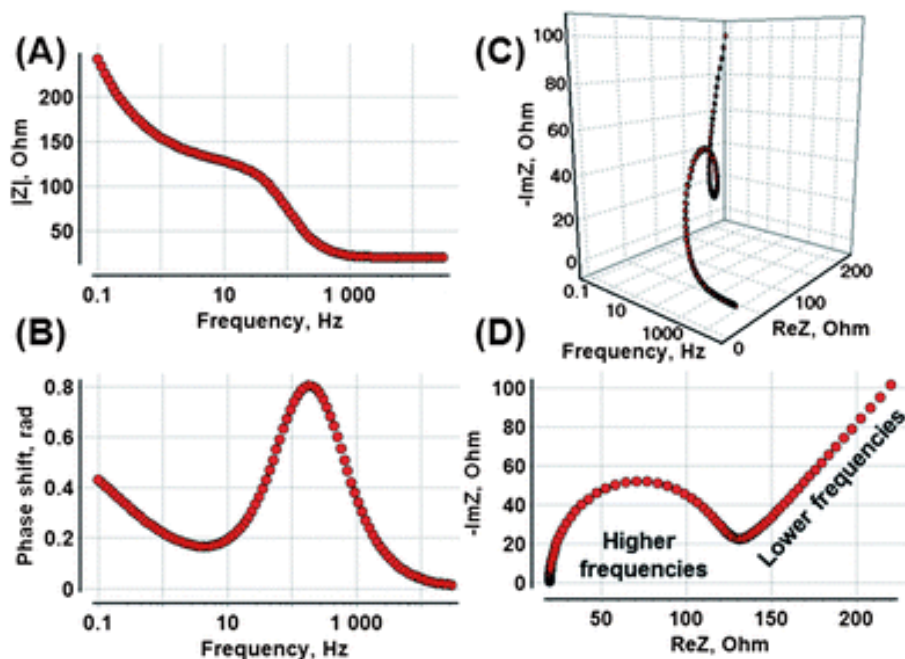


Figure 10.4. Impedance data represented by Bode plots A) and B), 3D plot C) and a Nyquist plot D) Reproduced by from Ref [280] permission of ©2013 The Royal Society of Chemistry

different physicochemical processes within the electrochemical system occur on different time scales and are hence sensed in different frequency regimes during the experiment. A typical example is given in *Figure 10.5* for a lithiated graphite electrode.

10.8.4 Electrode preparation and cell construction

Unless specified, only pouch cells were principally used to prepare the electrochemical half-cells that were investigated in all the projects summarised in this thesis. In Paper II Swagelok® cells were used instead. In all cases, the electrochemical cells were built by assembling the carbon foam (pristine and

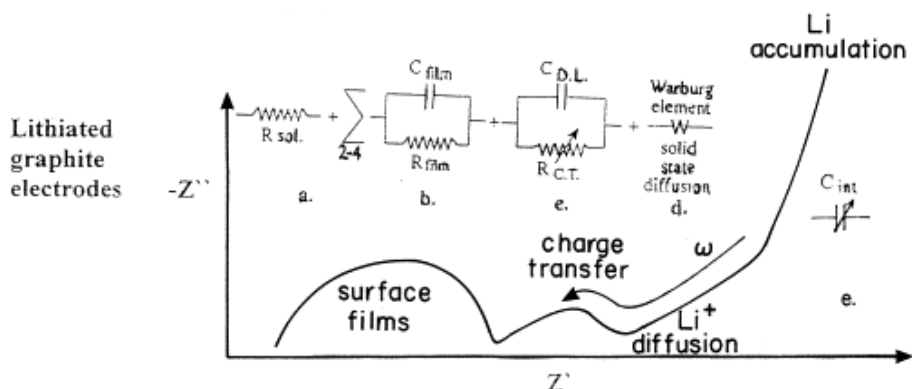


Figure 10.5. A schematic illustration of the equivalent circuit elements, and the typical features observed in the impedance spectra of lithiated graphite electrodes. Adapted from Ref. [281] with permission from ©Elsevier

coated) as working electrodes and lithium foils as counter and reference electrodes. Glass fiber separators soaked in an electrolyte were used in between the two electrodes. A schematic of the half-cells in pouch and Swagelok® configurations is given in Figure 10.6. For electrochemical testing, all electrodes

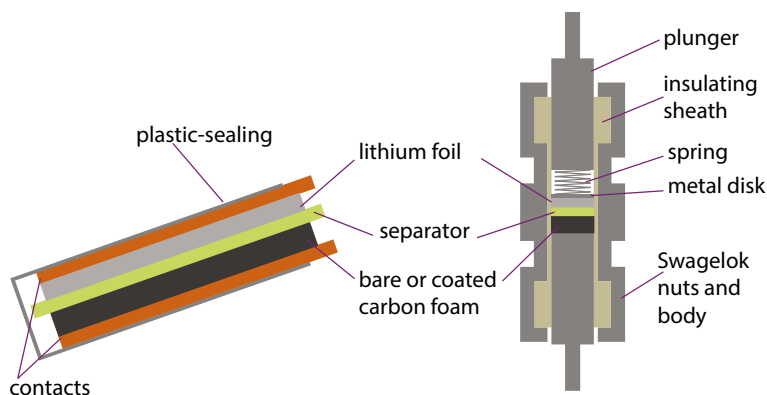


Figure 10.6. Schematic representation of the cross-section view of a pouch cell (a) and a Swagelok® (b).

(pristine or coated carbon foams) were dried under vacuum at 80-120 °C for 12 h before use. Pouch and Swagelok cells were assembled in an argon-filled glove box (MBRAUN labmaster 130) using pristine or coated carbon foams, lithium foil anodes, and glass fiber separators soaked in electrolyte (1 M LiPF₆ in EC/DEC 1:1). In Paper IV, however, the working electrodes were disks of CNT (carbon nanotube) paper clad in hydrated V₂O₅ nanosheets. Cyclic voltammetry and controlled-current techniques were employed to characterize the electrochemical behavior and rate capability of the electrodes using Arbin (Arbin BT2043), Biologic VMP2, and Biologic MPG2. The electrodes

were cycled at different current densities and scan rates in an electrochemical voltage windows wherein the the active materials in consideration reacted reversibly. The capacities at different current densities were normalized to the footprint areas of the electrodes used. Electrochemical impedance data were collected for some of the electrodes using the BioLogic VMP2 and SP240 potentiostats. The electrodes were charged and discharged by stepwise imposition of potential steps between the respective cut-off voltages. After 20 minutes, a sinusoidal signal with amplitude of 10 mV and scan frequencies ranging from 200 kHz to 1 MHz was applied on the polarized electrodes. Detailed descriptions of the experimental procedure and parameters can be found in the respective papers appended to this thesis.

References

- [1] Matthew Roberts, Phil Johns, John Owen, Daniel Brandell, Kristina Edström, Gaber El Enany, Claude Guery, Diana Golodnitsky, Matt Lacey, Cyrille Lecoer, Hadar Mazor, Emanuel Peled, Emilie Perre, Manikoth M. Shaijumon, Patrice Simon, and Pierre-Louis Taberna. 3D lithium ion batteries—from fundamentals to fabrication. *J. Mater. Chem.*, 21(27):9876–9890, 2011.
- [2] Jeffrey W. Long, Bruce Dunn, Debra R. Rolison, and Henry S. White. Three-dimensional battery architectures. *Chem. Rev.*, 104(10):4463–4492, 2004. PMID: 15669159.
- [3] Jos F. M. Oudenhoven, Loïc. Baggetto, and Peter H. L. Notten. All-solid-state lithium-ion microbatteries: A review of various three-dimensional concepts. *Adv. Energy Mater.*, 1(1):10–33, 2011.
- [4] K A Cook-Chennault, N Thambi, and A M Sastry. Powering mems portable devices—a review of non-regenerative and regenerative power supply systems with special emphasis on piezoelectric energy harvesting systems. *Smart Mater. Struct.*, 17(4):043001, 2008.
- [5] Knowmade. Microbattery Patent Landscape Analysis, year = 2016, url = <http://www.i-micronews.com/category-listing/product/microbattery-patent-landscape-analysis.html> description, urldate = 2017-01-05.
- [6] S. Sudevalayam and P. Kulkarni. Energy harvesting sensor nodes: Survey and implications. *IEEE Commun. Surv. Tut.*, 13(3):443–461, 2011.
- [7] S P Beeby, M J Tudor, and N M White. Energy harvesting vibration sources for microsystems applications. *Meas. Sci. Technol.*, 17(12):R175, 2006.
- [8] Shad Roundy, Paul K. Wright, and Jan Rabaey. A study of low level vibrations as a power source for wireless sensor nodes. *Computer Communications*, 26(11):1131–1144, 7 2003.
- [9] J. F. M. Oudenhoven, R. J. M. Vullers, and R. van Schaijk. A review of the present situation and future developments of micro-batteries for wireless autonomous sensor systems. *Int. J. Energy Res.*, 36(12):1139–1150, 2012.
- [10] Thomas B. Reddy and David. Linden. Linden’s handbook of batteries, 2011.
- [11] M. Armand and J. M. Tarascon. Building better batteries. *Nature*, 451(7179):652–657, 02 2008.
- [12] M. Stanley Whittingham and Fred R. Gamble. The lithium intercalates of the transition metal dichalcogenides. *Mater. Res. Bull.*, 10(5):363–371, 1975.
- [13] M. Stanley Whittingham and Arthur H. Thompson. Intercalation and lattice expansion in titanium disulfide. *J. Chem. Phys.*, 62(4):1588–1588, 2017/01/06 1975.
- [14] M. Stanley Whittingham. Chemistry of intercalation compounds: Metal guests in chalcogenide hosts. *Prog. Solid State Chem.*, 12(1):41–99, 1978.
- [15] M. Stanley Whittingham. Electrical energy storage and intercalation chemistry. *Science*, 192(4244):1126–1127, 1976.

- [16] Natasha A. Chernova, Megan Roppolo, Anne C. Dillon, and M. Stanley Whittingham. Layered vanadium and molybdenum oxides: batteries and electrochromics. *J. Mater. Chem.*, 19(17):2526–2552, 2009.
- [17] M. S. Dresselhaus and G. Dresselhaus. Intercalation compounds of graphite. *Adv. Phys.*, 30(2):139–326, 04 1981.
- [18] K. Mizushima, P. C. Jones, P. J. Wiseman, and J. B. Goodenough. Li_xCoO_2 ($0 < x < 1$): A new cathode material for batteries of high energy density. *Mater. Res. Bull.*, 15(6):783–789, 1980.
- [19] Christian Masquelier and Laurence Croguennec. Polyanionic (phosphates, silicates, sulfates) frameworks as electrode materials for rechargeable Li (or Na) batteries. *Chem. Rev.*, 113(8):6552–6591, 08 2013.
- [20] A. K. Padhi, K. S. Nanjundaswamy, and J. B. Goodenough. Phospho-olivines as positive-electrode materials for rechargeable lithium batteries. *J. Electrochem. Soc.*, 144(4):1188–1194, 1997.
- [21] Li-Xia Yuan, Zhao-Hui Wang, Wu-Xing Zhang, Xian-Luo Hu, Ji-Tao Chen, Yun-Hui Huang, and John B. Goodenough. Development and challenges of LiFePO_4 cathode material for lithium-ion batteries. *Energy Environ. Sci.*, 4(2):269–284, 2011.
- [22] A. Nyten, S. Kamali, L. Häggström, T. Gustafsson, and J. O. Thomas. The lithium extraction/insertion mechanism in $\text{Li}_2\text{FeSiO}_4$. *J. Mater. Chem.*, 16(23):2266–2272, 2006.
- [23] N. Recham, J.-N. Chotard, L. Dupont, C. Delacourt, W. Walker, M. Armand, and J.-M. Tarascon. A 3.6 v lithium-based fluorosulphate insertion positive electrode for lithium-ion batteries. *Nat. Mater.*, 9(1):68–74, 01 2010.
- [24] Adam Sobkowiak, Matthew R. Roberts, Reza Younesi, Tore Ericsson, Lennart Häggström, Cheuk-Wai Tai, Anna M. Andersson, Kristina Edström, Torbjörn Gustafsson, and Fredrik Björefors. Understanding and controlling the surface chemistry of LiFeSO_4F for an enhanced cathode functionality. *Chem. Mater.*, 25(15):3020–3029, 08 2013.
- [25] Masataka Wakihara and Osamu *Lithium ion batteries: fundamentals and performance*. John Wiley & Sons, 2008.
- [26] J. O. Besenhard and H. P. Fritz. Cathodic reduction of graphite in organic solutions of alkali and NR_4^+ salts. *J. electroanal. chem. interfacial electrochem.*, 53(2):329–333, 1974.
- [27] R. Yazami and Ph. Touzain. A reversible graphite-lithium negative electrode for electrochemical generators. *J. Power Sources*, 9(3):365–371, 1983.
- [28] Rachid Yazami. Surface chemistry and lithium storage capability of the graphite–lithium electrode. *Electrochim. Acta*, 45(1–2):87–97, 9 1999.
- [29] Z. X. Shu, R. S. McMillan, and J. J. Murray. Electrochemical intercalation of lithium into graphite. *J. Electrochem. Soc.*, 140(4):922–927, 1993.
- [30] E. Peled. The electrochemical behavior of alkali and alkaline earth metals in nonaqueous battery systems—the solid electrolyte interphase model. *J. Electrochem. Soc.*, 126(12):2047–2051, 1979.
- [31] E. Peled, D. Golodnitsky, G. Ardel, and V. Eshkenazy. The SEI model—application to lithium-polymer electrolyte batteries. *Electrochim. Acta*, 40(13):2197–2204, 1995.
- [32] K. M. Colbow, J. R. Dahn, and R. R. Haering. Structure and electrochemistry

- of the spinel oxides LiTi_2O_4 and $\text{Li}_{4/3}\text{Ti}_{5/3}\text{O}_4$. *J. Power Sources*, 26(3):397–402, 1989.
- [33] B. Guo, X. Yu, X.-G. Sun, M. Chi, Z.-A. Qiao, J. Liu, Y.-S. Hu, X.-Q. Yang, J. B. Goodenough, and S. Dai. A long-life lithium-ion battery with a highly porous TiNb_2O_7 anode for large-scale electrical energy storage. *Energy Environ. Sci.*, 7(7):2220–2226, 2014.
- [34] Y. G. Guo, Y. S. Hu, W. Sigle, and J. Maier. Superior electrode performance of nanostructured mesoporous TiO_2 (anatase) through efficient hierarchical mixed conducting networks. *Adv. Mater.*, 19(16):2087–2091, 2007.
- [35] Ryoji Kodama, Yasuko Terada, Izumi Nakai, Shinichi Komaba, and Naoaki Kumagai. Electrochemical and in situ XAFS-XRD investigation of Nb_2O_5 for rechargeable lithium batteries. *J. Electrochem. Soc.*, 153(3):A583–A588, 2006.
- [36] Naoaki Kumagai, Yoshimasa Koishikawa, Shinichi Komaba, and Nobuharu Koshiba. Thermodynamics and kinetics of lithium intercalation into Nb_2O_5 electrodes for a 2 V rechargeable lithium battery. *J. Electrochem. Soc.*, 146(9):3203–3210, 1999.
- [37] J. R. Dahn, Tao Zheng, Yinghu Liu, and J. S. Xue. Mechanisms for lithium insertion in carbonaceous materials. *Science*, 270(5236):590–593, 1995.
- [38] Yinghu Liu, J. S. Xue, Tao Zheng, and J. R. Dahn. Mechanism of lithium insertion in hard carbons prepared by pyrolysis of epoxy resins. *Carbon*, 34(2):193–200, 1996.
- [39] Y. P. Wu, E. Rahm, and R. Holze. Carbon anode materials for lithium ion batteries. *J. Power Sources*, 114(2):228–236, 3 2003.
- [40] Wei-Jun Zhang. A review of the electrochemical performance of alloy anodes for lithium-ion batteries. *J. Power Sources*, 196(1):13–24, 1 2011.
- [41] M. Morcrette, D. Larcher, J. M. Tarascon, K. Edström, J. T. Vaughey, and M. M. Thackeray. Influence of electrode microstructure on the reactivity of Cu_2Sb with lithium. *Electrochim. Acta*, 52(17):5339–5345, 5 2007.
- [42] Dominique Larcher, Shane Beattie, Mathieu Morcrette, Kristina Edstrom, Jean-Claude Jumas, and Jean-Marie Tarascon. Recent findings and prospects in the field of pure metals as negative electrodes for Li-ion batteries. *J. Mater. Chem.*, 17(36):3759–3772, 2007.
- [43] P. Poizot, S. Laruelle, S. Grugeon, L. Dupont, and J-M. Tarascon. Nano-sized transition-metal oxides as negative-electrode materials for lithium-ion batteries. *Nature*, 407(6803):496–499, 09 2000.
- [44] John R. Owen. Rechargeable lithium batteries. *Chem. Soc. Rev.*, 26(4):259–267, 1997.
- [45] John B. Goodenough and Kyu-Sung Park. The Li-ion rechargeable battery: A perspective. *J. Am. Chem. Soc.*, 135(4):1167–1176, 01 2013.
- [46] A.J. Bard and L.R. Faulkner. *Electrochemical Methods: Fundamentals and Applications*. John Wiley & Sons, 2004.
- [47] Todd R. Ferguson and Martin Z. Bazant. Nonequilibrium thermodynamics of porous electrodes. *J. Electrochem. Soc.*, 159(12):A1967–A1985, 2012.
- [48] John Newman and Karen E. Thomas-Alyea. *Electrochemical systems*. John Wiley & Sons, 2012.
- [49] M. Barrande, R. Bouchet, and R. Denoyel. Tortuosity of porous particles. *Analytical Chemistry*, 79(23):9115–9121, 2007.

- [50] Yiling Dai and Venkat Srinivasan. On graded electrode porosity as a design tool for improving the energy density of batteries. *J. Electrochem. Soc.*, 163(3):A406–A416, 2016.
- [51] Bruno Scrosati, KM Abraham, Walter A van Schalkwijk, and Jusef Hassoun. *Lithium batteries: advanced technologies and applications*, volume 58 John Wiley & Sons, 2013.
- [52] Kristina Edström, Daniel Brandell, Torbjörn Gustafsson, and Leif Nyholm. Electrodeposition as a tool for 3d microbattery fabrication. *Electrochem. Soc. Interface*, 20(2):41, 2011.
- [53] Nancy J Dudney et al. Thin film micro-batteries. *Electrochem. Soc. Interface*, 17(3):44, 2008.
- [54] J. B. Bates, N. J. Dudney, B. Neudecker, A. Ueda, and C. D. Evans. Thin-film lithium and lithium-ion batteries. *Solid State Ionics*, 135(1):33–45
- [55] F. Chamran, Hong-Seok Min, B. Dunn, and Chang-Jin Kim. Zinc-air microbattery with electrode array of zinc microposts. In *2007 IEEE 20th International Conference on Micro Electro Mechanical Systems (MEMS)*, pages 871–874, Jan 2007.
- [56] S. K. Cheah, E. Perre, M. Rooth, M. Fondell, A. Hårsta, L. Nyholm, M. Boman, T. Gustafsson, J. Lu, P. Simon, and K. Edström. Self-supported three-dimensional nanoelectrodes for microbattery applications. *Nano Lett.*, 9(9):3230–3233, 2009.
- [57] W. Wei, G. Oltean, C.-W. Tai, K. Edstrom, Fredrik B., and Leif Nyholm. High energy and power density TiO₂ nanotube electrodes for 3D Li-ion microbatteries. *J. Mater. Chem. A*, 1(28):8160–8169, 2013.
- [58] D. Golodnitsky, M. Nathan, V. Yufit, E. Strauss, K. Freedman, L. Burstein, A. Gladkich, and E. Peled. Progress in three-dimensional (3D) li-ion microbatteries. *Solid State Ionics*, 177(26, Åi32):2811 – 2819, 2006.
- [59] M. M. Shaijumon, E. Perre, B. Daffos, P.-L. Taberna, J.-M. Tarascon, and P. Simon. Nanoarchitected 3D cathodes for li-ion microbatteries. *Adv. Mater.*, 22(44):4978–4981, 2010.
- [60] E. Perre, L. Nyholm, T. Gustafsson, P.-L. Taberna, P. Simon, and K. Edström. Direct electrodeposition of aluminium nano-rods. *Electrochem. Commun.*, 10(10):1467–1470, 10 2008.
- [61] Chunlei Wang, Lili Taherabadi, Guangyao Jia, Marc Madou, Yuting Yeh, and Bruce Dunn. C-MEMS for the manufacture of 3D microbatteries. *Electrochem. Solid State Lett.*, 7(11):A435–A438, 2004.
- [62] Ryan W. Hart, Henry S. White, Bruce Dunn, and Debra R. Rolison. 3-d microbatteries. *Electrochem. Commun.*, 5(2):120 – 123, 2003.
- [63] Vahur Zadin, Heiki Kasemägi, Alvo Aabloo, and Daniel Brandell. Modelling electrode material utilization in the trench model 3D-microbattery by finite element analysis. *J. Power Sources*, 195(18):6218 – 6224, 2010.
- [64] Debra R. Rolison, Jeffrey W. Long, Justin C. Lytle, Anne E. Fischer, Christopher P. Rhodes, Todd M. McEvoy, Megan E. Bourg, and Alia M. Lubers. Multifunctional 3D nanoarchitectures for energy storage and conversion. *Chem. Soc. Rev.*, 38:226–252, 2009.
- [65] Phil Johns, Matthew Roberts, and John Owen. Conformal electrodeposition of manganese dioxide onto reticulated vitreous carbon for 3D microbattery

- applications. *J. Mater. Chem.*, 21(27):10153–10159, 2011.
- [66] Matthew Roberts, An Feng Huang, Phil Johns, and John Owen. Dip–spin coating of reticulated vitreous carbon with composite materials to act as an electrode for 3d microstructured lithium ion batteries. *J. Power Sources*, 224:250–259, 2 2013.
- [67] Jeffrey W. Long and Debra R. Rolison. Architectural design, interior decoration, and three-dimensional plumbing en route to multifunctional nanoarchitectures. *Acc. Chem. Res.*, 40(9):854–862, 09 2007.
- [68] Bing Sun, David Rehnlund, Matthew J. Lacey, and Daniel Brandell. Electrodeposition of thin poly(propylene glycol) acrylate electrolytes on 3D-nanopillar electrodes. *Electrochim. Acta*, 137:320–327, 8 2014.
- [69] G. Sun, J. I. Hur, X. Zhao, and C. J. Kim. Fabrication of very-high-aspect-ratio micro metal posts and gratings by photoelectrochemical etching and electroplating. *J. Microelectromech. Syst.*, 20(4):876–884, Aug 2011.
- [70] F. Chamran, Y. Yeh, H. S. Min, B. Dunn, and C. J. Kim. Fabrication of high-aspect-ratio electrode arrays for three-dimensional microbatteries. *J. Microelectromech. Syst.*, 16(4):844–852, Aug 2007.
- [71] Gabriel Oltean, Leif Nyholm, and Kristina Edström. Galvanostatic electrodeposition of aluminium nano-rods for Li-ion three-dimensional micro-battery current collectors. *Electrochim. Acta*, 56(9):3203 – 3208, 2011.
- [72] P. L. Taberna, S. Mitra, P. Poizot, P. Simon, and J. M. Tarascon. High rate capabilities Fe_3O_4 -based cu nano-architected electrodes for lithium-ion battery applications. *Nat. Mater.*, 5(7):567–573, 07 2006.
- [73] F. Chamran, Hong-Seok Min, B. Dunn, and Chang-Jin Kim. Three-dimensional nickel-zinc microbatteries. In *19th IEEE International Conference on Micro Electro Mechanical Systems*, pages 950–953, 2006.
- [74] Nicolas Cirigliano, Guangyi Sun, Daniel Membreno, Peter Malati, C. J. Kim, and Bruce Dunn. 3D architected anodes for lithium-ion microbatteries with large areal capacity. *Energy Technol.*, 2(4):362–369, 2014.
- [75] Etienne Eustache, Pascal Tilmant, Laurence Morgenroth, Pascal Roussel, Gilles Patriarche, David Troadec, Nathalie Rolland, Thierry Brousse, and Christophe Lethien. Silicon-microtube scaffold decorated with anatase TiO_2 as a negative electrode for a 3D lithium-ion microbattery. *Advanced Energy Materials*, 4(8):1301612–n/a, 2014. 1301612.
- [76] Evert Jonathan van den Ham, Sven Gielis, Marlies K. Van Bael, and An Hardy. Ultrasonic spray deposition of metal oxide films on high aspect ratio microstructures for three-dimensional all-solid-state li-ion batteries. *ACS Energy Lett.*, 1(6):1184–1188, 2016.
- [77] Mario Valvo, David Rehnlund, Ugo Lafont, Maria Hahlin, Kristina Edstrom, and Leif Nyholm. The impact of size effects on the electrochemical behaviour of Cu_2O -coated cu nanopillars for advanced Li-ion microbatteries. *J. Mater. Chem. A*, 2:9574–9586, 2014.
- [78] Emilie Perre, Pierre Louis Taberna, Driss Mazouzi, Philippe Poizot, Torbjörn Gustafsson, Kristina Edström, and Patrice Simon. Electrodeposited Cu_2S as anode material for 3-dimensional li-ion microbatteries. *Nano Lett.*, (8):1485–1491.
- [79] Chanyuan Liu, Eleanor I. Gillette, Xinyi Chen, Alexander J. Pearse,

- Alexander C. Kozen, Marshall A. Schroeder, Keith E. Gregorczyk, Sang Bok Lee, and Gary W. Rubloff. An all-in-one nanopore battery array. *Nat. Nano.*, 9(12):1031–1039, 12 2014.
- [80] Loic Baggetto, Harm C. M. Knoop, Rogier A. H. Niessen, Wilhelmus M. M. Kessels, and Peter H. L. Notten. 3D negative electrode stacks for integrated all-solid-state lithium-ion microbatteries. *J. Mater. Chem.*, 20:3703–3708, 2010.
- [81] P. H. L. Notten, F. Roozeboom, R. A. H. Niessen, and L. Baggetto. 3-D integrated all-solid-state rechargeable batteries. *Adv. Mater.*, 19(24):4564–4567, 2007.
- [82] M. Nathan, D. Golodnitsky, V. Yufit, E. Strauss, T. Ripenbein, I. Shechtman, S. Menkin, and E. Peled. Three-dimensional thin-film li-ion microbatteries for autonomous MEMS. *J. Microelectromech.*, 14(5):879–885, 2005.
- [83] Thomas Dobbelaere, Felix Mattelaer, Jolien Dendooven, Philippe Vereecken, and Christophe Detavernier. Plasma-enhanced atomic layer deposition of iron phosphate as a positive electrode for 3D lithium-ion microbatteries. *Chem. Mater.*, 28(10):3435–3445, 05 2016.
- [84] L. Baggetto, Rogier A. H. Niessen, Fred Roozeboom, and Peter H. L. Notten. High energy density all-solid-state batteries: A challenging concept towards 3D integration. *Adv. Funct. Mater.*, 18(7):1057–1066, 2008.
- [85] D. Golodnitsky, V. Yufit, M. Nathan, I. Shechtman, T. Ripenbein, E. Strauss, S. Menkin, and E. Peled. Advanced materials for the 3D microbattery. *Journal of Power Sources*, 153(2):281–287, 2 2006.
- [86] L. Baggetto, J.F.M. Oudenhoven, T. van Dongen, J.H. Klootwijk, M. Mulder, R.A.H. Niessen, M.H.J.M. de Croon, and P.H.L. Notten. On the electrochemistry of an anode stack for all-solid-state 3D-integrated batteries. *J. Power Sources*, 189(1):402 – 410, 2009. Selected Papers presented at the 14th IMLB-2008.
- [87] T. Ripenbein, D. Golodnitsky, M. Nathan, and E. Peled. Novel porous-silicon structures for 3D-interlaced microbatteries. *Electrochim. Acta*, 56(1):37 – 41, 2010.
- [88] Huigang Zhang, Xindi Yu, and Paul V. Braun. Three-dimensional bicontinuous ultrafast-charge and -discharge bulk battery electrodes. *Nat. Nano.*, 6(5):277–281, 05 2011.
- [89] Guangmin Zhou, Lu Li, Chaoqun Ma, Shaogang Wang, Ying Shi, Nikhil Koratkar, Wencai Ren, Feng Li, and Hui-Ming Cheng. A graphene foam electrode with high sulfur loading for flexible and high energy Li–S batteries. *Nano Energy*, 11:356–365, 1 2015.
- [90] Na Li, Zongping Chen, Wencai Ren, Feng Li, and Hui-Ming Cheng. Flexible graphene-based lithium ion batteries with ultrafast charge and discharge rates. *Proc. Natl. Acad. Sci. USA*, 109(43):17360–17365, 2012.
- [91] Junyi Ji, Hengxing Ji, Li Li Zhang, Xin Zhao, Xin Bai, Xiaobin Fan, Fengbao Zhang, and Rodney S. Ruoff. Graphene-encapsulated si on ultrathin-graphite foam as anode for high capacity lithium-ion batteries. *Adv. Mater.*, 25(33):4673–4677, 2013.
- [92] Anvar A. Zakhidov, Ray H. Baughman, Zafar Iqbal, Changxing Cui, Ilyas Khayrullin, Socrates O. Dantas, Jordi Marti, and Victor G. Ralchenko. Carbon

- structures with three-dimensional periodicity at optical wavelengths. *Science*, 282(5390):897–901, 1998.
- [93] Mara Olivares-Marin, Pablo Palomino, Jose Manuel Amarilla, Eduardo Enciso, and Dino Tonti. Effects of architecture on the electrochemistry of binder-free inverse opal carbons as Li-air cathodes in an ionic liquid-based electrolyte. *J. Mater. Chem. A*, 1(45):14270–14279, 2013.
- [94] K. T. Lee, J. C. Lytle, N. S. Ergang, S. M. Oh, and A. Stein. Synthesis and rate performance of monolithic macroporous carbon electrodes for lithium-ion secondary batteries. *Adv. Funct. Mater.*, 15(4):547–556, 2005.
- [95] Mukesh Agrawal, Soumyadip Choudhury, Katharina Gruber, Frank Simon, Dieter Fischer, Victoria Albrecht, Michael Göbel, Stefan Koller, Manfred Stamm, and Leonid Ionov. Porous carbon materials for li-s batteries based on resorcinol-formaldehyde resin with inverse opal structure. *J. Power Sources*, 261:363–370, 9 2014.
- [96] Zhiyong Wang, Fan Li, Nicholas S. Ergang, and Andreas Stein. Monolithic carbon-based nanocomposites with hierarchical porosity: Novel anode materials for Li-ion batteries. *ECS Transactions*, 6(25):199–204, 2008.
- [97] Zhiyong Wang, Fan Li, Nicholas S. Ergang, and Andreas Stein. Effects of hierarchical architecture on electronic and mechanical properties of nanocast monolithic porous carbons and carbon-carbon nanocomposites. *Chem. Mater.*, 18(23):5543–5553, 2006.
- [98] James H. Pikul, Hui Gang Zhang, Jiung Cho, Paul V. Braun, and William P. King. High-power lithium ion microbatteries from interdigitated three-dimensional bicontinuous nanoporous electrodes. *Nat. Commun.*, 4:1732 EP –, 04 2013.
- [99] Manon Létiche, Etienne Eustache, Jeremy Freixas, Arnaud Demortière, Vincent De Andrade, Laurence Morgenroth, Pascal Tilmant, François Vaurette, David Troadec, Pascal Roussel, Thierry Brousse, and Christophe Lethien. Atomic layer deposition of functional layers for on chip 3D Li-ion all solid state microbattery. *Adv. Energy Mater.*, pages 1601402–n/a, 2016.
- [100] J F Ribeiro, R Sousa, D J Cunha, E M F Vieira, M M Silva, L Dupont, and L M Goncalves. A chemically stable PVD multilayer encapsulation for lithium microbatteries. *J. Phys. D: Appl. Phys.*, 48(39):395306, 2015.
- [101] Woon-Gi Choi and Soon-Gil Yoon. Structural and electrical properties of LiCoO₂ thin-film cathodes deposited on planar and trench structures by liquid-delivery metalorganic chemical vapour deposition. *J. Power Sources*, 125(2):236–241, 1 2004.
- [102] C. V. Ramana, K. Zaghib, and C. M. Julien. Pulsed-laser deposited LiNi_{0.8}Co_{0.15}Al_{0.05}O₂ thinfilmsforapplicationinmicrobatteries, ty = JOUR, url = <http://dx.doi.org/10.1063/1.2430933>, volume = 90, year = 2007, year1 = 2007, bdsk-url-1 = <http://dx.doi.org/10.1063/1.2430933>. *Appl. Phys. Lett.*, (2):021916.
- [103] Binggong Yan, Jichang Liu, Bohang Song, Pengfei Xiao, and Li Lu. Li-rich thin film cathode prepared by pulsed laser deposition. *Sci. Rep.*, 3:3332 EP –, 11 2013.
- [104] Jinkui Feng, Binggong Yan, Man O. Lai, and Lu Li. Design and fabrication of an all-solid-state thin-film li-ion microbattery with amorphous TiO₂ as the

- anode. *Energy Technology*, 2(4):397–400, 2014.
- [105] J. K. Feng, M. O. Lai, Xianting Zeng, Zhaohong Huang, and L. Lu. Spie proceedings: All-solid-state thin film microbatteries fabricated by rf sputtering. volume 8035, pages 80350E–80350E–6, 2011.
- [106] H. Y. Park, S. R. Lee, Y. J. Lee, B. W. Cho, and W. I. Cho. Bias sputtering and characterization of LiCoO_2 thin film cathodes for thin film microbattery. *Mater. Chem. and Phys.*, 93(1):70–78, 9 2005.
- [107] Jadra Mosa, Mario Aparicio, Alicia Duran, Christel Laberty-Robert, and Clement Sanchez. Nanocrystalline mesoporous LiFePO_4 thin-films as cathodes for Li-ion microbatteries. *J. Mater. Chem. A*, 2(9):3038–3046, 2014.
- [108] Ugo Lafont, Anca Anastasopol, Esteban Garcia-Tamayo, and Erik Kelder. Electrostatic spray pyrolysis of $\text{LiNi}_{0.5}\text{Mn}_{1.5}\text{O}_4$ films for 3D Li-ion microbatteries. *Thin Solid Films*, 520(9):3464–3471, 2 2012.
- [109] F. K. Shokoohi, J. M. Tarascon, and B. J. Wilkens. Fabrication of thin?film LiMn_2O_4 cathodes for rechargeable microbatteries. *Appl. Phys. Lett.*, 59(10):1260–1262, 2017/01/02 1991.
- [110] Barbara Laïk, Laurent Eude, Jean-Pierre Pereira-Ramos, Costel Sorin Cojocaru, Didier Pribat, and Emmanuelle Rouvière. Silicon nanowires as negative electrode for lithium-ion microbatteries. *Electrochim. Acta*, 53(17):5528–5532, 7 2008.
- [111] Jae Joon Lee, Soo Ho Kim, Seung Hyun Jee, Young Soo Yoon, Won Il Cho, Seok Jin Yoon, Ji Won Choi, and Sang-Cheol Nam. Characteristics of $\text{Sn}/\text{Li}_2\text{O}$ multilayer composite anode for thin film microbattery. *J. Power Sources*, 178(1):434–438, 3 2008.
- [112] M. Rosa Palacin. Recent advances in rechargeable battery materials: a chemist’s perspective. *Chem. Soc. Rev.*, 38(9):2565–2575, 2009.
- [113] J.B. Bates, G.R. Gruzalski, N.J. Dudney, C.F. Luck, and Xiaohua Yu. Rechargeable thin-film lithium batteries. *Solid State Ionics*, 70:619 – 628, 1994.
- [114] Daniel T. Hallinan Jr. and Nitash P. Balsara. Polymer electrolytes. *Annu. Rev. Mater. Res.*, 43(1):503–525, 2013.
- [115] J. Mindemark, B. Sun, and D. Brandell. Hydroxyl-functionalized poly(trimethylene carbonate) electrolytes for 3D-electrode configurations. *Polym. Chem.*, 6:4766–4774, 2015.
- [116] Noriaki Kamaya, Kenji Homma, Yuichiro Yamakawa, Masaaki Hirayama, Ryoji Kanno, Masao Yonemura, Takashi Kamiyama, Yuki Kato, Shigenori Hama, Koji Kawamoto, and Akio Mitsui. A lithium superionic conductor. *Nat Mater*, 10(9):682–686, 09 2011.
- [117] Yuki Kato, Satoshi Hori, Toshiya Saito, Kota Suzuki, Masaaki Hirayama, Akio Mitsui, Masao Yonemura, Hideki Iba, and Ryoji Kanno. High-power all-solid-state batteries using sulfide superionic conductors. *Nat. Energy*, 1:16030 EP –, 03 2016.
- [118] Seung-Wan Song, Ki-Chang Lee, and Ho-Young Park. High-performance flexible all-solid-state microbatteries based on solid electrolyte of lithium boron oxynitride. *J. Power Sources*, 328:311 – 317, 2016.
- [119] Alexander C. Kozen, Alexander J. Pearse, Chuan-Fu Lin, Malachi Noked, and Gary W. Rubloff. Atomic layer deposition of the solid electrolyte LiPON.

- Chem. of Mater.*, 27(15):5324–5331, 2015.
- [120] Nareerat Plylahan, Nana Amponsah Kyeremateng, Marielle Eyraud, Frederic Dumur, Hervé Martinez, Lionel Santinacci, Philippe Knauth, and Thierry Djenizian. Highly conformal electrodeposition of copolymer electrolytes into titania nanotubes for 3d li-ion batteries. *Nanoscale Res. Lett.*, 7(1):349, 2012.
 - [121] Semra Tan, Sylwia Walus, Jöns Hilborn, Torbjörn Gustafsson, and Daniel Brandell. Poly(ether amine) and cross-linked poly(propylene oxide) diacrylate thin-film polymer electrolyte for 3D-microbatteries. *Electrochem. Commun.*, 12(11):1498 – 1500, 2010.
 - [122] Boyko Tsyntarski, Bilyana Petrova, Temenuzhka Budinova, Nartzislav Petrov, Leticia F. Velasco, JoséB. Parra, and Conchi O. Ania. Porosity development during steam activation of carbon foams from chemically modified pitch. *Micropor. Mesopor. Mat.*, 154:56–61, 5 2012.
 - [123] Masaya Kodama, Junya Yamashita, Yasushi Soneda, Hiroaki Hatori, and Katsumi Kamegawa. Preparation and electrochemical characteristics of n-enriched carbon foam. *Carbon*, 45(5):1105 – 1107, 2007.
 - [124] Joji Hasegawa, Kazuyoshi Kanamori, Kazuki Nakanishi, and Teiichi Hanada. Macro- and microporous carbon monoliths with high surface areas pyrolyzed from poly(divinylbenzene) networks. *C. R. Chim.*, 13(1-Ä2):207 – 211, 2010.
 - [125] George Hasegawa, Kazuyoshi Kanamori, Kazuki Nakanishi, and Teiichi Hanada. Fabrication of activated carbons with well-defined macropores derived from sulfonated poly(divinylbenzene) networks. *Carbon*, 48(6):1757 – 1766, 2010.
 - [126] Shu ping Zhang, Ming xian Liu, Li hua Gan, Fang rui Wu, Zi jie Xu, Zhi xian Hao, and Long wu Chen. Synthesis of carbon foams with a high compressive strength from arylacetylene. *New Carbon Mater.*, 25(1):9 – 14, 2010.
 - [127] Zhiyong Wang, Elizabeth R. Kiesel, and Andreas Stein. Silica-free syntheses of hierarchically ordered macroporous polymer and carbon monoliths with controllable mesoporosity. *J. Mater. Chem.*, 18:2194–2200, 2008.
 - [128] A. Taguchi, J. H. Smått, and M. Lindén. Carbon monoliths possessing a hierarchical, fully interconnected porosity. *Adv. Mater.*, 15(14):1209–1211, 2003.
 - [129] Linghui Yu, Nicolas Brun, Ken Sakaushi, Jürgen Eckert, and Magdalena M. Titirici. Hydrothermal nanocasting: Synthesis of hierarchically porous carbon monoliths and their application in lithium–sulfur batteries. *Carbon*, 61:245–253, 9 2013.
 - [130] Neil R. Cameron. High internal phase emulsion templating as a route to well-defined porous polymers. *Polymer*, 46(5):1439 – 1449, 2005.
 - [131] N. R. Cameron and D. C. Sherrington. *High internal phase emulsions (HIPEs) — Structure, properties and use in polymer preparation*, pages 163–214. Springer Berlin Heidelberg, Berlin, Heidelberg, 1996.
 - [132] Michael S. Silverstein and Neil R. Cameron. *PolyHIPEs-Porous Polymers from High Internal Phase Emulsions*. John Wiley & Sons, Inc., 2002.
 - [133] Andrea Barbetta, Neil R. Cameron, and Sharon J. Cooper. High internal phase emulsions (HIPEs) containing divinylbenzene and 4-vinylbenzyl chloride and the morphology of the resulting PolyHIPE materials. *Chem. Commun.*, pages 221–222, 2000.

- [134] I. Pulko and P. Krajnc. High internal phase emulsion templating-a path to hierarchically porous functional polymers. *Macromol. Rapid Commun.*, 33(20):1731–1746, 2012.
- [135] S. D. Kimmins and N. R. Cameron. Functional porous polymers by emulsion templating: Recent advances. *Adv. Funct. Mater.*, 21(2):211–225, 2011.
- [136] H. Zhang and A. I. Cooper. Synthesis and applications of emulsion-templated porous materials. *Soft Matter*, 1:107–113, 2005.
- [137] D. Wang, N. L. Smith, and P. M Budd. Polymerization and carbonization of high internal phase emulsions. *Polym. Int.*, 54(2):297–303, 2005.
- [138] Noa Cohen and M. S. Silverstein. Synthesis of emulsion-templated porous polyacrylonitrile and its pyrolysis to porous carbon monoliths. *Polymer*, 52(2):282 – 287, 2011.
- [139] O. Kulygin and M. S. Silverstein. Porous poly(2-hydroxyethyl methacrylate) hydrogels synthesized within high internal phase emulsions. *Soft Matter*, 3:1525–1529, 2007.
- [140] R. Butler, I. Hopkinson, and A. I. Cooper. Synthesis of porous emulsion-templated polymers using high internal phase CO₂-in-water emulsions. *J. Am. Chem. Soc.*, 125(47):14473–14481, 2003.
- [141] P. Krajnc, D. Štefanec, and I. Pulko. Acrylic acid reversed PolyHIPEs. *Macromol. Rapid Commun.*, 26(16):1289–1293, 2005.
- [142] F. Audouin, M. Birot, É. Pasquinet, O. Besnard, P. Palmas, D. Poullain, and H. Deleuze. Preparation, solid-state nmr, and physicochemical characterization of surprisingly tough open cell polyhypes derived from 1-vinyl-1,2,4-triazole oil-in-water emulsions. *Macromolecules*, 44(12):4879–4886, 06 2011.
- [143] C. Youssef, R. Backov, M. Treguer, M. Birot, and H. Deleuze. Preparation of remarkably tough polyHIPE materials via polymerization of oil-in-water HIPEs involving 1-vinyl-5-aminotetrazole. *J. Polym. Sci. A Polym. Chem.*, 48(13):2942–2947, 2010.
- [144] A. Szczurek, V. Fierro, A. Pizzi, and A. Celzard. Emulsion-templated porous carbon monoliths derived from tannins. *Carbon*, 74:352 – 362, 2014.
- [145] I. Gurevitch and M. S. Silverstein. Polymerized pickering HIPEs: Effects of synthesis parameters on porous structure. *J. Polym. Sci. A Polym. Chem.*, 48(7):1516–1525, 2010.
- [146] Angelika Menner, Vivian Ikem, Mariely Salgueiro, Milo S. P. Shaffer, and Alexander Bismarck. High internal phase emulsion templates solely stabilised by functionalised titania nanoparticles. *Chem. Commun.*, (41):4274–4276, 2007.
- [147] Robert Owen, Colin Sherborne, Thomas Paterson, Nicola H. Green, Gwendolen C. Reilly, and Frederik Claeyssens. Emulsion templated scaffolds with tunable mechanical properties for bone tissue engineering. *J. Mech. Behav. Biomed. Mater.*, 54:159 – 172, 2016.
- [148] Ai juan Wang, Thomas Paterson, Robert Owen, Colin Sherborne, James Dugan, Jun ming Li, and Frederik Claeyssens. Photocurable high internal phase emulsions (HIPEs) containing hydroxyapatite for additive manufacture of tissue engineering scaffolds with multi-scale porosity. *Mater. Sci. Eng. C*, 67:51 – 58, 2016.
- [149] I. Cooperstein, M. Layani, and S. Magdassi. 3D printing of porous structures

- by UV-curable O/W emulsion for fabrication of conductive objects. *J. Mater. Chem. C*, 3:2040–2044, 2015.
- [150] M. Sušec, S. C. Ligon, J. Stampfl, R. Liska, and P. Krajnc. Hierarchically porous materials from layer-by-layer photopolymerization of high internal phase emulsions. *Macromol. Rapid Commun.*, 34(11):938–943, 2013.
- [151] D. W. Johnson, C. Sherborne, M. P. Didsbury, C. Pateman, N. R. Cameron, and F. Claeysens. Macrostructuring of emulsion-templated porous polymers by 3D laser patterning. *Adv. Mater.*, 25(23):3178–3181, 2013.
- [152] F. Audouin, M. Birot, É. Pasquinet, H. Deleuze, O. Besnard, and D. Poullain. Synthesis of porous materials by 2-nitroresorcinol/cyanuric chloride thermal polycondensation in emulsions. *J. Appl. Polym. Sci.*, 108(5):2808–2813, 2008.
- [153] A. F. Gross and A. P. Nowak. Hierarchical carbon foams with independently tunable mesopore and macropore size distributions. *Langmuir*, 26(13):11378–11383, 2010.
- [154] H. Deleuze, R. Faivre, and V. Herroquez. Preparation and functionalisation of emulsion-derived microcellular polymeric foams (polyHIPEs) by ring-opening metathesis polymerisation (ROMP). *Chem. Commun.*, pages 2822–2823, 2002.
- [155] S. Kovacic, K. Jerabek, P. Krajnc, and C. Slugovc. Ring opening metathesis polymerisation of emulsion templated dicyclopentadiene giving open porous materials with excellent mechanical properties. *Polym. Chem.*, 3:325–328, 2012.
- [156] Y. Luo, A.-N. Wang, and X. Gao. Pushing the mechanical strength of polyhypes up to the theoretical limit through living radical polymerization. *Soft Matter*, 8:1824–1830, 2012.
- [157] N. R. Cameron, D. C. Sherrington, I. Ando, and H. Kurosu. Chemical modification of monolithic poly(styrene-divinylbenzene) polyhipe materials. *J. Mater. Chem.*, 6:719–726, 1996.
- [158] Joseph R. Duke, Mark A. Hoisington, David A. Langlois, and Brian C. Benicewicz. High temperature properties of poly(styreneco-alkylmaleimide) foams prepared by high internal phase emulsion polymerization. *Polymer*, 39(18):4369 – 4378, 1998.
- [159] H. D. Asfaw, R. Younesi, M. Valvo, J. Maibach, J. Ångström, C.-W. Tai, Z. Bacsik, M. Sahlberg, L. Nyholm, and K. Edström. Boosting the thermal stability of emulsion-templated polymers via sulfonation: an efficient synthetic route to hierarchically porous carbon foams. *ChemistrySelect*, 1(4):784–792, 2016.
- [160] Barby Donald and Haq Zia. Low density porous cross-linked polymeric materials and their preparation, patent number: EP19820301199 19820309, 1982.
- [161] M. M. Alam, J. Miras, L. A. Pérez-Carrillo, S. Vílchez, C. Solans, T. Imae, M. Ujihara, and J. Esquena. Facile synthesis of dual micro/macroporous carbonaceous foams by templating in highly concentrated water-in-oil emulsions. *Micropor. Mesopor. Mat.*, 182:102–108, 12 2013.
- [162] Wencui Li, G Reichenauer, and J Fricke. Carbon aerogels derived from cresol-resorcinol-formaldehyde for supercapacitors. *Carbon*, 40(15):2955–2959, 2002.

- [163] N. Brun, L. Edembe, S. Gounel, N. Mano, and M. M. Titirici. Emulsion-templated macroporous carbons synthesized by hydrothermal carbonization and their application for the enzymatic oxidation of glucose. *ChemSusChem*, 6(4):701–710, 2013.
- [164] Mingxian Liu, Lihua Gan, Fengqi Zhao, Huixiang Xu, Xuezhong Fan, Ci Tian, Xi Wang, Zijie Xu, Zhixian Hao, and Longwu Chen. Carbon foams prepared by an oil-in-water emulsion method. *Carbon*, 45(13):2710 – 2712, 2007.
- [165] N. Thongprachan, T. Yamamoto, J. Chaichanawong, T. Ohmori, and A. Endo. Preparation of macroporous carbon foam using emulsion templating method. *Adsorption*, 17(1):205–210, 2011.
- [166] S. Vílchez, L. A. Pérez-Carrillo, J. Miras, C. Solans, and J. Esquena. Oil-in-alcohol highly concentrated emulsions as templates for the preparation of macroporous materials. *Langmuir*, 28(20):7614–7621, 2012.
- [167] N. Brun, S. R. S. Prabakaran, M. Morcrette, C. Sanchez, G. Pécastaings, A. Derré, A. Soum, H. Deleuze, M. Birot, and R. Backov. Hard macrocellular silica Si(HIPE) foams templating micro/macroporous carbonaceous monoliths: Applications as lithium ion battery negative electrodes and electrochemical capacitors. *Adv. Funct. Mater.*, 19(19):3136–3145, 2009.
- [168] Ilke Akartuna, André R. Studart, Elena Tervoort, and Ludwig J. Gauckler. Macroporous ceramics from particle-stabilized emulsions. *Adv. Mater.*, 20(24):4714–4718, 2008.
- [169] Vivian O. Ikem, Angelika Menner, and Alexander Bismarck. High internal phase emulsions stabilized solely by functionalized silica particles. *Angew. Chem. Int. Ed.*, 48(4):632–632, 2009.
- [170] Guanqing Sun, Zifu Li, and To Ngai. Inversion of particle-stabilized emulsions to form high-internal-phase emulsions. *Angew. Chem. Int. Ed.*, 49(12):2163–2166, 2010.
- [171] Zifu Li, Tian Ming, Jianfang Wang, and To Ngai. High internal phase emulsions stabilized solely by microgel particles. *Angew. Chem. Int. Ed.*, 48(45):8490–8493, 2009.
- [172] Yun Zhu, Ranran Zhang, Shengmiao Zhang, Yeqian Chu, and Jianding Chen. Macroporous polymers with aligned microporous walls from pickering high internal phase emulsions. *Langmuir*, 32(24):6083–6088, 2016.
- [173] B. Zhang, J. Zhang, C. Liu, L. Peng, X. Sang, B. Han, X. Ma, T. Luo, X. Tan, and G. Yang. High-internal-phase emulsions stabilized by metal-organic frameworks and derivation of ultralight metal-organic aerogels. *Sci. Rep.*, 6:21401 EP –, 02 2016.
- [174] Jia Huo, Marco Marcello, Ashesh Garai, and Darren Bradshaw. MOF-polymer composite microcapsules derived from pickering emulsions. *Adv. Mater.*, 25(19):2717–2722, 2013.
- [175] Bo Xiao, Qingchun Yuan, and Richard A. Williams. Exceptional function of nanoporous metal organic framework particles in emulsion stabilisation. *Chem. Commun.*, 49:8208–8210, 2013.
- [176] Angelika Menner, Raquel Verdejo, Milo Shaffer, and Alexander Bismarck. Particle-stabilized surfactant-free medium internal phase emulsions as templates for porous nanocomposite materials: poly-pickering-foams. *Langmuir*, 23(5):2398–2403, 2007.

- [177] Robert T. Woodward, Derrick W.H. Fam, David B. Anthony, Jindui Hong, Tom O. McDonald, Camille Petit, Milo S.P. Shaffer, and Alexander Bismarck. Hierarchically porous carbon foams from pickering high internal phase emulsions. *Carbon*, 101:253 – 260, 2016.
- [178] Robert T. Woodward, François De Luca, Aled D. Roberts, and Alexander Bismarck. High-surface-area, emulsion-templated carbon foams by activation of polyHIPEs derived from pickering emulsions. *Materials*, 9(9):776, 2016.
- [179] Simona Ungureanu, Marc Birot, Hervé Deleuze, Véronique Schmitt, Nicolas Mano, and Rénal Backov. Triple hierarchical micro–meso–macroporous carbonaceous foams bearing highly monodisperse macroporosity. *Carbon*, 91:311–320, 9 2015.
- [180] Lee SJ. Flow behavior of high internal phase emulsions and preparation to microcellular foam. *Korea-Aust. Rheol. J.*, 16(3):153–160, 2004.
- [181] Cynthia F. Welch, Gene D. Rose, David Malotky, and Sarah T. Eckersley. Rheology of high internal phase emulsions. *Langmuir*, 22(4):1544–1550, 02 2006.
- [182] Ross J. Carnachan, Maria Bokhari, Stefan A. Przyborski, and Neil R. Cameron. Tailoring the morphology of emulsion-templated porous polymers. *Soft Matter*, 2(7):608–616, 2006.
- [183] C. Y. Liang and S. Krimm. Infrared spectra of high polymers. vi. polystyrene. *J. Polym. Sci.*, 27(115):241–254, 1958.
- [184] R. D. Kross, V. A. Fassel, and M. Margoshes. The infrared spectra of aromatic compounds. ii. evidence concerning the interaction of π -electrons and σ -bond orbitals in C–H out-of-plane bending vibrations1. *J. Am. Chem. Soc.*, 78(7):1332–1335, 04 1956.
- [185] George Socrates. *Infrared and Raman Characteristic Group Frequencies Tables and Charts*. John Wiley & Sons Ltd, 3 edition, 02 2004. An optional note.
- [186] Jin Chuan Yang, Michael J Jablonsky, and Jimmy W Mays. NMR and FT–IR studies of sulfonated styrene-based homopolymers and copolymers. *Polymer*, 43(19):5125–5132, 9 2002.
- [187] Yang Yang, Ying Chu, Fuyong Yang, and Yanping Zhang. Uniform hollow conductive polymer microspheres synthesized with the sulfonated polystyrene template. *Mater. Chem. Phys.*, 92(1):164–171, 7 2005.
- [188] El Mostafa Moujahid, Jérôme Inacio, Jean-Pierre Besse, and Fabrice Leroux. Adsorption of styrene sulfonate vs. polystyrene sulfonate on layered double hydroxides. *Micropor. Mesopor. Mat.*, 57(1):37–46, 1 2003.
- [189] Masami Matsuda, Kiyomi Funabashi, Hideo Yusa, and Makoto Kikuchi. Influence of functional sulfonic acid group on pyrolysis characteristics for cation exchange resin. *Journal of Nuclear Science and Technology*, 24(2):124–128, 02 1987.
- [190] Masami Matsuda and Kiyomi Funabashi. Influence of functional sulfonic acid groups on styrene–divinylbenzene copolymer pyrolysis. *J. Polym. Sci. A Polym. Chem.*, 25(2):669–673, 1987.
- [191] Chang Hyuck Choi, Sung Hyeon Park, and Seong Ihl Woo. Heteroatom doped carbons prepared by the pyrolysis of bio-derived amino acids as highly active catalysts for oxygen electro-reduction reactions. *Green Chem.*, 13(2):406–412,

- 2011.
- [192] Michael Schuster, Carla C. de Araujo, Vladimir Atanasov, Henrik T. Andersen, Klaus-Dieter Kreuer, and Joachim Maier. Highly sulfonated poly(phenylene sulfone): Preparation and stability issues. *Macromolecules*, 42(8):3129–3137, 04 2009.
 - [193] Michael Schuster, Klaus-Dieter Kreuer, Henrik T. Andersen, and Joachim Maier. Sulfonated poly(phenylene sulfone) polymers as hydrolytically and thermooxidatively stable proton conducting ionomers. *Macromolecules*, 40(3):598–607, 02 2007.
 - [194] Dun Chen, Xiang Gao, and David Dollimore. A generalized form of the Kissinger equation. *Thermochim. Acta*, 215:109–117, 1993.
 - [195] James W. Neely. Characterization of polymer carbons derived from porous sulfonated polystyrene. *Carbon*, 19(1):27–36, 1981.
 - [196] Rosalind E. Franklin. Crystallite growth in graphitizing and non-graphitizing carbons. *Proc. R. Soc. A: Mathematical and Physical Sciences*, 209(1097):196–218, 1951.
 - [197] Peter J. F. Harris. New perspectives on the structure of graphitic carbons. *Critical Reviews in Solid State and Materials Sciences*, 30(4):235–253, 10 2005.
 - [198] P. J. F. Harris. Structure of non-graphitising carbons. *International Materials Reviews*, 42(5):206–218, 09 1997.
 - [199] George Hasegawa, Kazuyoshi Kanamori, Naokatsu Kannari, Jun-ichi Ozaki, Kazuki Nakanishi, and Takeshi Abe. Hard carbon anodes for Na-ion batteries: Toward a practical use. *ChemElectroChem*, 2(12):1917–1920, 2015.
 - [200] A. C. Ferrari and J. Robertson. Interpretation of Raman spectra of disordered and amorphous carbon. *Phys. Rev. B*, 61(20):14095–14107, 05 2000.
 - [201] Yan Wang, Daniel C. Alsmeyer, and Richard L. McCreery. Raman spectroscopy of carbon materials: structural basis of observed spectra. *Chem. Mater.*, 2(5):557–563, 09 1990.
 - [202] Stephanie Reich and Christian Thomsen. Raman spectroscopy of graphite. *Phil. Trans. R. Soc. A: Mathematical, Physical and Engineering Sciences*, 362(1824):2271–2288, 2004.
 - [203] Yasushi Kawashima and Gen Katagiri. Fundamentals, overtones, and combinations in the raman spectrum of graphite. *Phys. Rev. B*, 52(14):10053–10059, 10 1995.
 - [204] R. J. Nemanich and S. A. Solin. First- and second-order raman scattering from finite-size crystals of graphite. *Phys. Rev. B*, 20(2):392–401, 07 1979.
 - [205] A. C. Ferrari and J. Robertson. Resonant raman spectroscopy of disordered, amorphous, and diamondlike carbon. *Phys. Rev. B*, 64(7):075414–, 07 2001.
 - [206] Edward Buell and J. R. Dahn. Li-insertion in hard carbon anode materials for Li-ion batteries. *Electrochim. Acta*, 45(1–2):121–130, 9 1999.
 - [207] F. Béguin, F. Chevallier, C. Vix-Guterl, S. Saadallah, V. Bertagna, J. N. Rouzaud, and E. Frackowiak. Correlation of the irreversible lithium capacity with the active surface area of modified carbons. *Carbon*, 43(10):2160–2167, 8 2005.
 - [208] D. Larcher, C. Mudalige, M. Gharghour, and J. R. Dahn. Electrochemical insertion of Li and irreversibility in disordered carbons prepared from oxygen

- and sulfur-containing pitches. *Electrochim. Acta*, 44(23):4069–4072, 7 1999.
- [209] Andreas Hirsch. The era of carbon allotropes. *Nat. Mater.*, 9(11):868–871, 11 2010.
- [210] Tao Zheng and J. R. Dahn. Hysteresis observed in quasi open-circuit voltage measurements of lithium insertion in hydrogen-containing carbons. *J. Power Sources*, 68(2):201–203, 1997.
- [211] Jaroslav Stejskal, Miroslava Trchová, Patrycja Bober, Petr Humpolíček, Věra Kašpárková, Irina Sapurina, Mikhail A. Shishov, and Martin Varga. *Conducting Polymers: Polyaniline*. John Wiley & Sons, Inc., 2002.
- [212] Hongjun Yang and Allen J. Bard. The application of fast scan cyclic voltammetry. mechanistic study of the initial stage of electropolymerization of aniline in aqueous solutions. *J. Electroanal. Chem.*, 339(1):423–449, 1992.
- [213] P. Nunziante and G. Pistoia. Factors affecting the growth of thick polyaniline films by the cyclic voltammetry technique. *Electrochim. Acta*, 34(2):223–228, 1989.
- [214] A. Guiseppi-Elie, S. R. Pradhan, A. M. Wilson, D. L. Allara, P. Zhang, R. W. Collins, and Y. T. Kim. Growth of electropolymerized polyaniline thin films. *Chem. of Mater.*, 5(10):1474–1480, 10 1993.
- [215] Florence Fusalba and Daniel Bélanger. Electropolymerization of polypyrrole and polyaniline-polypyrrole from organic acidic medium. *J. Phys. Chem. B*, 103(42):9044–9054, 10 1999.
- [216] A. G MacDiarmid, L. S Yang, W. S Huang, and B. D Humphrey. Polyaniline: Electrochemistry and application to rechargeable batteries. *Synth. Met.*, 18(1):393–398, 1987.
- [217] E. M. Geniès, M. Lapkowski, and J. F. Penneau. Cyclic voltammetry of polyaniline: interpretation of the middle peak. *J. electroanal. chem. interfacial electrochem.*, 249(1):97–107, 1988.
- [218] Petr Novák, Klaus Müller, K. S. V. Santhanam, and Otto Haas. Electrochemically active polymers for rechargeable batteries. *Chem. Rev.*, 97(1):207–282, 02 1997.
- [219] James Manuel, Jae-Kwang Kim, Aleksandar Matic, Per Jacobsson, Ghanshyam S. Chauhan, Jong Keun Ha, Kwon-Koo Cho, and Jou-Hyeon Ahn. Electrochemical properties of lithium polymer batteries with doped polyaniline as cathode material. *Mater. Res. Bull.*, 47(10):2815–2818, 10 2012.
- [220] Miroslava Trchová and Jaroslav Stejskal. Polyaniline: The infrared spectroscopy of conducting polymer nanotubes (iupac technical report). *IUPAC*, 83(10):1803–1817
- [221] H. Mazor, D. Golodnitsky, L. Burstein, A. Gladkich, and E. Peled. Electrophoretic deposition of lithium iron phosphate cathode for thin-film 3d-microbatteries. *J. Power Sources*, 198:264 – 272, 2012.
- [222] Robert Dominko, Marjan Bele, Jean-Michel Goupil, Miran Gaberscek, Darko Hanzel, Iztok Arcon, and Janez Jamnik. Wired porous cathode materials: A novel concept for synthesis of LiFePO_4 . *Chem. Mater.*, 19(12):2960–2969, 06 2007.
- [223] Miran Gaberscek, Robert Dominko, Marjan Bele, Maja Remskar, Darko Hanzel, and Janko Jamnik. Porous, carbon-decorated LiFePO_4 prepared by sol–gel method based on citric acid. *Solid State Ionics*,

- 176(19–22):1801–1805, 6 2005.
- [224] Antonino Salvatore Arico, Peter Bruce, Bruno Scrosati, Jean-Marie Tarascon, and Walter van Schalkwijk. Nanostructured materials for advanced energy conversion and storage devices. *Nat. Mater.*, 4(5):366–377, 05 2005.
 - [225] J. Come, P.-L. Taberna, S. Hamelet, C. Masquelier, and P. Simon. Electrochemical kinetic study of LiFePO_4 using cavity microelectrode. *J. Electrochem. Soc.*, 158(10):A1090–A1093, 2011.
 - [226] Denis Y. W. Yu, Christopher Fietzek, Wolfgang Weydanz, Kazunori Donoue, Takao Inoue, Hiroshi Kurokawa, and Shin Fujitani. Study of LiFePO_4 by cyclic voltammetry. *J. Electrochem. Soc.*, 154(4):A253–A257, 2007.
 - [227] Kun Tang, Xiqian Yu, Jinpeng Sun, Hong Li, and Xuejie Huang. Kinetic analysis on LiFePO_4 thin films by cv, gitt, and {EIS}. *Electroch. Acta*, 56(13):4869 – 4875, 2011.
 - [228] Ruhul Amin, Palani Balaya, and Joachim Maier. Anisotropy of electronic and ionic transport in LiFePO_4 single crystals. *Electrochem. Solid State Lett.*, 10(1):A13–A16, 2007.
 - [229] Rahul Malik, Damian Burch, Martin Bazant, and Gerbrand Ceder. Particle size dependence of the ionic diffusivity. *Nano Lett.*, 10(10):4123–4127, 10 2010.
 - [230] Phil A. Johns, Matthew R. Roberts, Yasuaki Wakizaka, James H. Sanders, and John R. Owen. How the electrolyte limits fast discharge in nanostructured batteries and supercapacitors. *Electrochem. Commun.*, 11(11):2089–2092, 11 2009.
 - [231] Fiona C. Strobridge, Bernardo Orvananos, Mark Croft, Hui-Chia Yu, Rosa Robert, Hao Liu, Zhong Zhong, Thomas Connolley, Michael Drakopoulos, Katsuyo Thornton, and Clare P. Grey. Mapping the inhomogeneous electrochemical reaction through porous LiFePO_4 -electrodes in a standard coin cell battery. *Chem. Mater.*, 27(7):2374–2386, 04 2015.
 - [232] Veronica Augustyn, Jérémy Come, Michael A. Lowe, Jong Woung Kim, Pierre-Louis Taberna, Sarah H. Tolbert, Héctor D. Abruña, Patrice Simon, and Bruce Dunn. High-rate electrochemical energy storage through Li^+ intercalation pseudocapacitance. *Nat. Mater.*, 12(6):518–522, 06 2013.
 - [233] Lingping Kong, Chuanfang Zhang, Jitong Wang, Wenming Qiao, Licheng Ling, and Donghui Long. Nanoarchitected Nb_2O_5 hollow, Nb_2O_5 @carbon and NbO_2 @carbon core-shell microspheres for ultrahigh-rate intercalation pseudocapacitors. *Sci. Rep.*, 6:21177 EP –, 02 2016.
 - [234] Torsten Brezesinski, John Wang, Sarah H. Tolbert, and Bruce Dunn. Ordered mesoporous $[\alpha]\text{-MoO}_3$ with iso-oriented nanocrystalline walls for thin-film pseudocapacitors. *Nat. Mater.*, 9(2):146–151, 02 2010.
 - [235] M Ristić, S Popović, and S Musić. Sol–gel synthesis and characterization of Nb_2O_5 powders. *Mater. Lett.*, 58(21):2658–2663, 8 2004.
 - [236] Hao-Jie Zhang, Jie Shu, Kai-Xue Wang, Xiao-Ting Chen, Yan-Mei Jiang, Xiao Wei, and Jie-Sheng Chen. Lithiation mechanism of hierarchical porous MoO_2 nanotubes fabricated through one-step carbothermal reduction. *J. Mater. Chem. A*, 2(1):80–86, 2014.
 - [237] Ye Zhao, Zhengjun Zhang, and Yuanhua Lin. Optical and dielectric properties of a nanostructured NbO_2 thin film prepared by thermal oxidation. *J. Phys. D: Appl. Phys.*, 37(24):3392, 2004.

- [238] Zhang Weibin, Wu Weidong, Wang Xueming, Cheng Xinlu, Yan Dawei, Shen Changle, Peng Liping, Wang Yuying, and Bai Li. The investigation of NbO₂ and Nb₂O₅ electronic structure by XPS, UPS and first principles methods. *Surf. Interface Anal.*, 45(8):1206–1210, 2013.
- [239] M. J. Olszta, J. Wang, and E. C. Dickey. Stoichiometry and valence measurements of niobium oxides using electron energy-loss spectroscopy. *Journal of Microscopy*, 224(3):233–241, 2006.
- [240] David Pech, Magali Brunet, Hugo Durou, Peihua Huang, Vadym Mochalin, Yury Gogotsi, Pierre-Louis Taberna, and Patrice Simon. Ultrahigh-power micrometre-sized supercapacitors based on onion-like carbon. *Nat. Nano.*, 5(9):651–654, 09 2010.
- [241] Shuang Wang, Ben Hsia, Carlo Carraro, and Roya Maboudian. High-performance all solid-state micro-supercapacitor based on patterned photoresist-derived porous carbon electrodes and an ionogel electrolyte. *J. Mater. Chem. A*, 2(21):7997–8002, 2014.
- [242] Maher F. El-Kady, Melanie Ihns, Mengping Li, Jee Youn Hwang, Mir F. Mousavi, Lindsay Chaney, Andrew T. Lech, and Richard B. Kaner. Engineering three-dimensional hybrid supercapacitors and microsupercapacitors for high-performance integrated energy storage. *Proc. Natl. Acad. Sci. USA*, 112(14):4233–4238, 2015.
- [243] Narendra Kurra, Qiu Jiang, and H. N. Alshareef. A general strategy for the fabrication of high performance microsupercapacitors. *Nano Energy*, 16:1–9, 9 2015.
- [244] You-Yu Peng, Bilen Akuzum, Narendra Kurra, Meng-Qiang Zhao, Mohamed Alhabeb, Babak Anasori, Emin Caglan Kumbur, Husam N. Alshareef, Ming-Der Ger, and Yury Gogotsi. All-mxene (2D titanium carbide) solid-state microsupercapacitors for on-chip energy storage. *Energy Environ. Sci.*, 9(9):2847–2854, 2016.
- [245] Zhong-Shuai Wu, Khaled Parvez, Xinliang Feng, and Klaus Müllen. Graphene-based in-plane micro-supercapacitors with high power and energy densities. *Nat. Commun.*, 4:2487 EP –, 09 2013.
- [246] Xu Xiao, Tianqi Li, Peihua Yang, Yuan Gao, Huanyu Jin, Weijian Ni, Wenhui Zhan, Xianghui Zhang, Yuanzhi Cao, Junwen Zhong, Li Gong, Wen-Chun Yen, Wenjie Mai, Jian Chen, Kaifu Huo, Yu-Lun Chueh, Zhong Lin Wang, and Jun Zhou. Fiber-based all-solid-state flexible supercapacitors for self-powered systems. *ACS Nano*, 6(10):9200–9206, 10 2012.
- [247] Maher F. El-Kady, Veronica Strong, Sergey Dubin, and Richard B. Kaner. Laser scribing of high-performance and flexible graphene-based electrochemical capacitors. *Science*, 335(6074):1326–1330, 2012.
- [248] S. Ardizzone, G. Fregonara, and S. Trasatti. 'inner' and 'outer' active surface of RuO₂ electrodes. *Electrochim. Acta*, 35(1):263–267, 1990.
- [249] John B. Cook, Hyung-Seok Kim, Yan Yan, Jesse S. Ko, Shauna Robbennolt, Bruce Dunn, and Sarah H. Tolbert. Mesoporous mos₂ as a transition metal dichalcogenide exhibiting pseudocapacitive li and na-ion charge storage. *Advanced Energy Materials*, 6(9):1501937–n/a, 2016.
- [250] Markéta Zukalová, Martin Kalbáč, Ladislav Kavan, Ivan Exnar, and Michael Graetzel. Pseudocapacitive lithium storage in TiO₂(b). *Chem. Mater.*,

- 17(5):1248–1255, 03 2005.
- [251] Junrong Li, Zilong Tang, and Zhongtai Zhang. Layered hydrogen titanate nanowires with novel lithium intercalation properties. *Chem. Mater.*, 17(23):5848–5855, 2005.
 - [252] Zheng Liu, Yuri G. Andreev, A. Robert Armstrong, Sergio Brutti, Yu Ren, and Peter G. Bruce. Nanostructured $\text{TiO}_2(\text{b})$: the effect of size and shape on anode properties for Li-ion batteries. *Prog. Nat. Sci.: Materials International*, 23(3):235–244, 6 2013.
 - [253] Dae-Yeop Park, Yang-Kook Sun, and Seung-Taek Myung. Carbothermal synthesis of molybdenum(iv) oxide as a high rate anode for rechargeable lithium batteries. *J. Power Sources*, 280:1–4, 4 2015.
 - [254] Hyung-Seok Kim, John B. Cook, Sarah H. Tolbert, and Bruce Dunn. The development of pseudocapacitive properties in nanosized- MoO_2 . *J. Electrochem. Soc.*, 162(5):A5083–A5090, 2015.
 - [255] Liang Liu, Tao Yao, Xiaogang Tan, Qinghua Liu, Zhiqiang Wang, Dacheng Shen, Zhihu Sun, Shiqiang Wei, and Yi Xie. Room-temperature intercalation–deintercalation strategy towards $\text{VO}_2(\text{b})$ single layers with atomic thickness. *Small*, 8(24):3752–3756, 2012.
 - [256] Manish Chhowalla, Hyeon Suk Shin, Goki Eda, Lain-Jong Li, Kian Ping Loh, and Hua Zhang. The chemistry of two-dimensional layered transition metal dichalcogenide nanosheets. *Nat. Chem.*, 5(4):263–275, 04 2013.
 - [257] Kai-Ge Zhou, Nan-Nan Mao, Hang-Xing Wang, Yong Peng, and Hao-Li Zhang. A mixed-solvent strategy for efficient exfoliation of inorganic graphene analogues. *Angew. Chem. Int. Ed.*, 50(46):10839–10842, 2011.
 - [258] H. S. S. Ramakrishna Matte, A. Gomathi, Arun K. Manna, Dattatray J. Late, Ranjan Datta, Swapna K. Pati, and C. N. R. Rao. MoS_2 and WS_2 analogues of graphene. *Angew. Chem. Int. Ed.*, 49(24):4059–4062, 2010.
 - [259] Benxia Li, Yang Xu, Guoxin Rong, Meng Jing, and Yi Xie. Vanadium pentoxide nanobelts and nanorolls: from controllable synthesis to investigation of their electrochemical properties and photocatalytic activities. *Nanotechnology*, 17(10):2560, 2006.
 - [260] Winny Dong, Jeffrey S. Sakamoto, and Bruce Dunn. Electrochemical properties of vanadium oxide aerogels. *Sci. Tech. Adv. Mater.*, 4(1):3, 2003.
 - [261] Ying Wang and Guozhong Cao. Synthesis and enhanced intercalation properties of nanostructured vanadium oxides. *Chem. Mater.*, 18(12):2787–2804, 2006.
 - [262] Arianna Moretti and Stefano Passerini. Bilayered nanostructured $\text{V}_2\text{O}_5 \cdot n\text{H}_2\text{O}$ for metal batteries. *Adv. Energy Mater.*, 6(23):1600868–n/a, 2016.
 - [263] M. Sathiya, A. S. Prakash, K. Ramesha, J.-M. Tarascon, and A. K. Shukla. V_2O_5 -anchored carbon nanotubes for enhanced electrochemical energy storage. *J. Am. Chem. Soc.*, 133(40):16291–16299, 2011.
 - [264] Xiyue Zhang, Minghao Yu, Shaobin Zhao, Feng Li, Xianlei Hu, Shoubin Guo, Xihong Lu, and Yexiang Tong. $3\text{D V}_3\text{O}_7 \cdot \text{H}_2\text{O}$ /partially exfoliated carbon nanotube composites with significantly improved lithium storage ability. *Part. Part. Syst. Charact.*, 33(8):531–537, 2016.
 - [265] Sofiane Boukhalfa, Kara Evanoff, and Gleb Yushin. Atomic layer deposition of vanadium oxide on carbon nanotubes for high-power supercapacitor

- electrodes. *Energy Environ. Sci.*, 5:6872–6879, 2012.
- [266] J. S. Sakamoto and B. Dunn. Vanadium oxide-carbon nanotube composite electrodes for use in secondary lithium batteries. *J. Electrochem. Soc.*, 149(1):A26–A30, 2002.
- [267] Qi Liu, Zhe-Fei Li, Yadong Liu, Hangyu Zhang, Yang Ren, Cheng-Jun Sun, Wenquan Lu, Yun Zhou, Lia Stanciu, Eric A. Stach, and Jian Xie. Graphene-modified nanostructured vanadium pentoxide hybrids with extraordinary electrochemical performance for Li-ion batteries. *Nat. Commun.*, 6:6127 EP –, 01 2015.
- [268] Xianhong Rui, Jixin Zhu, Weiling Liu, Huiteng Tan, Daohao Sim, Chen Xu, Hua Zhang, Jan Ma, Huey Hoon Hng, Tuti Mariana Lim, and Qingyu Yan. Facile preparation of hydrated vanadium pentoxide nanobelts based bulky paper as flexible binder-free cathodes for high-performance lithium ion batteries. *RSC Adv.*, 1:117–122, 2011.
- [269] C. Delmas, H. Cognac-Auradou, J. M. Cocciantelli, M. Ménétrier, and J. P. Doumerc. The $\text{Li}_x\text{V}_2\text{O}_5$ system: An overview of the structure modifications induced by the lithium intercalation. *Solid State Ionics*, 69(3):257–264, 1994.
- [270] M. Nabavi, C. Sanchez, F. Taulelle, J. Livage, and A. de Guibert. Electrochemical properties of amorphous V_2O_5 . *Solid State Ionics*, 28:1183–1186, 1988.
- [271] Henrik H. Kristoffersen and Horia Metiu. Structure of $\text{V}_2\text{O}_5 \cdot n\text{H}_2\text{O}$ xerogels. *J. Phys. Chem. C*, 120(7):3986–3992, 02 2016.
- [272] Sergey Vyazovkin, Alan K. Burnham, JoséM. Criado, Luis A. Pérez-Maqueda, Crisan Popescu, and Nicolas Sbirrazzuoli. Ictac kinetics committee recommendations for performing kinetic computations on thermal analysis data. *Thermochimica Acta*, 520(1–2):1–19, 6 2011.
- [273] R. L. Blaine and B. K. Hahn. Obtaining kinetic parameters by modulated thermogravimetry. *J. Therm. Anal. Calorim.*, 54(2):695–704, 1998.
- [274] Giorgio Montaudou and Robert P. Lattimer. *Mass spectrometry of polymers*. CRC Press, 2001.
- [275] Jean Rouquerol, Françoise Rouquerol, Philip Llewellyn, Guillaume Maurin, and Kenneth SW *Adsorption by powders and porous solids: principles, methodology and applications*. Academic press, 2013.
- [276] Matthias Thommes, Katsumi Kaneko, Alexander V Neimark, James P Olivier, Francisco Rodriguez-Reinoso, Jean Rouquerol, and Kenneth SW Sing. Physisorption of gases, with special reference to the evaluation of surface area and pore size distribution (IUPAC technical report). *IUPAC*, 87(9-10):1051–1069
- [277] Kenneth SW Sing. Reporting physisorption data for gas/solid systems with special reference to the determination of surface area and porosity (recommendations 1984). *IUPAC*, 57(4):603–619
- [278] Richard G Compton and Craig E *Understanding voltammetry*. World Scientific, 2007.
- [279] Vadim F. Lvovich. *Impedance spectroscopy: applications to electrochemical and dielectric phenomena*. John Wiley & Sons, 2012.
- [280] Aliaksandr S. Bandarenka. Exploring the interfaces between metal electrodes and aqueous electrolytes with electrochemical impedance spectroscopy.

Analyst, 138(19):5540–5554, 2013.

- [281] Doron Aurbach. Review of selected electrode–solution interactions which determine the performance of Li and Li-ion batteries. *J. Power Sources*, 89(2):206–218, 8 2000.

Acta Universitatis Upsaliensis

*Digital Comprehensive Summaries of Uppsala Dissertations
from the Faculty of Science and Technology 1469*

Editor: The Dean of the Faculty of Science and Technology

A doctoral dissertation from the Faculty of Science and Technology, Uppsala University, is usually a summary of a number of papers. A few copies of the complete dissertation are kept at major Swedish research libraries, while the summary alone is distributed internationally through the series Digital Comprehensive Summaries of Uppsala Dissertations from the Faculty of Science and Technology. (Prior to January, 2005, the series was published under the title "Comprehensive Summaries of Uppsala Dissertations from the Faculty of Science and Technology".)

Distribution: publications.uu.se
urn:nbn:se:uu:diva-312897



ACTA
UNIVERSITATIS
UPSALIENSIS
UPPSALA
2017